Tracking Vibrational Dynamics

Time-Resolved 2-Color Vibrational Sum-Frequency Spectroscopy of Calcium Arachidate Adsorbate Layers

Dissertation
zur Erlangung des akademischen Grades eines Doktors der Naturwissenschaften
– Dr. rer. nat. –

vorgelegt von

MICHAEL LACKNER

Mai 2021

Fakultät für Chemie
Universität Duisburg-Essen

Betreuer
Prof. Dr. Eckart Hasselbrink

DOI: 10.17185/duepublico/74985
URN: urn:nbn:de:hbz:464-20211122-093554-8

Gutachter:
Prof. Dr. Eckart Hasselbrink
Prof. Dr. Richard Kramer Campen

Vorsitzender:
Prof. Dr. Mathias Ropohl

Datum der Disputation:
19. Oktober 2021

Die vorliegende Arbeit wurde im Zeitraum von Januar 2017 bis Mai 2021 unter Anleitung von Prof. Dr. Eckart Hasselbrink in der Fakultät für Chemie der Universität Duisburg-Essen durchgeführt.

Contents

Preface

This thesis was written in the context of the collaborative research center (CRC) 1242 "*Non-Equilibrium Dynamics of Condensed Matter in the Time Domain*". The CRC took off in the second half of 2016 and the first funding period ended in the first half of 2020. The overall goal of the CRC was to gain a fundamental understanding of the dynamics of non-equilibrium states in condensed matter. Ultimately, the CRC aimed to find material properties that only exist if the material is in a non-equilibrium state. These properties could eventually prove useful in future applications.

Our subproject "*Time-Resolved 2D-IR-Spectroscopy on Adsorbate Layers*" had the goal to track the dynamics of vibrational degrees of freedom in adsorbate systems. For this purpose, we set up a novel time-resolved non-coherent pump-probe spectroscopy experiment where the adsorbate is pumped with an infrared (IR) laser pulse, and the system is probed with vibrational sum-frequency spectroscopy (vSFS). The novelty of the experiment lies in the fact that the photon energies of the pump and probe pulses are entirely independent of one another.

One may notice that the subtitle of this thesis, "*Time-Resolved 2-Color Vibrational Sum Frequency Spectroscopy of Calcium Arachidate Adsorbate Layers*", deviates from the original title of the subproject. This is because the term "2D-spectroscopy" is reserved for spectroscopic methods where the pump and the probe pulse are coherent. In our case, the pump and probe pulses are non-coherent, so the correct term to use is "2-color spectroscopy".

1 Goal of the Project

With this project, we aim to show that we can track the non-equilibrium dynamics in an adsorbate system by utilizing a novel spectroscopic setup. In short, the idea is that a narrowband IR pulse excites specific vibrations in the adsorbate layer. After a specific time delay, a broadband IR pulse probes the adsorbate layer to determine which vibrational modes are currently excited. Here, the idea is that the color of the pump pulse is independent of the color of the probe pulse – hence the name "2-color spectroscopy". As a consequence, the probed spectral region does not necessarily have to match the pumped spectral region. From the spectroscopic data, we want to obtain information on

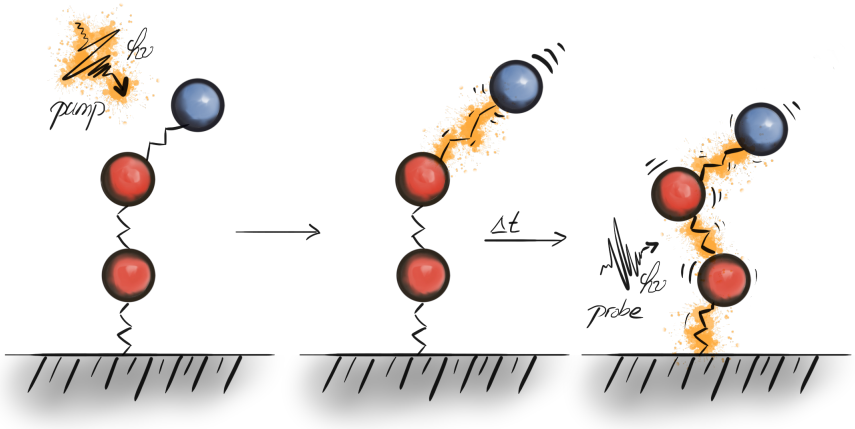

Figure 1: Illustration of the concept of probing vibrational energy redistribution in an adsorbate molecule. A narrowband pump pulse excites a specific vibration. After a certain time Δt a broadband pulse probes the molecule to determine which vibrational modes are currently excited.

- population lifetimes of the involved vibrational modes
- energy redistribution between these vibrational modes, and
- possible pathways of vibrational energy relaxation.

As a secondary objective, we planned to study this energy flow systematically. For example, this is achievable by varying the density of excitation or the packing density of the adsorbate layer. This would give further insights into the dynamics at hand. This secondary objective, however, is not part of this thesis.

The scope of this project covered roughly four parts. The first was to set up the laser system and all devices that were necessary to conduct the experiment. The second goal was to evaluate how to best perform the experiment from a technical standpoint and which adsorbate systems are optimal to use. The third part was to develop the tooling to process and analyze our data. Lastly, the vibrational dynamics of a monolayer of long-chain fatty acids were analyzed.

2 Timeline

The main components of the laser system arrived in 2016. The first task was to set up all the necessary devices that were needed to record a non-time-resolved vSFS spectrum. The second step was to find an appropriate adsorbate system to work with and perform time-resolved measurements. We eventually decided to perform the experiments using calcium arachidate adsorbed on glass since we worked with this system in our group previously. The first successful experiments with the time-resolved setup came in 2019, more or less

by chance. After finding a good workflow, we were at last able to perform reproducible measurements in the second half of 2019, which resulted in our paper [1] published in late 2019 showing the proof of concept of our experiment.

1 Theory

The theory chapter has three parts. The first part gives an overview of vibrational spectroscopy in general and ultimately builds up towards an understanding of the principles of vibrational sum-frequency spectroscopy. The second part is about vibrational dynamics, detailing concepts like vibrational energy redistribution and anharmonic coupling. The third part details previous experiments and results that are essential to this work.

1.1 Vibrational Spectroscopy

This chapter aims to explain the principles of vibrational sum-frequency spectroscopy (vSFS). We use this type of spectroscopy in our experimental setup. Basic knowledge of the fundamentals of vSFS is necessary to understand certain design choices in our experiment and also to interpret the experimental results. For this purpose, it is helpful to build up our understanding step by step, starting with molecular vibrations. Next, this chapter gives an introduction to infrared and Raman spectroscopy. Lastly, we will discuss nonlinear optics in general and sum-frequency spectroscopy in particular.

1.1.1 Molecular Vibrations

The very basis for being able to do vibrational spectroscopy as such is that molecules vibrate. As molecules become more complex, so do their vibrational patterns. We can express these vibrations – no matter how complex the molecules are – as linear combinations of so-called normal modes. At least, this is true in the harmonic approximation. Also, if we know the number of atoms N in the molecule, we can tell how many normal modes there are. These are $3N - 5$ modes in case the molecule is linear, or $3N - 6$ modes in case the molecule is non-linear. Thus, for a linear CO_2 molecule, we get four normal modes. For a more complex molecule like arachidate ($C_{20}H_{39}O_2^-$), the number of normal modes increases to as much as 177.

We can classify these normal modes into two different kinds of vibrations: Stretching vibrations which typically have a high frequency, and deformation modes which tend to be lower in energy. Stretching vibrations are such modes where the angle between the individual bonds in the molecule does not change significantly compared to the bond length itself. We can further divide these into symmetric and asymmetric stretching

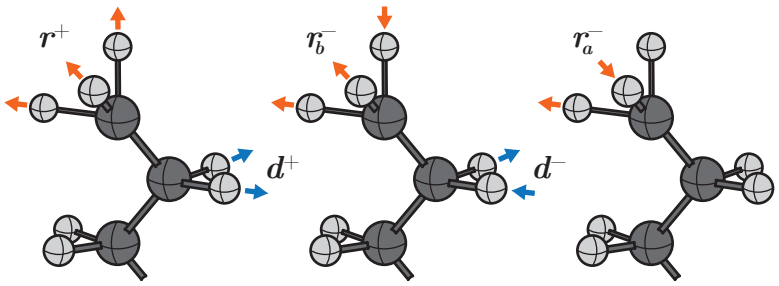

Figure 1.1: Stretching modes of the methyl group a) symmetric (r^+), b) asymmetric in-plane (r_b^-), c) asymmetric out-of-plane (r_a^-) and the methyl group a) symmetric (d^+) and b) asymmetric (d^-). The arrows indicate the displacement vector of the hydrogen atoms. The minor displacements of the carbon atoms is not shown. Inspired by Ref. [2].

modes and stretching modes that are neither symmetrical nor asymmetrical. Figure 1.1 illustrates the symmetric and asymmetric stretching modes for the methylene (CH_2) and methyl (CH_3) groups. These moieties are present in the alkyl chain of fatty acids and at the end of the chain, respectively. There are as many stretching modes in a molecule that can be associated with C–H bonds as there are individual C–H bonds. In the arachidate molecule, there are 39 C–H bonds, which means there will be 39 individual stretching modes. The same concept applies to individual functional groups. If we take the methyl head group of the arachidate, there will be 3 C–H stretching modes associated with that head group. The other 36 modes, we can attribute to the methyl stretches of the alkyl chain. However, contrary to the depiction in Figure 1.1, there are no localized modes at the individual moieties. It is more like these normal modes involve all atoms in a given molecule. It is just that the force vectors associated with a given vibrational mode are stronger on some atoms than on others. Energetically, the C–H stretching modes are located around $3000\,\mathrm{cm}^{-1}$ and will be most relevant for the recorded spectra in Chapter 2.

The deformation modes of the C–H bonds are energetically lower than the stretching modes, starting at around $1500\,\mathrm{cm}^{-1}$ downwards. The deformation modes are categorized into bending, rocking, wagging, and twisting modes.

To describe the potential energy of a vibrational mode it is useful to work with the normal coordinate Q_k instead of Cartesian coordinates. For any given normal mode k the normal coordinate simply describes the deviation from the equilibrium position. In the harmonic approximation the restoring force F_k is proportional to the displacement from the equilibrium position

$$F_k = -k_k Q_k \tag{1.1}$$

and the potential energy U can be expressed as

$$U(Q_k) = \frac{1}{2} k_k Q_k^2 \ . \tag{1.2}$$

If we solve the Schrödinger equation with this potential as part of the hamiltonian $\hat{\mathrm{H}}$ for a vibrational wave function ψ_{vib}

$$\hat{\mathrm{H}}\psi_{\mathrm{vib}} = \psi_{\mathrm{vib}} E \ , \tag{1.3}$$

we get eigenstates for different quanta v with energies

$$E_v = h\nu_k \left(v + \frac{1}{2} \right) \ , \tag{1.4}$$

where h is Planck's constant and ν is the frequency that describes the harmonic potential. This is linked to the force constant k and the reduced mass m via

$$\nu_k = \sqrt{\frac{k_k}{m_k}} \ . \tag{1.5}$$

This quantization of energy of the molecular vibrations is what allows us to perform optical vibrational spectroscopy on molecules, where we can tune the energy of the light to match those vibrational quanta. The probability P_{nm} with which a transition from a state Ψ_n to a state Ψ_m may occur can be expressed as

$$P_{nm} = \langle \Psi_m | \hat{\mathrm{O}} | \Psi_n \rangle \tag{1.6}$$

The states Ψ do not only represent the vibrational degrees of freedom but also rotational and electronic degrees of freedom. By applying the Born-Oppenheimer approximation we can unravel Equation 1.6 into

$$\begin{aligned} P_{nm} &= \langle \psi_{\mathrm{rot},m} \psi_{\mathrm{vib},m} \psi_{\mathrm{el},m} | \hat{\mathrm{O}}_{\mathrm{rot}} + \hat{\mathrm{O}}_{\mathrm{vib}} + \hat{\mathrm{O}}_{\mathrm{el}} | \psi_{\mathrm{rot},n} \psi_{\mathrm{vib},n} \psi_{\mathrm{el},n} \rangle \qquad (1.7) \\ &= \langle \psi_{\mathrm{vib},m} | \psi_{\mathrm{vib},n} \rangle \langle \psi_{\mathrm{el},m} | \psi_{\mathrm{el},n} \rangle \langle \psi_{\mathrm{rot},m} | \hat{\mathrm{O}}_{\mathrm{rot}} | \psi_{\mathrm{rot},n} \rangle \\ &+ \langle \psi_{\mathrm{rot},m} | \psi_{\mathrm{rot},n} \rangle \langle \psi_{\mathrm{el},m} | \psi_{\mathrm{el},n} \rangle \langle \psi_{\mathrm{vib},m} | \hat{\mathrm{O}}_{\mathrm{vib}} | \psi_{\mathrm{vib},n} \rangle \\ &+ \langle \psi_{\mathrm{rot},m} | \psi_{\mathrm{rot},n} \rangle \langle \psi_{\mathrm{vib},m} | \psi_{\mathrm{vib},n} \rangle \langle \psi_{\mathrm{el},m} | \hat{\mathrm{O}}_{\mathrm{el}} | \psi_{\mathrm{el},n} \rangle \qquad (1.8) \end{aligned}$$

Here, we are only interested in transitions where the vibrational wave function changes, but the rotational and electronic wave functions do not change. Thus, the first and third terms in Equation 1.8 vanish and we are left with the second term. The probability P_{nm} with which a transition from a vibrational state $\psi_{\mathrm{vib},n}$ to a vibrational state $\psi_{\mathrm{vib},m}$ may

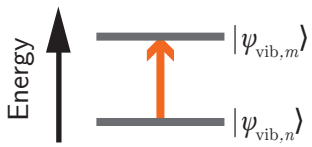

Figure 1.2: Schematic of IR absorption spectroscopy: a photon of energy $h\nu$ causes a transition from state $|\psi_{\mathrm{vib},n}\rangle$ to $|\psi_{\mathrm{vib},m}\rangle$.

occur can be expressed as

$$P_{nm} = \langle\psi_{\mathrm{vib},m}|\hat{\mathrm{O}}_{\mathrm{vib}}|\psi_{\mathrm{vib},n}\rangle \ . \tag{1.9}$$

The Operator $\hat{\mathrm{O}}_{\mathrm{vib}}$ is a general description of how the molecule is perturbed by the electric field of the light and differs depending on whether we deal with infrared, Raman or vibrational sum frequency spectroscopy.

1.1.2 Infrared Absorption Spectroscopy

In infrared (IR) absorption spectroscopy, we shoot photons with a relatively wide range of energies at a sample. After that, we determine which of these photons got absorbed. The absorbed photons transition the system from state $|\psi_{\mathrm{vib},n}\rangle$ to state $|\psi_{\mathrm{vib},m}\rangle$ (see Figure 1.2). Concurrently, this will also change the rotational state $|\psi_{\mathrm{rot},}\rangle$, but for the sake of simplicity, we will omit this.

In a molecule, due to different electronegativity of the individual atoms, we can assign a charge e_i to each atom i at position vector $\vec{r}_i$. The dipole moment $\vec{\mu}$ is then given by

$$\vec{\mu} = \sum_i e_i \vec{r}_i \ . \tag{1.10}$$

This is the operator used in Equation 1.6 in the case of IR spectroscopy:

$$\langle\mu\rangle = \langle\psi_{\mathrm{vib},m}|\hat{\mu}|\psi_{\mathrm{vib},n}\rangle \ . \tag{1.11}$$

The expectation value $\langle\mu\rangle$ is called the transition dipole moment and relates to the intensity I_{IR} of the vibrational mode in the IR spectrum via

$$I_{\mathrm{IR}} \propto \langle\mu\rangle^2 \ . \tag{1.12}$$

It is convenient to write the transition dipole moment operator in terms of a normal coordinate Q_k for any given normal mode k instead of Cartesian coordinates $\vec{r}$. With this,

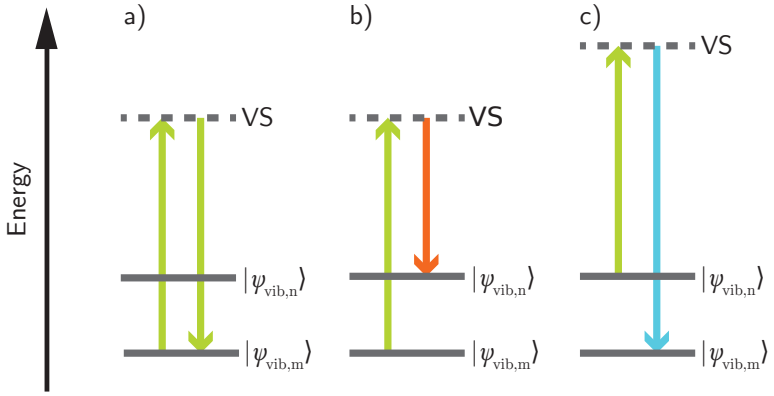

Figure 1.3: The principle of light scattering in a molecule: a) elastic Rayleigh scattering, b) and c) inelastic Raman scattering (Stokes and anti-Stokes). The dotted lines, denoted with *VS* represent *virtual states*.

Equation 1.10 can be expressed as a Taylor series

$$\hat{\mu}_k = \hat{\mu}_k\Big|_0 + \frac{\partial \hat{\mu}_k}{\partial Q_k}\Big|_0 Q_k + \dots \,, \tag{1.13}$$

which we can terminate after the first derivative, since we expect that the change of the dipole moment is constant as we move along the normal coordinate. In this notation $\hat{\mu}_k\Big|_0$ is the static dipole of the molecule. Plugging Equation 1.13 into Equation 1.11 we get

$$\langle \mu \rangle = \hat{\mu}_k\Big|_0 \langle \psi_{\text{vib},m} | \psi_{\text{vib},n} \rangle + \frac{\partial \hat{\mu}_k}{\partial Q_k}\Big|_0 \langle \psi_{\text{vib},m} | Q_k | \psi_{\text{vib},n} \rangle \ . \tag{1.14}$$

From the second term in this equation, we can derive the selection rule for IR spectroscopy: Firstly, the change in quantum number between states n and m has to be ± 1. In any other case, the term $\langle \psi_{\text{vib},m} | Q_k | \psi_{\text{vib},n} \rangle$ equals 0. Secondly, the dipole moment of the molecule has to change if we move along the normal coordinate. We can also deduce that it does not matter if the molecule has a static dipole because the wave functions $\psi_{\text{vib},m}$ and $\psi_{\text{vib},n}$ are always orthogonal if $m \neq n$, i.e. $\langle \psi_{\text{vib},m} | \psi_{\text{vib},n} \rangle = 0$.

With this, we have managed to establish the basics of vibrational IR spectroscopy. We can now move on to the slightly more complex Raman spectroscopy before we continue with nonlinear optics and sum-frequency spectroscopy.

1.1.3 Raman Scattering

Let us consider having a molecule that is exposed to an external electric field $\vec{E}(t)$ that oscillates with frequency ν_0 and amplitude $\vec{E}_0$:

$$\vec{E}(t) = \vec{E}_0 \cos(2\pi\nu_0 t) \tag{1.15}$$

This electric field will cause a relative displacement of the electrons and nuclei in the molecule, inducing a dipole

$$\vec{\mu}_{\text{ind}}(t) = \alpha \vec{E}(t) \tag{1.16}$$

in the molecule. Here, α describes the polarizability of the molecule. However the induced dipole does not simply scale with the external electric field. This is because typically we cannot polarize a molecule in just one spatial direction. If the electric field pushes the electrons in one direction, this will also induce a dipole in the other two spatial directions. Therefore the polarizability has to be expressed as a symmetric rank two tensor of the form

$$\alpha = \begin{vmatrix} \alpha_{xx} & \alpha_{xy} & \alpha_{xz} \\ \alpha_{yx} & \alpha_{yy} & \alpha_{yz} \\ \alpha_{zx} & \alpha_{zy} & \alpha_{zz} \end{vmatrix} \tag{1.17}$$

where $\alpha_{xy} = \alpha_{yx}$, $\alpha_{xz} = \alpha_{zx}$ and $\alpha_{yz} = \alpha_{zy}$ [3]. So, according to Equation 1.16, α will transform the electric field vector $\vec{E}$ in such a way that the resulting induced dipole does not necessarily have to point in the same direction as the electric field does.

Again, as was the case with the transition dipole moment operator in Section 1.1.2, we can write the polarizability as a Taylor series in normal coordinates:

$$\hat{\alpha}_k(\nu_0) = \hat{\alpha}_k(\nu_0)\Big|_0 + \left.\frac{\partial \hat{\alpha}_k}{\partial Q_k}\right|_0 Q_k \cos\left(2\pi\nu_k t\right) \tag{1.18}$$

This expression also incorporates the frequency ν_k of normal mode k. We can end the Taylor series after the first derivative, since we – again – deal with low field strengths of $\vec{E}$ and thus the polarizability will be proportional to Q_k. Q_k will also change periodically but not necessarily with the frequency of the electric field ν_0. In the case of vibrational IR spectroscopy, we deduced from Equation 1.14, that the electric dipole moment of the molecule has to change, in order to absorb the photon. Here, we can see, that for the molecule, in order to scatter the light wave, at least one component of $\hat{\alpha}_k$ – i.e. the polarizability – has to change during the time of irradiation. Combining Equation 1.18 with Equations 1.15 and 1.16, yields for the induced dipole

$$\begin{aligned} \vec{\mu}_{\text{ind}} = {} & \hat{\alpha}_k\Big|_0 \cdot E_0 \cos(2\pi\nu_0 t) \\ & + \left.\frac{\partial \hat{\alpha}_k}{\partial Q_k}\right|_0 Q_k \left[2\pi t(\cos(\nu_0 - \nu_k) + \cos(\nu_0 + \nu_k)\right] \ . \end{aligned} \tag{1.19}$$

From this we can see that the molecule radiates with three different frequencies (compare Figure 1.3):

1. ν_0 which corresponds to elastic Rayleigh scattering

2. $\nu_0 - \nu_k$, corresponding to the Stokes transition and

3. $\nu_0 + \nu_k$ for the anti-Stokes transition.

Like an ordinary antenna, the molecule will, according to classical electrodynamics, radiate the electromagnetic wave in a toroidal pattern. Whereby the induced dipole vector is the symmetry axis of that toroid. For example, if we have an electromagnetic wave polarized in the y-coordinate, it will move the electrons of the molecule along this coordinate. The scattered electromagnetic wave will then propagate in the x-z-plane with no preferred direction.

In Sections 1.1.2 and 1.1.3 we gained a fundamental understanding of linear optics and related spectroscopic methods. In the next chapter we will advance to nonlinear optics.

1.1.4 Nonlinear Optics

In this section, we take a closer look at second and third-order nonlinear effects. For sum-frequency spectroscopy, especially second-order nonlinear effects are of interest. However, also third-order nonlinear effects can play a role.[4] This section will help us understand how higher-order nonlinear processes work and in which kind of materials or systems these processes will occur.

Let us extend the principle discussed earlier, where an electric field induces a dipole in a medium.

$$\vec{\mu}_{\text{ind}}(t) = \vec{\mu}_0 + \alpha\vec{E}(t) \tag{1.20}$$

Here, $\vec{\mu}_0$ is the static dipole moment. Often the polarizability α and the induced dipole moment $\vec{\mu}(t)$ are only used if we consider a single molecule. If we consider a crystal or multiple molecules, we describe the effect of the electromagnetic radiation on the system in terms of polarization $\vec{P}$. The polarization is the dipole moment per unit volume. Likewise, the polarizability of the system as a whole is described by the susceptibility χ:

$$\vec{P}_{\text{ind}}(t) = \epsilon_0\chi^{(1)}\vec{E}(t) \tag{1.21}$$

With $\chi^{(1)}$ being the first-order susceptibility and ϵ_0 being the vacuum permittivity. We omit the static dipole moment and regard $\vec{P}_{\text{ind}}(t)$ as the induced polarization. However, this only describes the linear response of a medium. If the strength of the electric field in the medium is sufficiently high, the polarization of the material will not increase linearly with the applied electric field anymore. In this case, we need to extend Equation 1.21 by a quadratic term (for even higher field strengths we have to add a cubic term and so on)

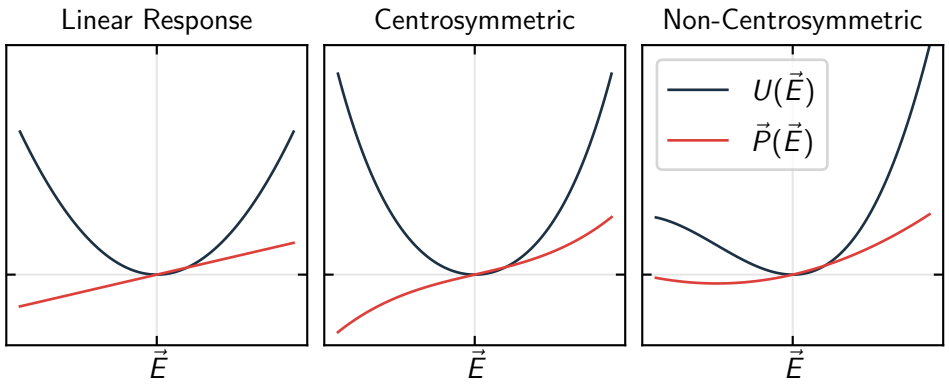

Figure 1.4: Potential energies $U(\vec{E})$ (black lines) and polarizations $P(\vec{E})$ (red lines) for a medium with a purely harmonic potential and linear polarization (left), for a centrosymmetric medium with an anharmonic potential (center) and for a non-centrosymmetric medium with an anharmonic potential (right). The polarization is proportional to the derivative of the potential energy with respect to the electric field: $P(\vec{E}) \propto \mathrm{d}U(\vec{E})/\mathrm{d}\vec{E}$

to describe the polarization of the material appropriately:

$$\vec{P}(t) = \epsilon_0 \left[\chi^{(1)}\vec{E}(t) + \chi^{(2)}\vec{E}^2(t) + \chi^{(3)}\vec{E}^3(t) + ...\right] \tag{1.22}$$

$\chi^{(2)}$ and $\chi^{(3)}$ are called the second and third-order susceptibility respectively. Typically each successive higher-order susceptibility decreases by orders of magnitude. Each term can also be written in the form $P^{(o)} = \epsilon_0 \chi^{(o)} E^o$ where $P^{(o)}$ is called the oth-order polarization. The implication of this is that if we have an electric field of sufficiently high field strength in a medium exhibiting nonlinear properties like we see in Equation 1.22, the medium itself will again (as we saw in Rayleigh scattering) radiate an electric field of its own. This time not only with the fundamental frequency of the electric field but also multiples of this frequency. This is depicted in Figures 1.4 and 1.5. For simplicity, let us treat all susceptibilities and field strengths as scalars although they are rank o tensors.

On the left of Figure 1.4, we see a system that has a purely linear response as described in Equation 1.21. The potential energy induced in the system by the electric field is harmonic and follows $U(E) \propto E^2$ (a parabola). Thus, the polarization of the medium increases linearly with $\vec{E}$. If the electric field is pointing in the opposite direction, i.e., it changes its sign, the polarization will change its sign too. Now, if we let the electric field oscillate, the polarization will also oscillate in the same manner, and the medium will radiate an electric field on its own. Figure 1.5 shows this process on the top left.

We can now Fourier transform the output of the oscillator to see with which frequency

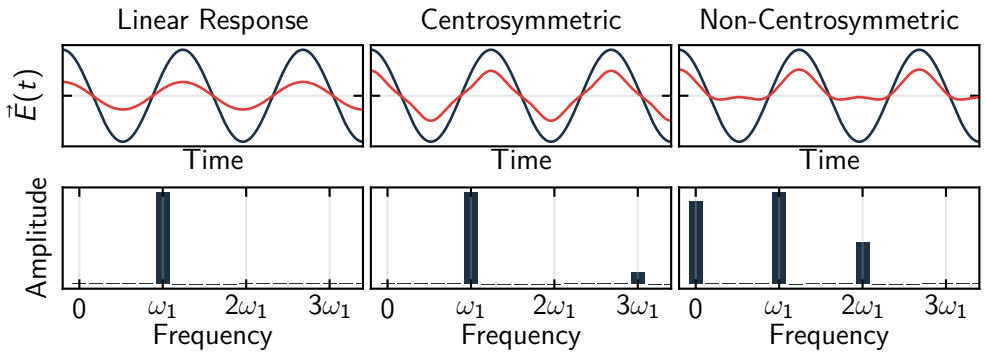

Figure 1.5: Top: External electric field (black lines) and radiated electric field of the oscillating medium (red lines) corresponding to the potentials and polarizations in Figure 1.4. The external electric field oscillates with a single frequency ω_1. Bottom: Fourier transforms of the electromagnetic field vector $\vec{E}(t)$ radiated by the oscillating media.

it radiates. Figure 1.5 shows this on the bottom left. Unsurprisingly the medium oscillates with a single frequency, corresponding to the frequency of the initial electric field.

Next, let us consider a medium that does not behave harmonically and where we can describe the potential energy of the system with

$$U(E,t) \propto \chi^{(1)}E + \chi^{(3)}E^3 \,, \tag{1.23}$$

like depicted in the center plot of Figure 1.4. The medium behaves the same in all spatial directions since the potential energy is symmetric to the electric field vector. With this, the medium is centrosymmetric. We can describe its total polarization by the sum of the first and third-order polarizations

$$P(E,t) = P^{(1)}(E,t) + P^{(3)}(E,t) \,, \tag{1.24}$$

In this case, Fourier transforming the output of the oscillator (see Figure 1.5) again gives us the fundamental frequency ω_1 but also the third harmonic at $3\omega_1$.

The third case is a medium where the potential energy – and therefore also the polarization – depends on the direction of the electric field (see the right plot in Figure 1.4). If the electric field points to one side, the potential energy quickly rises. If it points in the opposite direction, the potential energy will only slowly increase. In this case, we have a non-centrosymmetric medium, i.e., the medium behaves differently in each spatial direction. We can then describe the potential energy with

$$U(E,t) \propto \chi^{(1)}E + \chi^{(2)}E^2 \tag{1.25}$$

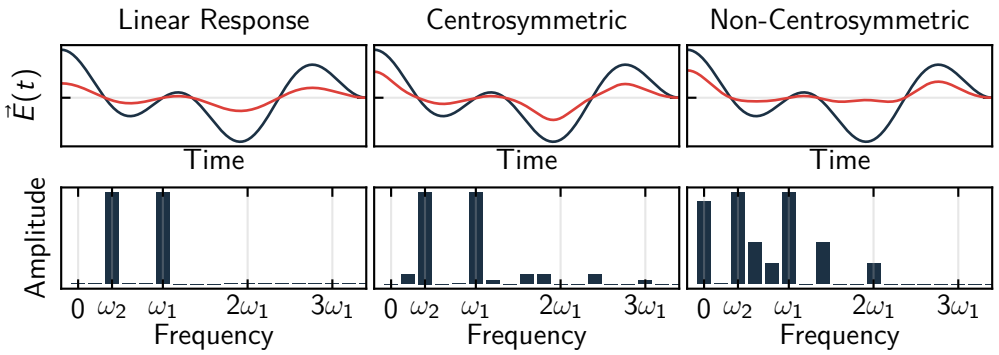

Figure 1.6: Top: External electric field (black lines) and radiated electric field of the oscillating medium (red lines) corresponding to the potentials and polarizations in Figure 1.4. The external electric field oscillates two distinct frequencies ω_1 and ω_2. Bottom: Fourier transforms of the electromagnetic field vector $\vec{E}(t)$ radiated by the oscillating media.

and the polarization accordingly with

$$P(E,t) = P^{(1)}(E,t) + P^{(2)}(E,t) \; . \tag{1.26}$$

Of course for a particular system the polarization could also depend on higher order polarizations like $P^{(3)}$ etc. but we will omit these to make things simpler. Now the Fourier transformed output of the oscillating medium shows frequencies at $0\omega_1$ and $2\omega_1$ besides the fundamental. The second process is called second harmonic generation (SHG). Second-order nonlinear processes (or higher even-order nonlinear processes) can only occur in non-isotropic media.

So far, we only looked at cases where the initial electric field oscillates with a single frequency ω_1. What happens if the electric field is a superposition of two oscillating electric fields oscillating with frequencies ω_1 and ω_2? This case is depicted in Figure 1.6. In the case of the harmonic system with linear polarization response, we see that the medium still only oscillates with frequencies ω_1 and ω_2. Things become more interesting when we look at the isotropic (centrosymmetric) system. Here the electric field oscillates with any three-fold combinations of the fundamental frequencies. These are (from left to right):

1) $\omega_1 - \omega_2 - \omega_2$, 2) $\omega_2 + \omega_2 - \omega_2$ (and the fundamental), 3) $\omega_1 + \omega_1 - \omega_1$ (and the fundamental), 4) the third harmonic of ω_2 $(\omega_2 + \omega_2 + \omega_2)$, 5) $\omega_1 + \omega_1 - \omega_2$, 6) $\omega_1 + \omega_2 + \omega_2$, 7) $\omega_1 + \omega_1 + \omega_2$ and 8) the third harmonic of ω_1 $(\omega_1 + \omega_1 + \omega_1)$. The non-isotropic, non-centrosymmetric system with only $P^{(1)}$ and $P(2)$ contributions shows, aside from the fundamental frequencies, any two-fold combination of the frequencies ω_1 and ω_2. These are (left to right): 1) $\omega_1 - \omega_1$ and $\omega_2 - \omega_2$, 2) $\omega_1 - \omega_2$ (this process is called difference-

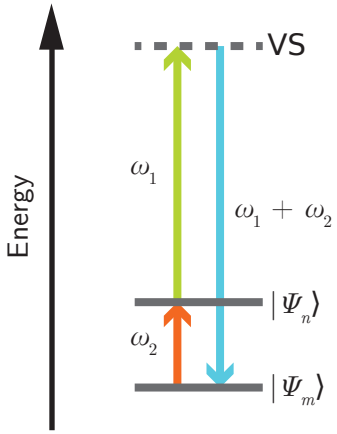

Figure 1.7: Schematic of a resonant vibrational SFG process. The IR pulse is resonantly tuned to the transition frequency ω_2 between $|\Psi_m\rangle$ and $|\Psi_n\rangle$. A laser pulse with frequency ω_1 "up-converts" the IR photons to a virtual state (VS). These two pulses generate light with energy corresponding to the sum of both frequencies $(\omega_1 + \omega_2)$.

frequency generation (DFG)), 3) the second harmonic $\omega_2 + \omega_2$, 4) $\omega_1 + \omega_2$ (this process is called sum-frequency generation (SFG)) and 5) the second harmonic $\omega_1 + \omega_1$.

In this thesis, we are specifically interested in the SFG process since this is the process we are using for probing our samples. In this section, we gained a fundamental understanding of nonlinear optical effects in general. In the next section, we will take a look at the SFG process specifically.

1.1.5 Vibrational Sum-Frequency Spectroscopy

We now want to apply the concepts of nonlinear optics, described in the previous section, to spectroscopic methods. In this section, we discuss how these concepts apply to vibrational sum-frequency spectroscopy (vSFS) in order to be able to interpret the spectra we recorded with our spectrometer.

In vibrational IR spectroscopy, we try to tune the energy of the incident light in such a way that it causes a transition in the sample from one state to another. We can deduce information about the chemical composition and structure of the sample from the energies at which these transitions take place. The same statement applies to vSFS. In vSFS we have two high-energy laser pulses of different photon energies:

1. An IR pulse, tuned to a vibrational transition frequency of the molecule. Since we want to probe vibrational transitions over a specific frequency range, the IR pulse is either tunable in energy or is spectrally broad so that it probes multiple transitions at the same time.

2. An upconversion pulse generating the sum-frequency of these two pulses. The upconversion pulse is typically in the visible or near-infrared region of the electromagnetic

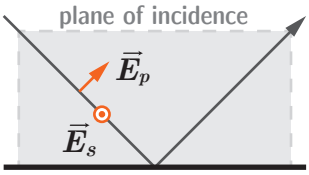

Figure 1.8: Perpendicular (s) and parallel (p) electric field vectors with respect to the plane of incidence

spectrum. It should be spectrally narrow since it is not needed to detect spectral features. Even more so, a spectrally broad upconversion pulse broadens the features of the resulting spectrum.

This process is illustrated in Figure 1.7 In order to obtain a sum-frequency spectrum, we detect the photons that are generated at the sample and resolve them energetically.

Since this is a 3-photon-process, the process shown in Figure 1.7 is only possible in non-isotropic media. Another implication of a 3-photon-process is that the susceptibility of the medium is a rank three tensor. We can interpret the susceptibility tensor similarly to the polarizability tensor in Raman scattering. The important thing about this is that the susceptibility of the medium depends on the direction of the electric field vectors of the two incident pulses. The polarization of these can be either parallel (p) or orthogonal (s from the German word "senkrecht") relative to the plane of incidence. This is illustrated in Figure 1.8. Also, the resulting SF signal can be in either p or s polarization. We can perform vSFS using different combinations of polarizations for the three involved laser pulses. Different polarization combinations can probe different elements of the $\chi^{(2)}$ tensor. With different polarization combinations, we can observe different spectral features. The convention here is to order the polarizations from high to low photon energy. For example, in the *ssp* polarization combination, only the s polarized portion of the sum-frequency signal is probed, the upconversion pulse is polarized orthogonal, and the IR pulse is polarized parallel to the plane of incidence. For a non-chiral medium the only polarization combinations that give rise to a sum-frequency signal are *ssp*, *ppp*, *sps* and *pss* [5–8]. The most widely used polarization combinations are *ssp* and *ppp* since they give the strongest signal (in case the substrate is a dielectric).

In the SFG process, light is not scattered in all directions like it is in Raman scattering. Due to phase matching of the two incident pulses, their sum-frequency leaves the medium at a specific angle. This angle results from the conservation of momentum of the two generating pulses. We can calculate the angle of the reflected sum-frequency beam $\beta_{\mathrm{SF,r}}$ via

$$\sin\beta_{\mathrm{SF,r}} = \frac{\omega_1}{\omega_{\mathrm{SF}}}\frac{n_1(\omega_1)}{n_1(\omega_{\mathrm{SF}})}\sin\beta_{1,\mathrm{i}} + \frac{\omega_2}{\omega_{\mathrm{SF}}}\frac{n_1(\omega_2)}{n_1(\omega_{\mathrm{SF}})}\sin\beta_{2,\mathrm{i}}\ . \tag{1.27}$$

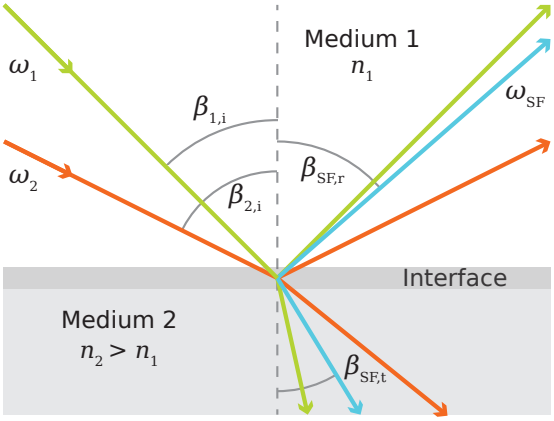

Figure 1.9: Schematic of the reflection and transmission geometries of the beams in sum-frequency generation.

Figure 1.9 illustrates the meaning of the various parameters in the above equation. Here, $\beta_{1,i}$ and $\beta_{2,i}$ are the incident angles of upconversion and IR pulses and $n_1(\omega)$ the index of refraction of the medium through which the incident beams travel. A portion of the generated sum-frequency signal transmits into the bulk sample. We can calculate the angle of the transmitted SF beam via Snell's law of refraction.

Interpretation of SF spectra It is not always obvious which information a spectrum holds. Some parameters that may seem apparent at first glance are the heights, widths, and positions of the peaks in the spectrum. However, things become more complicated if the resonant features overlap in the spectrum, i.e., if they are energetically close. Therefore, it is advantageous for the interpretation of spectra if we have a line shape model at hand that describes the spectrum. In vSFS the intensity of the signal of a vibrational mode q is proportional to the absolute square of its (complex) second-order susceptibility:

$$I_{\mathrm{SF}} \propto \left|\chi_q^{(2)}\right|^2 . \tag{1.28}$$

If we have more than one resonant feature we have to sum up all second-order susceptibilities. In addition, we have to incorporate that these modes may oscillate with a particular phase relation φ towards each other. Also, in case there is a non-resonant background present, we have to take its susceptibility $\chi_{\mathrm{NR}}^{(2)}$ into account. We then end up with

$$I_{\mathrm{SF}} \propto \left|\chi_{\mathrm{NR}}^{(2)} + \sum_q \chi_q^{(2)} e^{i\varphi_q}\right|^2 . \tag{1.29}$$

Of course the non-resonant second-order susceptibility has a phase as well but we can set the phase term to zero so that all phases of the individual resonant modes φ_q are relative to the phase of the non-resonant background.

All $\chi_q^{(2)}$ values depend on the frequency of the electric field. The question now is how

the line shape of the resonances can be best described. Usually, the line shape is expressed in terms of a simple Lorentzian model, so that for a single mode we have

$$\chi_q^{(2)} = \frac{A_q}{\omega_q - \omega + i\Gamma_q} \,, \tag{1.30}$$

where A_q is the oscillator strength, Γ_q is the damping coefficient which is a measure of the width of the resonance, ω is the frequency of the infrared light and ω_q is the resonance frequency of the vibrational mode. Ultimately we can combine Equations 1.30 and 1.29 to

$$I_{\mathrm{SF}} \propto \left| \chi_{\mathrm{NR}}^{(2)} + \sum_q \frac{A_q}{\omega_q - \omega + i\Gamma_q} e^{i\varphi_q} \right|^2 \,. \tag{1.31}$$

With this we have four parameters for each resonance. Since with different polarization combinations, we probe different elements of the $\chi^{(2)}$ tensor, the parameters A_q and φ_q also depend on the polarization combination, whereas Γ_q and ω_q are the same for all elements of the tensor [9]. We use this basic model in Equation 1.31 to fit our data. How the data fitting is done is elucidated further in Section 3.2.

Robert W. Boyd's lectures and his book *Nonlinear Optics* [10] partly served as inspiration for this chapter. Lambert, Davies, and Neivandt [2] give an in-depth overview of sum-frequency spectroscopy. Here, a more exhaustive discussion is unnecessary, and the extent to which this section discusses vSFS should suffice to interpret the spectra presented in this thesis.

1.2 Vibrational Dynamics

As vibrational dynamics, we understand the redistribution of vibrational energy in the time domain. This redistribution can happen between two different vibrational modes or, the vibrational energy can be transformed into another form of energy like, for example, radiation. This redistribution of energy can be intramolecular as well as intermolecular. There are two important parameters to quantify the vibrational dynamics of a specific vibrational mode. These are the dephasing time, typically abbreviated with T_2, and the population relaxation time T_1.

1.2.1 Vibrational Cooling

The entire process of a system transitioning from an excited "hot" state back to thermal equilibrium is referred to as vibrational cooling. In this process, the average vibrational population distribution shifts to lower energies and gets more spread out. The process of vibrational cooling can further be divided into multiple sequential and parallel steps of vibrational energy redistribution. There were models developed by Hill and Dlott that try to model the vibrational cooling process [11–13]. In these models, the vibrational cooling takes place in three energetic regimes: The high-frequency regime where a vibration relaxes into one or multiple other vibrations, the intermediate-frequency regime where a vibration relaxes into a phonon and a vibration, and the low-frequency regime where the vibration relaxes into two phonons.

1.2.2 Vibrational Energy Redistribution

In vibrational energy redistribution (VER), a vibration is deexcited, and its energy is transferred to other degrees of freedom. These degrees of freedom can be one or multiple other vibrations, phonons, or radiation. While the two former processes are fast, the relaxation of vibrational energy to radiation is a relatively slow process. VER is often also referred to as vibrational energy relaxation or simply vibrational relaxation (VR). The transfer of energy from one vibration to another mainly occurs through anharmonic coupling [14].

1.2.3 Anharmonic Coupling

In general, we can describe the vibration of two atoms as a harmonic motion if we only consider small displacements from the equilibrium bond distance. The potential energy surface U of any number N of normal modes, associated with their respective normal

coordinate Q_i, can be expressed as

$$U(Q_i) = \frac{1}{2}k_1Q_1 + \frac{1}{2}k_2Q_2 + ... + \frac{1}{2}k_NQ_N \ . \tag{1.32}$$

Here, k_i are the individual force constants of every normal mode i. If we solve the Schrödinger equation for this potential energy surface

$$\left[\sum_i^N -\frac{\hbar^2}{2m}\frac{\partial^2}{\partial Q_i^2} + U(Q_i)\right]\Psi(Q_i,t) = E\Psi(Q_i,t) \ , \tag{1.33}$$

we get a product of simple harmonic oscillator wave functions as a solution:

$$\Psi(Q_i,t) = \psi_1(Q_1)\cdot\psi_2(Q_2)\cdot \ ... \ \cdot\psi_N(Q_N) \tag{1.34}$$

These are completely decoupled harmonic oscillators. Let us take, for example, the CO_2 molecule, which has four normal modes. The symmetric stretching vibration which *should* be found at $\nu_1 = 1337\,\mathrm{cm}^{-1}$ (for reasons we will discuss later, we can not find it at this energy), two degenerate bending modes at $\nu_2 = 667\,\mathrm{cm}^{-1}$ and the asymmetric stretching mode at $\nu_3 = 2349\,\mathrm{cm}^{-1}$ [3]. If we excited this symmetric stretching vibration, the molecule would oscillate in this normal mode forever. However, this is not true for a real molecule. After a certain time, we would see the molecule executing a superposition of the bending mode and the symmetric stretch. This is because there is a strong anharmonic coupling between the symmetric stretching mode and the bending modes. To express this mathematically, we can add to Equation 1.32 a coupling term so that we can write it as

$$U(Q_i) = \left(\sum_i^{N\geq 2}\frac{1}{2}k_iQ_i\right) + k_{21}Q_2Q_1 \ . \tag{1.35}$$

Here, k_{21} is the coupling constant between normal coordinates Q_2 and Q_1. Figure 1.10 illustrates this more intuitively. Here, we can see the two-dimensional potential surface and the resulting deviation of the trajectory of a particle on this potential surface. Quantum mechanically, we can interpret this as a superposition of two vibrational wave functions. Considering a single molecule, it would oscillate back and forth between those two states. Upon measurement, the wave function will collapse, and we will find the molecule performing the vibration along either Q_1 or Q_2. If we took a spectrum of an ensemble of molecules, we would observe both lines belonging to Q_1 and Q_2.

This coupling is not limited to a pair of internal vibrational modes Q. Internal vibrational modes can also couple to external modes, denoted with q. External modes are, in this case, relative movements of the individual molecules of a crystal or molecular layer as well as movements of adsorbates relative to the adsorbent. Also, an arbitrary amount of internal and external modes can couple at the same time. In practice, the simplest case

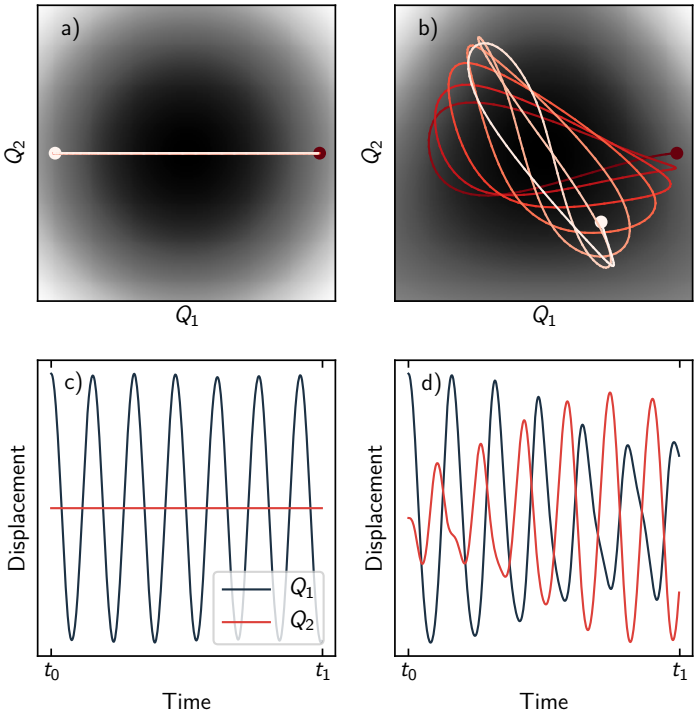

Figure 1.10: Classical illustration of anharmonic coupling between two normal coordinates Q_1 and Q_2: a) and c) - two uncoupled oscillators (see Equation 1.32). The initial displacement is only in the Q_1 coordinate. This does not change over time. All the energy stays in the Q_1 coordinate. b) and d) - Two anharmonically coupled oscillators (see Equation 1.35). Although the initial displacement is only in the Q_1 coordinate, the energy will distribute between both coordinates. The red dot indicates the initial displacement at time t_0. The displacement at time t_1 is indicated by the light dot. The gray colormap indicates the potential surfaces. A darker color indicates a low potential energy, a lighter color a higher potential energy.

of such an anharmonic coupling in a real molecule is the coupling between two internal modes with normal coordinates Q_i and Q_j and an external mode q_l, where the coupling term is

$$k_3 = k_{ijl} \cdot Q_i Q_j q_l \ . \tag{1.36}$$

Here, k_{ijl} is a matrix that describes the transition between the individual modes. There can also be higher-order coupling of the form $k_4 = k_{ijkl} \cdot Q_i Q_j Q_k q_l$. This case describes the coupling between three internal modes i, j, k and an external mode l. If a lower-order coupling like k_3 exists, this channel will usually dominate the rate of energy relaxation over the k_4 process [14].

1.2.4 Fermi Resonance

The closer the two normal modes are together in energy, typically the stronger the anharmonic coupling between those two modes becomes. In the CO_2 molecule, the symmetric stretch and the bending modes are not energetically close. However, the second excited state of the bending mode at an expected wavenumber of $\approx 2\nu_2 = 1334\,\mathrm{cm}^{-1}$ is energetically close. This is why the coupling is so strong for these two vibrational modes. There is another point that can be made here. In the Raman spectrum of CO_2, we do not find anything at $1337\,\mathrm{cm}^{-1}$ and $1334\,\mathrm{cm}^{-1}$. Instead, we find two strong modes at $1286\,\mathrm{cm}^{-1}$ and $1388\,\mathrm{cm}^{-1}$. This splitting is caused by a mixing of the two wave functions of the respective states and is called Fermi resonance. In the spectrum, the otherwise weak overtone "borrows" intensity from the strong fundamental transition. There are two conditions under which a Fermi resonance may occur. Firstly, the fundamental transition and the overtone have to be close in energy, and secondly, the symmetry of the vibrational modes has to be the same [3].

1.2.5 Condensed Matter and Gas Phase

We can differentiate between two kinds of systems when we study vibrational dynamics: gases and condensed matter. In gases, vibrational relaxation times are usually much longer than in condensed matter. In gases, the relaxation times are on a nanosecond time scale, whereas in condensed matter, the time scale is picoseconds [15]. Additionally, in the gas phase, molecules typically redistribute vibrational energy internally. This process is called intramolecular vibrational redistribution (IVR). An isolated molecule cannot transfer its energy to its surroundings or other molecules except by slow radiative processes [16]. Since in this work we are dealing with condensed matter, we will focus on it too when we take a look at the current state of research on vibrational dynamics in Chapter 1.3.

1.2.6 Coherent and Incoherent Methods

When investigating vibrational dynamics, we typically want to put the system in a non-equilibrium state by exciting vibrational modes. This can either be achieved by a stimulated Raman process or by IR absorption. When the system is out of its equilibrium, we can probe it with coherent or incoherent Raman scattering, fluorescence, or sum-frequency spectroscopy. Depending on the combinations of excitation and probing techniques, we can obtain specific information about the vibrational cooling process. With coherent methods, we can obtain information on the dephasing time T_2, collective beating, inhomogeneous broadening, and phonon lifetime. With incoherent methods, on the other hand, we can measure population relaxation times T_1 and energy redistribution and transfer [15]. In this work, we are using incoherent methods.

1.3 State of Research on Vibrational Dynamics

This chapter gives an overview of previous work related to dynamics of CH stretching vibrations in condensed matter. Specifically, we will address population relaxation times and proposed pathways of vibrational energy relaxation. In this regard, we will focus on adsorbates and liquids and disregard vibrational dynamics in the gas phase. Since, as discussed previously, energy relaxation times and pathways in the gas phase are not comparable to those in condensed matter.

1.3.1 Adsorbates

In 1989 Harris et al. [17, 18] performed pump-probe experiments on cadmium stearate adsorbed on a silver film to study the vibrational energy relaxation. The probe pulse was restricted to the same frequency as the pump pulse. For the symmetric methyl stretching vibration, they found a bi-exponential decay with the fast component having a time constant of 2.5 ps convoluted with the pump pulse and with the second component having a time constant of 165 ps. With a pump pulse energy of 10 to 30 µJ, they achieved an excited state population of 15 %. At wavenumbers of 2940 cm^{-1} and 2965 cm^{-1} – corresponding to the Fermi resonance and the asymmetric stretching vibration of the methyl group – only low excited state populations of 2 % to 3 % could be achieved. Here, only a fast recovery time constant and no slow component could be found.

In 1991 Harris et al. [19] performed similar pump-probe experiments on methylthiolate ($S-CH_3$) on an Ag(111) surface using the same technique as described previously. They, again, found a bi-exponential decay in the transient of the population of the CH_3 symmetric stretching mode. For this system, the fast component has a lifetime of 2.5 ps to 3.0 ps, and the slow component has a temperature-dependent lifetime decreasing with increasing temperature from 90 ps at 110 K to 55 ps at 380 K. They propose that the asymmetric CH_3 stretching modes and the overtone of the CH_3 asymmetric bending modes serve as intermediates in the vibrational energy relaxation pathway. The overtone of the asymmetric bending mode is coupled to the symmetric stretching mode by anharmonicity as well as by Fermi resonance.

Löbau et al. [20] conducted two-color pump-probe experiments on a monomolecular film of octadecyltrichlorosilane (OTS) ($CH_3(CH_2)_{17}SiCl_3$) chemisorbed on CaF_2. They used narrowband vSFS as a probing technique and an independently tunable IR pulse for excitation. The population lifetime of the CH_3 symmetric and asymmetric stretching vibration in these experiments was around 5 ps. They estimate an upper limit for the energy transfer time between the r^- and r^+ modes of 1.5 ps. The results are insofar noteworthy in that the population relaxation time is one order of magnitude faster than is the case in the experiments of Harris et al. [17–19] despite the systems being similar. With

pump energies of 20 µJ per pulse, they achieved a population of the excited vibrational state of 12 %. The probed system and the setup in this work are similar to those presented in this thesis. One big constraint, however, was the limitation to a narrowband probe-IR. This makes it impossible to observe a broad range of vibrational modes at the same time.

The same setup was used by Saß et al. [21] to investigate the vibrational energy transfer of ethyltrichlorosilane $CH_3CH_2SiCl_3$ chemisorbed on glass. They found a population relaxation time of 4.5 ps comparable to that of OTS [20]. In contrast, they found that the ground state re-populates slowly with a time constant of around 150 ps.

Bonn and coworkers performed measurements on lipid monolayers on H_2O and D_2O in a time-resolved SFG experiment with spectrally broad, 120 fs pump and probe pulses [22]. They evaluated the population relaxation time of the symmetric stretch of the CH_3 group to 3.6 ps. For the CH_3 asymmetric stretch, they found a much faster time constant of 0.8 ps. They attribute this difference in population relaxation times to a strong coupling between the CH_3 asymmetric stretch and the CH_2 vibrations. Also, the measurements show a comparably fast relaxation time of the CH_2 symmetric stretch, which they attribute to a fast delocalization of these vibrational modes. For dodecanol monolayers on D_2O, they found population relaxation times of 7.0 ± 0.5 ps for the CH_3 symmetric stretch and 1.5 ± 0.4 ps for the overtone of the CH_3 asymmetric bend. Like for the lipid monolayer, for the CH_3 asymmetric stretch of the dodecanol monolayer, they found a time constant of 0.8 ps [23].

Bonn et al. [23, 24] also performed 2D IR-pump/SFG-probe experiments on dodecanol monolayers on D_2O. The main difference to the experiment described before is that the pump pulse is spectrally narrow in this technique. Also, the spectra are recorded at a fixed pump-probe delay of 700 fs. The aim of these experiments was to gain information about the coupling of various vibrational modes instead of their dynamics. They found a strong coupling between the CH_2 asymmetric stretch and the CH_3 symmetric stretch. They also discuss a general approach to analyzing these types of experiments, specifically, the influence of hot band transitions on the observed spectra. These works are probably closest related to the experiments performed in the context of this thesis.

1.3.2 Liquids

For a detailed overview of early research on vibrational dynamics in liquids and solids, refer to the review of Laubereau and Kaiser from 1978 [15]. For a more recent overview of studies in polyatomic liquids, refer to Deàk et al. [16]. This section is a selection of the experiments and findings that are most relevant to this work.

The investigation of the vibrational population relaxation time of the symmetric CH_3 stretching vibration of trichloroethane (CH_3CCl_3) is one of the first experiments on vibrational dynamics in liquids. Laubereau et al. [25] found a time constant of $T_1 = 5.2$ ps

for the neat liquid, increasing to 29 ps with an added mole fraction of CCl_4 of 0.6. These findings illustrate that intermolecular vibrational energy transfer plays an important role in the vibrational relaxation process.

There is strong evidence that in ethanol and trichloroethane, the preferred pathway of vibrational relaxation is via the CH bending modes which have roughly half the frequency ($1450\,\mathrm{cm}^{-1}$) of the stretching modes [25–27]. Also, as is the case in adsorbates, the vibrational energy redistribution between neighboring states like CH stretching modes is rapid in liquids. Laubereau et al. [27] found in time-resolved pump-probe experiments that, for ethanol (CH_3CH_2OH), this happens on a time scale of $\sim$1 ps. They propose this rapid redistribution causes a quasi-equilibrium of population to form between all states at $\sim 2900\,\mathrm{cm}^{-1}$ including the various CH stretches as well as the overtones of the CH bends. They suggest the bottleneck for the subsequent vibrational energy relaxation is the decay to the fundamentals of the CH bending mode. For this relaxation step they found time constants of $\sim$20 ps [27, 28].

In 1981, Fendt et al. [29] highlighted the importance of the Fermi resonance between the CH_3 symmetric stretch and the overtone of the asymmetric CH_3 bending mode. Effectively, a strong Fermi resonance reduces the lifetime of the CH_3 stretching modes. In this case, this was shown by comparing the population relaxation times of the CH_3 symmetric stretch of methanol and ethanol. For methanol, having a strong Fermi resonance, they found a time constant of $T_1 = 1.5$ ps. In ethanol, with a significantly weaker Fermi resonance, the population relaxation time increases to as much as 20 ps which is in agreement with the population relaxation time found by Laubereau et al. [27, 28]. They also argue that the increased number of CH stretching modes in ethanol is partially responsible for the increased population relaxation time. This is the case because the vibrational energy equilibrates between all CH stretching modes. Subsequently, these serve as an energy reservoir that slows down the decay through the overtone of the asymmetric CH_3 bending mode.

In addition, Fendt et al. [29] proposed a model to estimate the population relaxation time T_1 of the initially excited state, which works surprisingly well:

$$T_1 = N\frac{(1+R)^2}{R} \cdot \exp\left(\omega/\Omega\right)^{2/3} T_{2,\mathrm{f}} \; . \tag{1.37}$$

Here, N is the number of initially excited states, and R is the intensity ratio between the Fermi resonance and the CH_3 symmetric stretch. We can calculate ω from the energy difference between the CH_3 symmetric stretch E_{CH_3} and its Fermi resonance E_{fr}. The relation is $\hbar\omega = E_{CH_3} - E_{\mathrm{fr}}$. For small molecules, Ω has typical values of $\sim 100\,\mathrm{cm}^{-1}$. $T_{2,\mathrm{f}}$ is the homogeneous dephasing time of the final state, i.e., the Fermi resonance. The dephasing time is related to the linewidth of the final state.

Deàk et al. [16] propose two possible pathways for the vibrational decay from the sym-

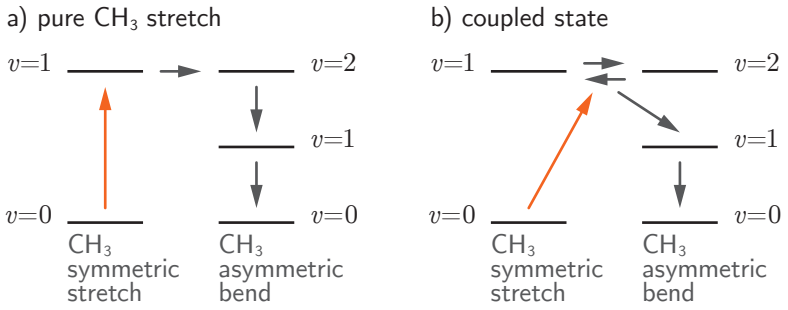

Figure 1.11: Possible pathways for the vibrational energy relaxation from the CH_3 symmetric stretch: a) The laser pulse pumps a pure stretching vibration which subsequently decays into the overtone of the asymmetric CH_3 bend. b) The laser pulse pumps a combination state of the symmetric stretch and the overtone of the bending mode, which then decays into low-energy vibrational modes. Adapted from Ref. [16]

metric CH_3 stretch via the Fermi resonance (see Figure 1.11 a) and b)). In the first case, the IR pulse populates a pure CH_3 stretching vibration. From here, the vibrational energy relaxes through the overtone of the asymmetric CH_3 bending mode to low energy modes. In the second case, the IR pulse excites a combination state of the stretch and bend overtone. Subsequently, this combination state decays into low energy modes. They argue that in the former case, the population of the overtone would build up as the population of the stretching mode decays. In the latter case, the population of the stretching and bending modes would decay simultaneously. Still, this is an open question to be addressed.

1.3.3 Summary and Open Questions

From these previous works, we can summarize some general findings regarding the dynamics of CH stretching vibrations. In general, these findings apply to adsorbates and molecular crystals as well as to liquids.

1. The vibrational energy redistribution between CH stretching modes of similar energy is fast in adsorbates as well as in liquids [25–27, 29–31].

2. Particularly, there is a strong coupling and fast energy exchange between the asymmetric CH_2 and the symmetric CH_3 stretching modes [22–24]. How fast this energy exchange takes place is still an open question.

3. The decay of the various CH stretching vibrations occurs through the CH bending modes and their overtones [16, 25–27]. Because of this, a strong Fermi resonance between the CH_3 symmetric stretch and the first overtone of asymmetric CH_3 bending mode significantly reduces the population relaxation time of the CH stretching vibrations [29]. The exact relaxation pathway is still unclear [16].

4. At least in liquids, intermolecular energy transfer plays an important role in the vibrational cooling process [25]. It is still unclear if and to which extend this is true for adsorbate systems. While this work will not address this question specifically, it lays the experimental foundation in order to address this question in the future.

5. Harris et al. [17–19] found slow and fast channels for the population relaxation of the CH_3 stretching modes in adsorbates. To explain the fast channel, they propose a fast equilibration of the vibrational energy between the CH stretches and the overtone of the asymmetric CH bend. They suggest a slow relaxation of the molecule from this overtone to the ground state is responsible for the slow channel.

In this work, we will try to address some of these open questions while we lay the foundation for further experiments that will hopefully reveal the vibrational relaxation dynamics of adsorbates in unprecedented detail.

2 Experimental

The first part of this chapter contains a detailed description of the sum-frequency spectrometer that we built. In the second part, we will discuss how we performed the measurements and how the data are processed before we do any further in-depth analysis with them in Chapter 3. The third part deals with the sample system that we investigate: A calcium arachidate monolayer deposited on a glass slide.

2.1 Vibrational Sum-Frequency Spectrometer

2.1.1 Setup

As part of this work, we built a novel spectroscopic system to perform the two-color pump-probe spectroscopy. The system consists of two parts. The first part, responsible for the broadband probing, is working with a repetition rate of 2 kHz and a pulse length of 290 fs. The second part of the system generates narrowband 15 ps pulses with a repetition rate of 1 kHz and serves as the pump laser. This section describes the most relevant components of the system.

Pump Laser (Pharos)

The core of the spectrometer we developed (see Figures 2.1 and 2.2 for reference) is the *Light Conversion: Pharos PH1* (Pharos) which generates laser pulses at around 1028 ± 5 nm at a repetition rate of 2 kHz and a pulse length of <300 ps. The output power is 3.8 W which results in pulse energies of 1.9 µJ. The output of the Pharos (B5 and B6) drives the *Light Conversion: Second Harmonic Bandwidth Compressor* (SHBC) harmonic generator as well as the *Light Conversion: Orpheus-Twins* (Twins) tunable optical parametric amplifier. It also seeds the *Ekspla: APL2210D-TR* diode-pumped Nd:YAG laser (B7) to ensure that the pulses from both parts of the system are synchronized.

Upconversion Pulse (SHBC)

The SHBC is generating the visible upconversion pulse (B1) used for the sum-frequency generation. Being the second harmonic of the output of the Pharos, the wavelength is at

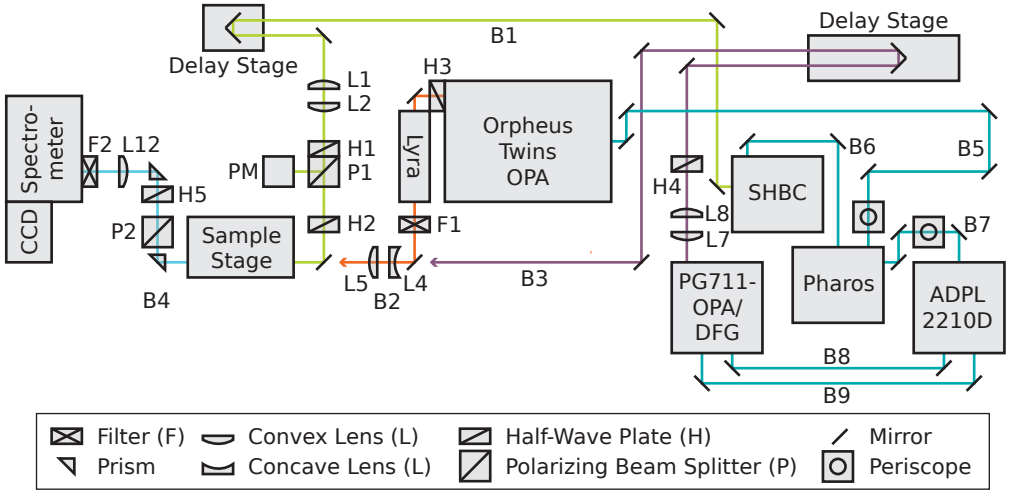

Figure 2.1: Schematic of the system setup

around 513 nm with a bandwidth of $<10\,\mathrm{cm}^{-1}$. The output power is adjustable by a built-in attenuator with a maximum output power of 66 mW. With a repetition rate of 2 kHz this results in maximum pulse energies of 33 µJ. The time the pulse hits the sample can be adjusted via a delay stage *Micos: Phytron / Micos SMC Controller* with a maximum displacement of 25 mm which corresponds to ∼167 ps and is adjustable in steps of 1 µm (∼6.6 fs). Lenses L1 and L2 form an adjustable telescope to control the expansion of the upconversion beam. Table 2.1 lists all lenses. With the telescope, it is possible to vary the spot size on the sample. The next component in the beam path is a polarizing beam splitter cube P1 with an upstream half-wave plate H1. These two components serve as an attenuator: P1 only transmits horizontally polarized light so that H1 controls the fraction of light that passes P1 and subsequently the laser power at the sample. P1 reflects the remaining portion into a power meter *Thorlabs: S121C*. By this, the approximate power at the sample can be recorded and monitored permanently. The polarization at the sample can be adjusted via half-wave plate H2. The beam is focused on the sample via lens L3 at an angle of 45° with respect to the surface normal (see Figure 2.2).

Probe Pulse (Orpheus-Twins)

The Twins are independently adjustable tunable optical parametric amplifiers. The experiments presented here use only one arm of the Orpheus for the broadband probe pulse. The probe pulse has a bandwidth of approximately $200\,\mathrm{cm}^{-1}$ (FWHM) and a nominal pulse duration of 300 fs at a repetition rate of 2 kHz. In connection with the *Light Conversion: Lyra* DFG unit the output wavelength is tunable in a range from 1300 nm to 19 500 nm with pulse energies ranging from 100 µJ to 0.1 µJ. In the spectral range of the CH stretching region, the maximum output power is 50 mW to 60 mW corresponding to 25 µJ to 30 µJ per pulse.

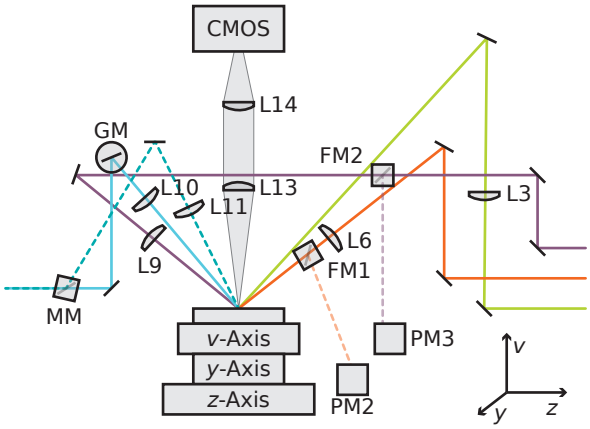

Figure 2.2: Schematic of the sample stage

Table 2.1: Lenses that are used in the experimental setup (see Figures 2.1 and 2.2). Positive focal lengths indicate a convex lens while the focal lengths of concave lenses are indicated with a negative value.

Lens	Material	Focal Length (mm)	Location
L1	BK7	75	Telescope Upconversion
L2	BK7	75	Telescope Upconversion
L3	BK7	500	Sample Focus Upconversion
L4	CaF_2	−40	Telescope Probe-IR
L5	CaF_2	25	Telescope Probe-IR
L6	CaF_2	100	Sample Focus Probe-IR
L7	CaF_2	75	Telescope Pump-IR
L8	CaF_2	75	Telescope Pump-IR
L9	CaF_2	150	Sample Focus Pump-IR
L10	BK7	125	SF Beam Collimator Probe
L11	BK7	175	SF Beam Collimator Pump
L12	BK7	150	Spectroscope Entrance
L13	BK7	75	Sample Camera
L14	BK7	75	Sample Camera

The *Lyra* DFG unit generates light at wavenumbers smaller than 2600 cm^{-1} ($\gtrapprox$3800 nm) and can be employed optionally. In contrast to the original configuration the *Lyra* is rotated 90° around the beam axis. We did this to avoid the use of a half-wave plate in the probe beam. In our experimental setup, the probe beam is only intended to hit the sample in *p*-polarization. However, in the original configuration, the output of the *Lyra* was polarized in such a way that it hit the sample in *s*-polarization. Half-wave plate H3, located between the *Orpheus* and the *Lyra*, can be employed optionally in case low-energy pulses from the DFG unit are needed. H3 rotates the polarization of both the signal and idler output of the *Orpheus* so that the polarization at the DFG crystal in the *Lyra* is correct.

F1 is an interchangeable highpass/lowpass filter and ensures that no unwanted signal/idler from the *Orpheus* or *Lyra* output is transmitted. The beam expansion and spot size on the sample can be controlled via lenses L4 and L5. For large changes in wavelength (∼1000 nm), the beam divergence changes significantly. Also, the refractive index of the lenses changes significantly for different wavelengths. In this case, L4 and L5 need to be adjusted manually for the specific wavelength. The beam is focused on the sample with L6.

A computer-controlled motorized mirror *Thorlabs: MFF101* can be moved into the beam path to direct the beam onto a *Thorlabs: TD10XP* power meter PM2 in order to determine the pulse energy at the sample. Typical energies at the sample are in the range from 12 µJ to 15 µJ per pulse in the CH stretching region. The beam is directed at the sample at an angle of 60° with respect to the surface normal.

Pump Pulse (PG711-DFG)

As mentioned earlier the *Pharos* is seeding the *APL2210D-TR* (B7) to ensure both the *Ekspla* and the *Light Conversion* part of the system run synchronously. The *Ekspla: APL2210D-TR* is generating pulses with a wavelength of 1064 nm (B8 and B9) at a repetition rate of 1 kHz (half the frequency of the *Pharos*) to pump the *Ekspla: PG711-DFG* unit which in turn generates the pulse that is used to pump the sample. The wavelength is tunable from 1540 nm to 16 000 nm with pulse energies ranging from 560 µJ to 3 µJ. The polarization in the idler regime (2340 nm to 3439 nm) is vertical whereas the polarization in the DFG regime (3440 nm to 16 000 nm) is horizontal.

The beam expansion and spot size on the sample can be controlled manually via a telescope consisting of lenses L7 and L8. With half-wave plate H4, the polarization of the laser can be adjusted. The delay of the pump beam can be adjusted via a *Micos: LS-180* translation stage with a maximum travel distance of 30.5 cm which results in a total delay of ∼1 ns. The beam is then focused onto the sample by lens L9 from the opposite side as the probe pulse at an angle of 60° with respect to the surface normal. The pump and probe pulses hit the sample from opposite directions to avoid detection of the sum-frequency signal generated by the pump and the upconversion pulse. In this configuration, the sum-frequency signal generated by the probe pulse and the upconversion pulse is reflected from the sample at an angle of 46.7°. The sum-frequency signal generated by the pump pulse and the upconversion pulse is reflected at an angle of 30.0° (both with respect to the surface normal and assuming an IR wavenumber of 2900 cm^{-1}).

Like with the probe-IR beam, a motorized flip mirror *Thorlabs: MFF101* can be employed to guide the laser on the *Thorlabs: TD10XP* power meter (PM3) to get the approximate pump pulse energy reading at the sample.

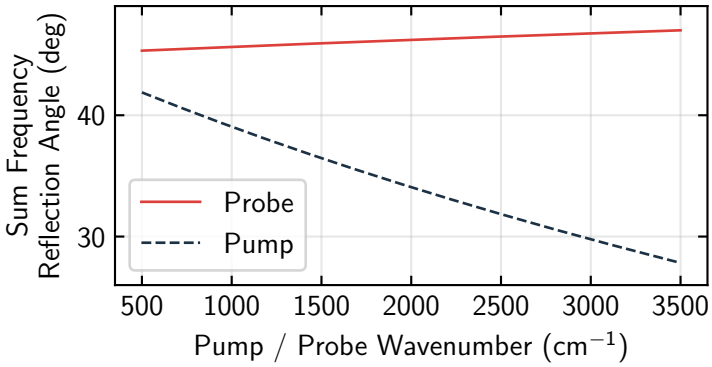

Figure 2.3: Calculated angles $\beta_{\mathrm{SF,r}}$ (see Figure 1.9) with respect to the surface normal of reflected sum-frequency signal generated by both the pump pulse and the probe pulse for different IR wavenumbers. The upconversion wavelength was set to 515 nm for the calculations. Incident angles of upconversion and IR beams correspond to those used in the experiment (45° and 60° respectively).

Sum-Frequency Signal (Probe)

The reflection angle of the sum-frequency beam that is generated by the upconversion pulse and the broadband IR probe pulse is not changing significantly with the IR wavenumber, as can be seen in Figure 2.3. The signal is collimated by lens L10 before it hits the galvanometer mirror GM (see Figure 2.2). The purpose of the galvanometer mirror is explained in detail later. The beam path uses two prisms instead of mirrors since these have slightly better reflection properties (see Figure 2.1). In order to select the appropriate polarization for the experiment, the beam passes a *Thorlabs: GTH10M-A* Glan-Thompson calcite polarizer. Half-wave plate H5 polarizes the sum-frequency into *p*-polarization since the grating and mirrors in the spectrometer have a better reflectivity for this polarization. The signal is focused on the slit of the spectrometer via lens L12. Since the upconversion beam and the sum-frequency signal have similar reflection angles (45.0° and 46.7°, there is still a significant amount of 515 nm light at the entrance to the spectrometer. This light is filtered by a *Thorlabs: FESH0500* shortpass filter F2 with a cut-off wavelength of 500 nm and a transmission region from 494 nm to 400 nm.

Spectrometer/CCD

The spectrometer used in the setup is an *Acton: SpectraPro-300i* imaging spectrograph in combination with *Andor: iXon Ultra 897* electron-multiplying charged coupled device (EMCCD). The spectrometer has a focal length of 300 mm and is equipped with a *Princeton Instruments* holographic grating optimized for the visible spectral range with a groove density of 2400 gr/mm. The CCD sensor has a resolution of 512 × 512 pixels, with each pixel having an edge length of 16 µm resulting in a spectral resolution of approximately

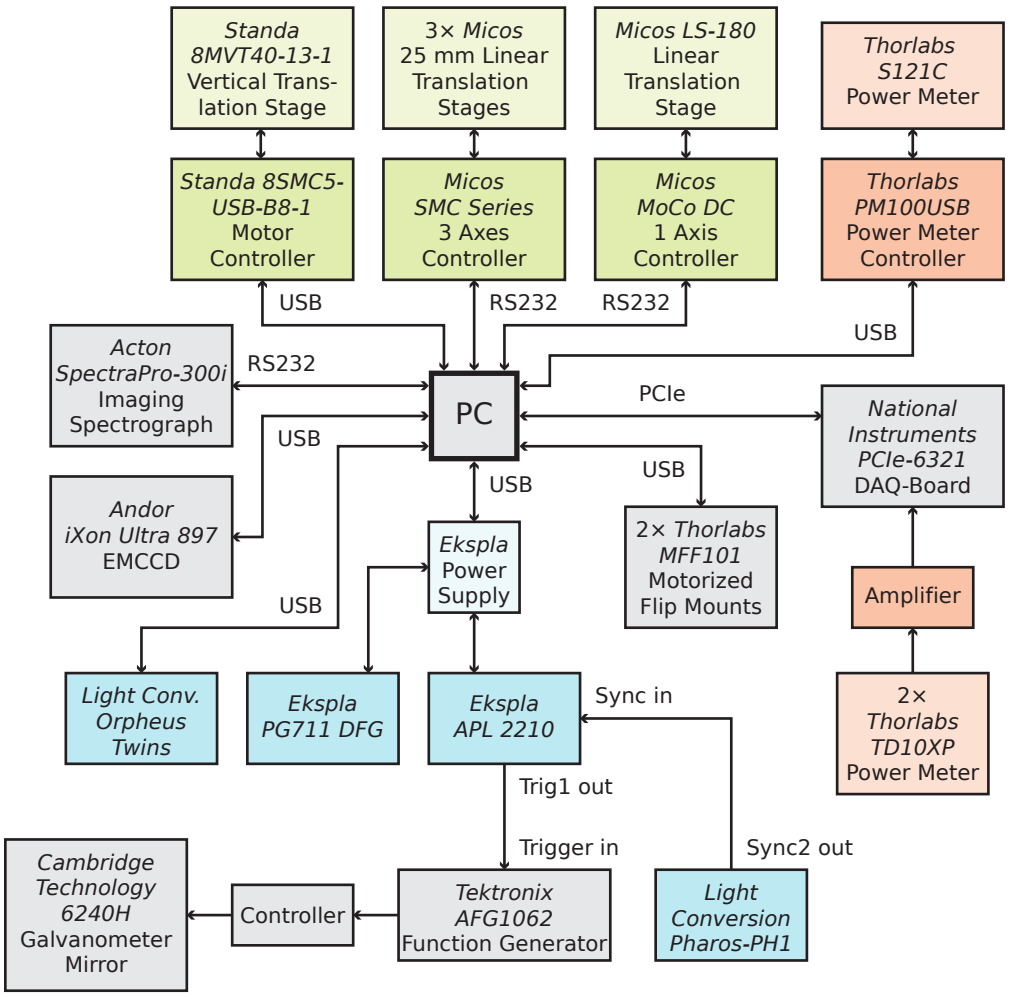

Figure 2.4: Schematic of all connected devices. The arrowheads indicate the directions of communication between the devices or between the devices and the PC.

$0.74\,\mathrm{cm}^{-1}$ per pixel. The configuration of the CCD camera for the experiments can be found in Section 2.2.1.

Sum-Frequency Signal (Pump)

Alternatively, the sum-frequency signal generated by the upconversion pulse and the IR pump pulse can be directed onto the CCD by manually putting in a mirror on a magnetic mount (MM) (see the dotted beam path in Figure 2.2). The signal is collimated by lens L11 passing the galvanometer mirror GM. The downstream path corresponds to that of the sum-frequency signal of the probe pulse. Being able to record the SF signal of the pump pulse is useful for two reasons. Firstly, it is needed to determine the temporal and spatial overlap between the pump and the upconversion pulse in case a non-resonant signal or an SFG-active vibrational mode is present. Secondly, this allows us to indirectly measure spectral characteristics of the pump pulse via generated non-resonant sum-frequency light.

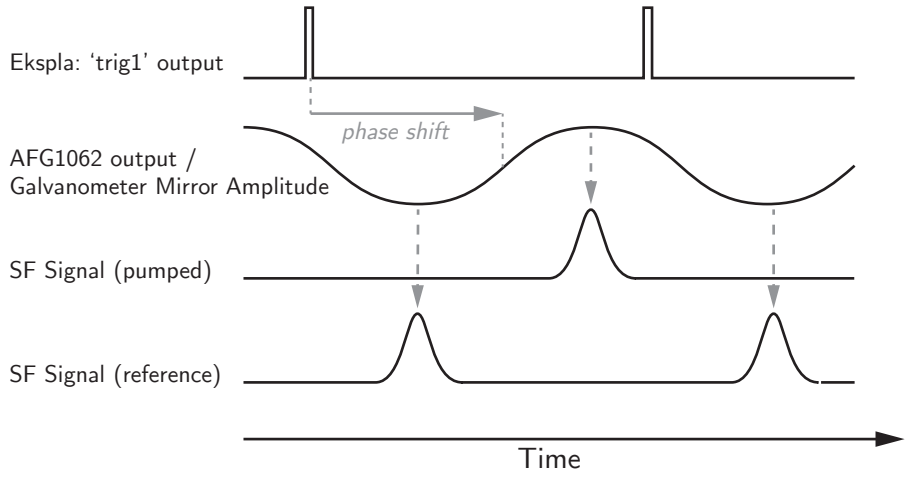

Figure 2.5: Schematic of the synchronization of the galvanometer mirror with *trig1* output of the *Ekspla: APL2210D-TR* and the pumped and reference sum-frequency signals. The phase of the function generator output can be shifted so in order for the maximum amplitude of the galvanometer mirror to coincide with the sum-frequency signals.

The geometry of the beam path is optimized for wavelengths in the CH stretching region. In Figure 2.3 it can be seen that the reflection angle of the SF signal is more dependent on the wavenumber of the IR-pump pulse than on the wavenumber of the IR-probe pulse.

Galvanometer Mirror

The galvanometer mirror GM (*Cambridge Technology: 6240H*) (see Figure 2.2) is used to record a pumped spectrum and an unpumped reference spectrum quasi-simultaneously. The angle of the mirror can be adjusted by applying a certain voltage. Because the upconversion and broadband IR probe pulses have a repetition rate of 2 kHz and the pump pulse only has a repetition rate of 1 kHz, the system is only pumped every other shot. When the upconversion and probe pulse hit the sample the next time after 500 µs, the system should be in equilibrium again. This is a prerequisite for the experiment but certainly fulfilled. The angle of the galvanometer mirror oscillates so that the signal of the pumped spectrum (signal) and the reference spectrum (reference) end up on the upper and lower half of the CCD sensor, respectively.

Synchronization A function generator (*Tektronix: AFG1062*) is triggered by the trigger output of the *Ekspla: APL2210D-TR*, generating a sine voltage profile with a frequency of 1 kHz. To ensure the synchronization of the galvanometer mirror and the laser pulses, only one period of the sine wave is generated per trigger pulse. Figure 2.5 illustrates the timing of the trigger and laser pulses with respect to the generated sine wave. The phase of the galvanometer mirror has to be shifted so that the pulses hit the mirror at the maximum absolute amplitude. This is done by monitoring the separation between the signal and

the reference on the CCD sensor and tuning the phase of the sine wave until both signals reach maximum separation. Additionally, the beam routing can be adjusted vertically by applying an offset voltage to the galvanometer mirror via the function generator. It is beneficial if the signal and the reference are equally separated from the center of the CCD sensor (see Section 2.2.3 for more detail).

Sample Table

The sample table is made of anodized aluminum and can be adjusted in all three spatial directions. The position of the sample table can be fully controlled by the computer. In the x-y-plane, corresponding to the plane of the sample table (see Figure 2.2 for reference), the translation is done via two *Micos* 25 mm linear translation stages that are connected to the x and y axes of a *Micos SMC Series* 3-axes controller. By being able to move the sample in the x-y plane, we can avoid deterioration of the sample during long measurements caused by high laser intensities in combination with dust particles settling on the sample.

The height of the sample is adjusted by a *Standa 8MVT40-13-1* vertical translation stage connected to a *Standa 8SMC5-USB-B8-1* controller. Computer control of the vertical position is crucial for the pump-probe experiments because with this, the overlap of the pump and probe pulses can be very finely tuned.

Via a CMOS camera mounted above the sample stage, a rough alignment of the sample height can be achieved. The optical filters in front of the sensor were removed to be able to observe near-IR light. Lenses L12 and L13 serve as a camera lens, allowing a magnified view of the sample (4×4 mm). For alignment, the z-axis is adjusted in such a way that the spot of the upconversion beam on the sample is visible in the center of the CMOS sensor. Maintaining the correct sample height can only be assured in this way if the beam path of the laser stays constant. This is done by adjusting the beam path to pass fixed apertures which are not shown in the figures.

Lenses L3, L6, and L9 focus the upconversion, IR probe, and IR pump beams onto the sample, respectively. Generally speaking, the shorter the focal length of a lens, the smaller the beam width at its focal point. The focal length of L6 (IR probe) is as small as possible (100 mm) while still allowing the upconversion beam to pass by the lens and achieving the highest possible field strength at the surface to maximize the SF intensity. For L3 (upconversion), we chose a relatively large focal length of 500 mm resulting in a big spot size relative to the probe-IR. This has the advantage that the alignment of the two spots is less critical for the intensity of the SF signal. Having a large focal length for L3 lowers the field strength of the upconversion pulse at the sample. However, this is not critical in this setup because of the high energy of the upconversion pulse of 30 µJ. The damage threshold of the calcium arachidate monolayers on glass is at around 20 µJ per pulse for the 515 nm upconversion light. The focal length of L9 (pump) with 150 mm is

Table 2.2: Laser models and specifications as provided by the manufacturers (LC: Light Conversion). The pulse energies of the Orpheus Twins and OPG711-DFG are typical around wavelengths corresponding to the C−H stretching region.

Model Name	Manufacturer	Wavelength Range	Pulse Length	Pulse Energy
Pharos	LC	1030 nm	290 fs	1.9 mJ
SHBC	LC	512 nm	5 ps	33 µJ
Orpheus Twins	LC	1.3 µm to 20 µm	300 fs	30 µJ
APL2210D-TR	Ekspla	1064 nm	30 ps	5.7 mJ
OPG711-DFG	Ekspla	1 µm to 16 µm	25 ps	120 µJ

restricted by the geometry of the sample stage (see Figure 2.2). A shorter focal length would lead to clipping of the SF signal. On the other hand, a larger focal length would widen the diameter of the beam in its focal point.

Theoretical Effective Susceptibilities

In this section, we take a look at how to calculate the intensities of the generated sum-frequency that we can expect with our setup. The only experimental parameter that directly affects the susceptibility of the sample itself are the incident angles of the IR and upconversion beams. Additionally, there are parameters that we will regard as invariant for a given experiment, but which also affect the theoretical susceptibility. These are the refractive index of the sample's substrate, the number of probed molecules, the intensities of both the upconversion and probe-IR beam, and the orientation of the molecules on the sample's surface. Knowledge about the theoretical susceptibilities is important for at least three reasons:

1. If we know the relative susceptibilities (and by that the relative intensities) that we can expect from different incident angles of our upconversion and IR beams, we can tweak the incident angles in such a way that increase the intensity of our sum-frequency signal.

2. The susceptibility is a complex number where the imaginary part contains valuable information about the expected phase of the signal. This helps us in assigning spectral features to specific modes because the phase directly affects the spectrum that is recorded.

3. We can calculate the relative intensity of a given mode in different polarization combinations. For example we can calculate the relative intensity of the symmetric stretching vibration of the CH_3 groups in *ssp* and *ppp* polarization ($I_{\mathrm{rel}} = I_{ssp}/I_{ppp}$). This helps us in identifying and interpreting spectral features.

The intensity of the generated sum-frequency I_{SF} is given by

$$I_{\mathrm{SF}} = \frac{8\pi^3\ \omega_{\mathrm{SF}}^2\ \sec^2\beta_{\mathrm{SF}}}{c^3 n_1(\omega_{\mathrm{SF}})\ n_1(\omega_{\mathrm{Vis}})\ n_1(\omega_{\mathrm{IR}})} \cdot \left|\chi_{\mathrm{eff}}^{(2)}\right|^2\ I_{\mathrm{Vis}} I_{\mathrm{IR}}\ , \tag{2.1}$$

where c is the speed of light. If we omit all the parameters which we may regard as invariant for a given experiment this reduces to

$$I_{\mathrm{SF}} \propto \left|\chi_{\mathrm{eff}}^{(2)}\right|^2 \cdot \sec^2\beta_{\mathrm{SF}}\ . \tag{2.2}$$

The effective second-order susceptibility $\chi_{\mathrm{eff}}^{(2)}$ is given by

$$\chi_{\mathrm{eff}}^{(2)} = [\hat{e}(\omega_{\mathrm{SF}}) \cdot L(\omega_{\mathrm{SF}})] \cdot \chi^{(2)} : [L(\omega_{\mathrm{Vis}}) \cdot \hat{e}(\omega_{\mathrm{Vis}})][L(\omega_{\mathrm{IR}}) \cdot \hat{e}(\omega_{\mathrm{IR}})]\ , \tag{2.3}$$

where $\hat{e}(\omega)$ is the unit polarization vector and $L(\omega)$ the Fresnel factor at the respective frequency ω. $\chi^{(2)}$ is the non-effective susceptibility and depends on the functional group's point group and the vibrational mode in question. The susceptibility forms the basis for the calculation of the expected effective susceptibilities.

For systems that are isotropic in the surface plane, the number of independent non-zero tensor elements of $\chi^{(2)}$ can be reduced from 27 to 4 in the case of $C_{3\mathrm{v}}$ symmetry. These four tensor elements are $\chi_{xxz} = \chi_{yyz}$, $\chi_{xzx} = \chi_{yzy}$, $\chi_{zxx} = \chi_{zyy}$ and χ_{zzz}. In the SF spectrum, these can be probed separately by using different polarization combinations (*ssp*, *sps*, *pss*, and *ppp*, respectively). Note that *ppp* does not probe χ_{zzz} alone but all independent tensor elements (see Equation 2.4). By applying the Fresnel factors to the susceptibility tensors, the following expressions are obtained for the effective susceptibility for the individual polarization combinations [32]:

$$\chi_{\mathrm{eff},ssp}^{(2)} = \ L_{yy}(\omega_{\mathrm{SF}}) L_{yy}(\omega_{\mathrm{Vis}}) L_{zz}(\omega_{\mathrm{IR}}) \sin\beta_{\mathrm{IR}} \cdot \chi_{yyz} \tag{2.4a}$$

$$\chi_{\mathrm{eff},sps}^{(2)} = \ L_{yy}(\omega_{\mathrm{SF}}) L_{zz}(\omega_{\mathrm{Vis}}) L_{yy}(\omega_{\mathrm{IR}}) \sin\beta_{\mathrm{Vis}} \cdot \chi_{yzy} \tag{2.4b}$$

$$\chi_{\mathrm{eff},pss}^{(2)} = \ L_{zz}(\omega_{\mathrm{SF}}) L_{yy}(\omega_{\mathrm{Vis}}) L_{yy}(\omega_{\mathrm{IR}}) \sin\beta_{\mathrm{SF}} \cdot \chi_{zyy} \tag{2.4c}$$

$$\begin{aligned}\chi_{\mathrm{eff},ppp}^{(2)} = & -L_{xx}(\omega_{\mathrm{SF}}) L_{xx}(\omega_{\mathrm{Vis}}) L_{zz}(\omega_{\mathrm{IR}}) \cos\beta_{\mathrm{SF}} \cos\beta_{\mathrm{Vis}} \sin\beta_{\mathrm{IR}} \cdot \chi_{xxz} \\ & -L_{xx}(\omega_{\mathrm{SF}}) L_{zz}(\omega_{\mathrm{Vis}}) L_{xx}(\omega_{\mathrm{IR}}) \cos\beta_{\mathrm{SF}} \sin\beta_{\mathrm{Vis}} \cos\beta_{\mathrm{IR}} \cdot \chi_{xzx} \\ & +L_{zz}(\omega_{\mathrm{SF}}) L_{xx}(\omega_{\mathrm{Vis}}) L_{xx}(\omega_{\mathrm{IR}}) \sin\beta_{\mathrm{SF}} \cos\beta_{\mathrm{Vis}} \cos\beta_{\mathrm{IR}} \cdot \chi_{zxx} \\ & +L_{zz}(\omega_{\mathrm{SF}}) L_{zz}(\omega_{\mathrm{Vis}}) L_{zz}(\omega_{\mathrm{IR}}) \cos\beta_{\mathrm{SF}} \cos\beta_{\mathrm{Vis}} \cos\beta_{\mathrm{IR}} \cdot \chi_{zzz}\end{aligned} \tag{2.4d}$$

Note that $\chi_{zyy} = \chi_{yzy}$ and therefore, the effective susceptibilities in *sps* and *pss* polarization merely differ only due to different Fresnel factors. For the four unique and non-zero tensor elements, we then get three expressions for a given vibrational mode. For the symmetric stretching vibration of the methyl group (or more general for every group with C_{3v}

symmetry), these are

$$\chi_{XZX} = \chi_{ZXX} = \chi_{YZY} = \chi_{ZYY} = \frac{1}{2} N_s \beta_{ccc} (\langle \cos\theta \rangle - \langle \cos^3\theta \rangle)(1-r) \tag{2.5a}$$

$$\chi_{XXZ} = \chi_{YYZ} = \frac{1}{2} N_s \beta_{ccc} [\langle \cos\theta \rangle (1+r) - \langle \cos^3\theta \rangle (1-r)] \tag{2.5b}$$

$$\chi_{ZZZ} = N_s \beta_{ccc} [r \langle \cos\theta \rangle + \langle \cos^3\theta \rangle (1-r)] \, . \tag{2.5c}$$

For the antisymmetric stretching vibration of a functional group with C_{3v} symmetry, the susceptibilities are calculated by

$$\chi_{XZX} = \chi_{ZXX} = \chi_{YZY} = \chi_{ZYY} = \frac{1}{2} N_s \beta_{caa} \langle \cos^3\theta \rangle \tag{2.6a}$$

$$\chi_{XXZ} = \chi_{YYZ} = -\frac{1}{2} N_s \beta_{caa} (\langle \cos\theta \rangle - \langle \cos^3\theta \rangle) \tag{2.6b}$$

$$\chi_{ZZZ} = N_s \beta_{caa} (\langle \cos\theta \rangle - \langle \cos^3\theta \rangle) \, . \tag{2.6c}$$

Here, N_s is the number density of molecules, β the hyperpolarizability tensor and $r = \beta_{acc}/\beta_{ccc}$. θ is the tilt angle of the symmetry axis of the molecule relative to the surface normal. Not every molecule orients itself with the same angle relative to the surface normal. The angled brackets $\langle\rangle$ indicate an angular distribution of the tilt angle.

The hyperpolarizability ratio r is connected to the Raman depolarization ratio ρ by

$$\rho = \frac{3}{4} \left(1 + \frac{5}{4} \left(\frac{2r+1}{r-1} \right)^2 \right)^{-1} \, . \tag{2.7}$$

The ratio depends both on the functional group as well as on the molecule itself. For the methyl group, it ranges between 1.7 and 4.0 [33]. For the calculations in this work, we assumed a value of 1.9.

The Fresnel factors in Equation 2.4 [34] can be calculated by

$$L_{xx}(\omega) = \frac{2 n_1(\omega) \cos\beta_\mathrm{t}}{n_1(\omega) \cos\beta_\mathrm{t} + n_2(\omega) \cos\beta_\mathrm{i}} \tag{2.8a}$$

$$L_{yy}(\omega) = \frac{2 n_1(\omega) \cos\beta_\mathrm{i}}{n_1(\omega) \cos\beta_\mathrm{i} + n_2(\omega) \cos\beta_\mathrm{t}} \tag{2.8b}$$

$$L_{zz}(\omega) = \frac{2 n_2(\omega) \cos\beta_\mathrm{i}}{n_1(\omega) \beta_\mathrm{t} + n_2(\omega) \cos\beta_\mathrm{i}} \cdot \left(\frac{n_1(\omega)}{n'(\omega)} \right)^2 \, . \tag{2.8c}$$

(See also Figure 1.9 for reference). The refractive index n' in Equation 2.8c is that of the interface between media 1 and 2. Often this interfacial layer is only one or a few monolayers of molecules thick. Therefore, its refractive index may differ from that of the

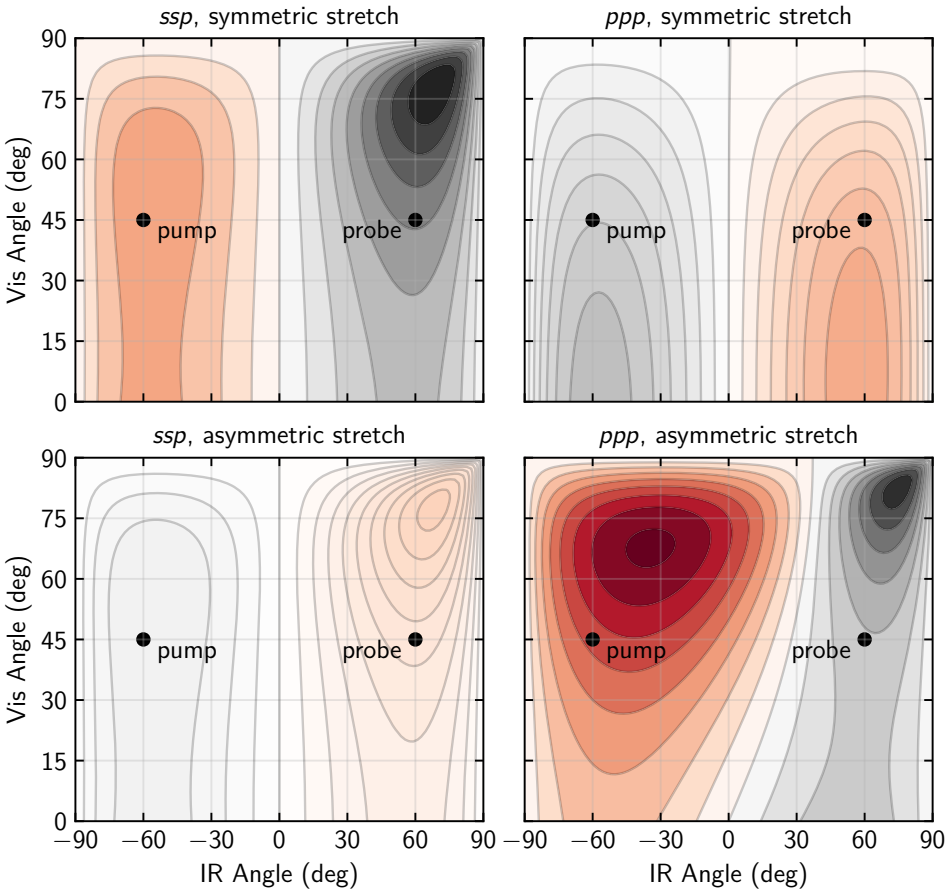

Figure 2.6: Theoretical effective susceptibilities ($\chi^{(2)}_{\text{eff}} \cdot \sec^2 \beta$) for *ssp* polarization (left column) and *ppp* polarization (right column) for both the symmetric stretch (top row) and the antisymmetric stretch (bottom row) for the CH_3 group as a function of the IR and visible pulse incident angles. The lightness of the color resembles the value of the effective susceptibility, whereby a higher lightness means a lower absolute effective susceptibility. Areas shaded in red indicate negative effective susceptibilities, whereas areas shaded in gray indicate positive effective susceptibilities. The effective susceptibilities are relative to one another between polarization combinations but not between the two vibrational modes. For the calculation, we assumed a normally distributed tilt angle with a mean of 0° and a standard deviation of 15°. The refractive indices are $n_1(\omega_{SF}) = n_1(\omega_{Vis}) = n_1(\omega_{IR}) = 1$, $n_2(\omega_{SF}) = 1.53$, $n_2(\omega_{Vis}) = 1.52$ and $n_2(\omega_{IR}) = 1.41$. The hyperpolarizability ratio was set to $r = 1.9$.

bulk material. The value of n' can be estimated by a local-field correction and in case of $n_1 = 1$ may be obtained [34] from the expression

$$\left(\frac{1}{n'}\right)^2 = \frac{4n_2^2 + 2}{n_2^2(n_2^2 + 5)} \,. \tag{2.9}$$

With this, we can calculate the susceptibilities we can expect for a calcium arachidate monolayer for our particular setup. The calculated susceptibilities are shown in Figure 1.9.

2.1.2 Laser Pulse Characterization

Cross-correlation measurements are a good way of determining the temporal profile of laser pulses. The cross-correlation between the pulses in question can be obtained by recording the frequency-resolved sum-frequency signal generated by the two pulses in question. The time of incidence of one of the pulses can be altered by delay stages. To generate the SF signal, we use the surface of a gold crystal. In principle, this can be any other material that is SFG active if it has the two following properties: 1) The intensity of the generated SF signal does not vary over the spectral width of the two laser pulses involved, i.e., we have a non-resonant signal that does not change in the wavelength range of interest. 2) The coherence time of the excitations is shorter than the duration of the pulses. A long coherence time would have the effect of broadening the SF signal in time, thus stretching its temporal profile. Both properties are valid for gold surfaces. We can not only measure the temporal but also the spectral cross-correlation of the two pulses in question. Recoding the sum-frequency signal, we are limited to two out of three possible pulse combinations. These combinations are SHBC/Twin and SHBC/PG711 since we need the upconversion pulse to generate a sum-frequency signal that is detectable by our system.

By cross-correlating the SHBC and the Twin pulse on the one hand and the SHBC pulse and the PG711 pulse, on the other hand, we can obtain the following parameters:

1. The pulse length of the *SHBC* is accessible by cross-correlating it with the *Twin* pulse. Since the nominal pulse length of the *Twin* is ∼300 fs it should not broaden the signal obtained by the cross-correlation significantly.

2. We can obtain the pulse length of the *PG711* by cross-correlating it with the *SHBC*. The same argument as before applies here: We can expect that the *SHBC* pulse is much shorter than the *PG711* pulse. Therefore the cross-correlation mainly measures the width of the *PG711* pulse.

3. From the cross-correlation with the *SHBC* the spectral width of the Twin, since the Twin pulse is much shorter than the SHBC pulse.

4. From the pulse lengths, we may deduce the bandwidth limit of the longer of the two cross-correlated pulses.

5. From the spectral width of the SF signal generated by cross-correlation of the SHBC and PG711, we may conclude the spectral width of these pulses.

6. Also, we can determine if a chirp (temporal change of the spectral profile) is present in the SHBC and PG711 pulses.

From these parameters, two are especially important. Firstly, the length and secondly, the spectral width of the pump pulse. The length is relevant for the interpretation of the transients we record in the pump-probe experiments. This is the case because the data will be convoluted with the temporal profile of the pump pulse. We also want to know the spectral width to ensure that the bandwidth is sufficiently narrow to excite only one specific vibrational mode and not multiple ones. If we assume that the pulses are bandwidth limited, we can get information on the duration and spectral width of the pulses that are involved in the experiment. This is done by solving the time-bandwidth-product (TBWP) for the pulse duration $\Delta\tau$ or the bandwidth $\Delta\tilde{\nu}$:

$$\mathrm{TBWP} = \Delta\tau \cdot \Delta\tilde{\nu} \cdot c \tag{2.10}$$

For a gaussian pulse the TBWP is ≈0.44 and for a sech^2 shaped pulse it is ≈0.315 Since the temporal and spectral profiles of the pulses are not ideal, the values we will calculate from the TBWP are just the lower limits of the pulse lengths and bandwidths.

In the following, we will determine the pulse lengths and bandwidths as described above. The pulse lengths were determined by integrating the data in the frequency dimension. For every pulse, the spectral width was determined at the time step that showed the strongest signal. Note that the spectral width of a pulse should generally not be time-depended. A time dependency of the spectral width should only occur in a chirped pulse.

Cross-Correlation SHBC - Twin

Figure 2.7 shows the temporal profile of the SHBC pulse. It is worthy to note that we do not consistently get such a "clean" temporal profile as the data represented by the solid line suggests. Depending on the state of the pump laser and beam alignment, it may be that the temporal profile looks more like the dashed/dotted lines in Figure 2.7. Since the Twin pulse has a nominal pulse length of ∼300 fs FWHM, we may assume that the signal we get from the cross-correlation closely resembles the temporal profile of the SHBC pulse. Therefore it is safe to say that the pulse length of the SHBC is ∼2.7 ps FWHM.

It is possible to deduce the bandwidth of the SHBC from its pulse length. If we assume the length of the SHBC pulse is bandwidth limited, for a Gaussian pulse, we get

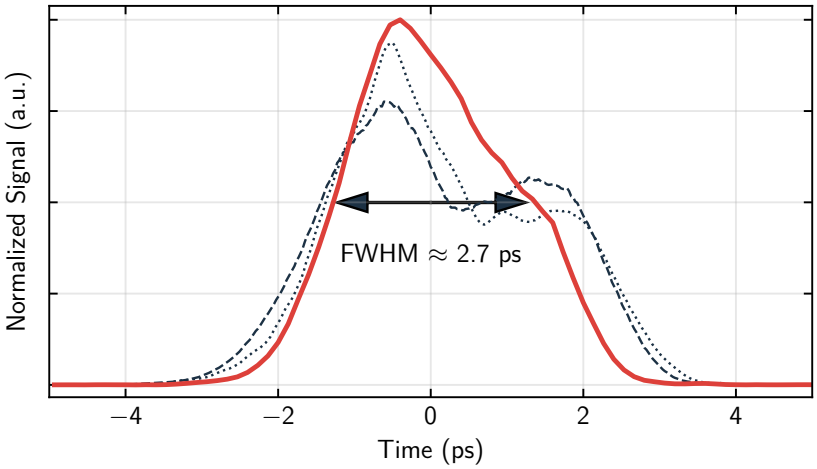

Figure 2.7: Typical cross-correlations between the broadband IR pulse of the *Orpheus Twin* and the upconversion pulse of the SHBC. The plot shows three cross-correlations measured on three different days. The FWHM value was taken from the plot marked in red.

a spectral width of $\geq$5.5 cm^{-1} FWHM. If we assume a $sech^2$ pulse, the spectral width is $\geq$3.9 cm^{-1} FWHM. From the SHBC's specifications, we expect a bandwidth of <10 cm^{-1} (see Section 2.1.1). The lower bandwidth limit we found corroborates this.

Figure 2.8 shows both the temporal and the spectral profile of the cross-correlation signal. The data reveal a spectral width of the Twin of 230 cm^{-1} FWHM. For the cross-correlation, the central wavelength of the Twin was set to 3450 nm ($\sim$2900 cm^{-1}) which corresponds to the CH stretching region that we focus on in our experiment. Note that the spectral profile of the Twin strongly depends on the center wavelength. If we assume that the spectral profile of the Twin is limited by the time-bandwidth-product (TBWP), the Twin has a pulse duration of >70 fs assuming a Gaussian profile. This value is much shorter than the nominal 300 fs pulse length of the *Pharos* pump laser so that we can assume that the pulse duration of the Twin is much longer than the TBWP suggests.

The data in Figure 2.8 suggests a chirp of the Twin pulse. We can see that the SF signal shifts to higher wavenumbers with the duration of the pulse. In the case shown here, the wavenumber shift is 15 cm^{-1}. Other cross-correlation measurements show shifts from 4 cm^{-1} to 20 cm^{-1}. We can assume that the wavenumber shift is not due to a chirp in the SHBC pulse but shows that the center wavelength of the Twin shifts with the duration of the pulse. The data of the cross-correlation between the SHBC and the PG711 corroborates this claim.

Cross-Correlation SHBC - PG711

Figure 2.9 shows the temporal profile of the cross-correlation between the SHBC pulse and the PG711 pulse. It shows an FWHM of 16 ps. Since we evaluated the length of the pump pulse to be 2.7 ps, we can assume that the temporal width of the cross-correlation signal closely resembles the length of the PG711 pulse.

The spectral width of the cross-correlation signal that is shown in Figure 2.8 is more complicated to decipher. This is because both the SHBC and PG711 pulse are close in spectral width. Nominally this is $<10\,\mathrm{cm}^{-1}$ for the SHBC and $5\,\mathrm{cm}^{-1}$ for the PG711. Additionally, the resolution of the spectrometer also broadens the signal. From the data, it is safe to say that neither pulse is broader than $9.7\,\mathrm{cm}^{-1}$. From the TBWP, we get a lower bandwidth limit for the PG711 pulse of $0.9\,\mathrm{cm}^{-1}$. For the SHBC, we get a lower pulse length limit of 1.5 ps which is well below the 2.7 ps that we evaluated from the cross-

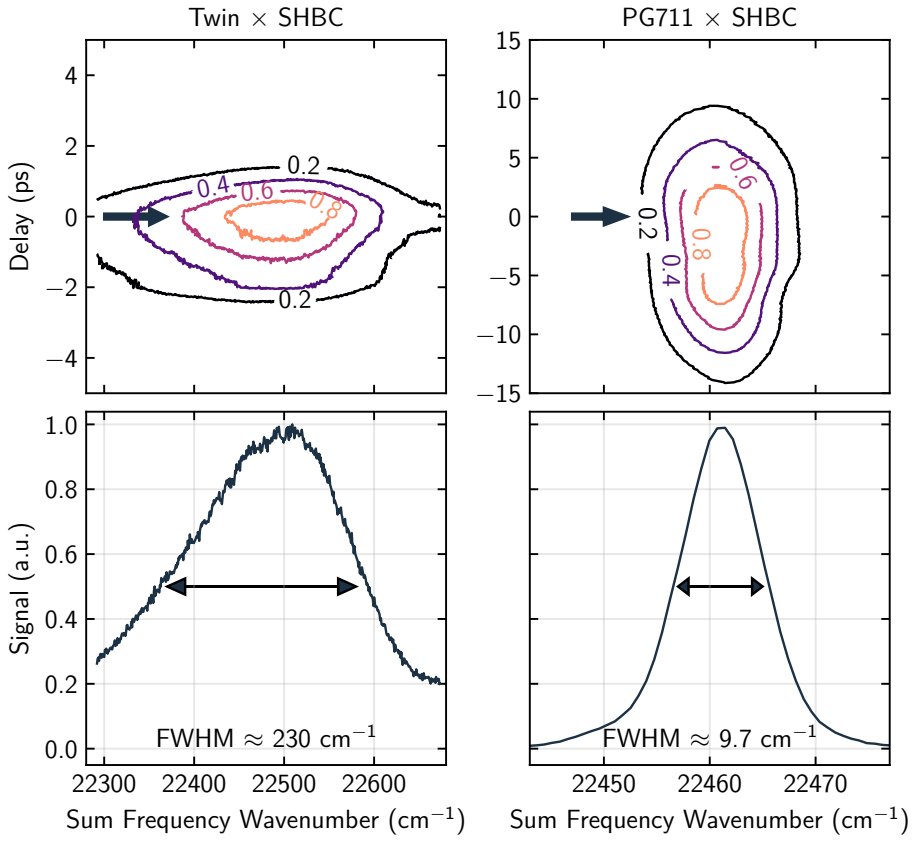

Figure 2.8: Cross-correlation data of the Twin and the SHBC pulses (left column) and the PG711 and SHBC pulses (right column). The upper plots show the SF signal in both time and frequency dimensions. The signal is normalized to a maximum value of 1.0. The arrow indicates the delay at which the maximum signal was detected. The bottom two plots show the frequency-dependent cross-correlation signal at the delay indicated by the arrows in the upper plots. The FWHM of the signal is indicated by the double-headed arrows. The time-dependent cross-correlation signal is shown in Figures 2.7 and 2.9.

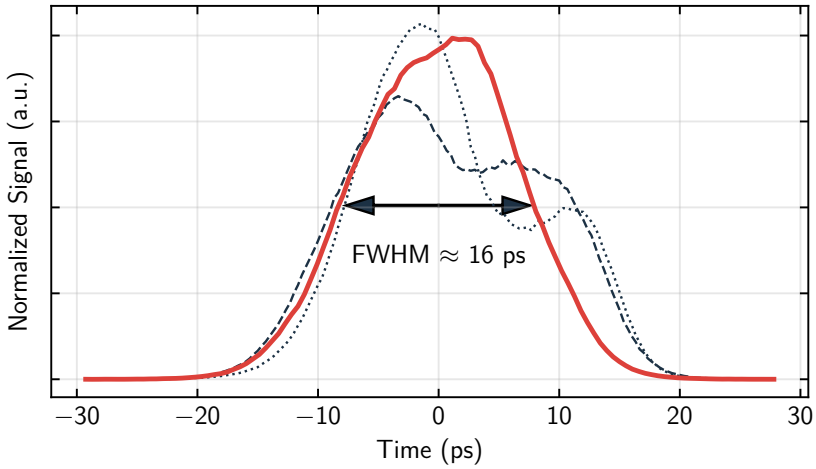

Figure 2.9: Cross-correlation between the pump-IR pulse of the *PG711 DFG* and the up-conversion pulse of the SHBC. The plot shows three cross-correlations measured on three different days. The FWHM value was taken from the plot marked in red.

correlation with the Twin pulse. The cross-correlation signal of the SHBC pulse with the PG711 pulse does not show a significant chirp.

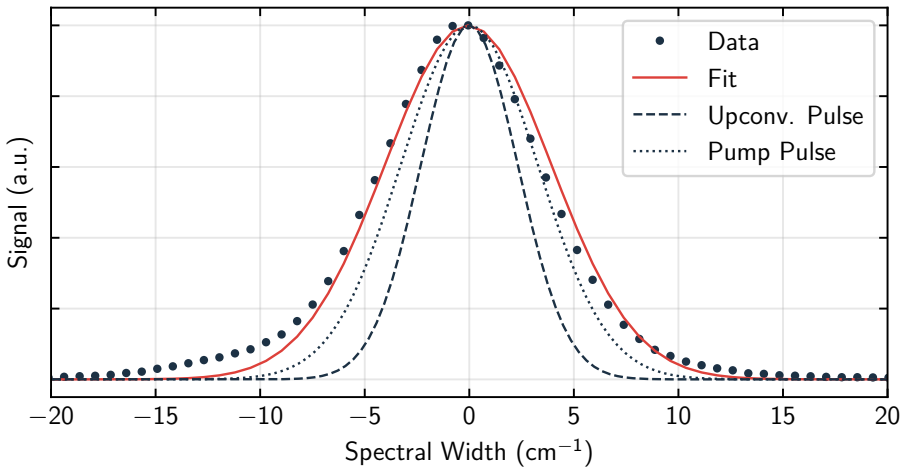

Figure 2.10: Illustration of how we can use the spectral cross-correlation data of the SHBC with the PG711 (black dots) and the minimum spectral width of the SHBC pulse that we obtained with the TBWP (dashed line) to calculate the maximum spectral width of the PG711 pump pulse (dotted line). The red line is a Gaussian fit to the black data points.

PG711 Bandwidth In order to find the bandwidth of the PG711 pump pulse, we can try to deconvolute the cross-correlation signal that is giving us the combined spectral shape of the SHBC and the PG711 pulse. The data from Figure 2.8 reappear in Figure 2.10 as

the black dots. In this case, absolute wavelengths do not matter, so we shift the center wavenumber to 0. We can take the lowest possible spectral width of the SHBC pulse that we determined via the TBWP ($5.5\,\mathrm{cm}^{-1}$) and find a gaussian spectral profile for the PG711 so that cross-correlating these two resembles the data points. This yields a maximum spectral width of $7.7\,\mathrm{cm}^{-1}$ FWHM for the PG711 pulse.

We can conclude that the pulse used to pump the system (PG711) has a pulse duration of $\sim$16 ps and a spectral width of $0.9\,\mathrm{cm}^{-1}$ to $7.7\,\mathrm{cm}^{-1}$. With this, it is spectrally narrow enough to be able to pump specific vibrational modes of the system in question. The data from the cross-correlations are summarized in, Table 2.1.2. Determining the real bandwidth of the SHBC pulse bandwidth instead of just a lower limit would help in finding a more accurate bandwidth value for the PG711 pulse. The pulse length of the PG711 is the limiting factor in determining the rates of energy redistribution in our system. We will not be able to observe processes that are faster than the pump pulse duration.

Table 2.3: Data obtained from the cross-correlation between the upconversion pulse ($SHBC$) and the probe pulse ($Twin$) / upconversion pulse and pump pulse ($PG711$). All values are given in FWHM. The bandwidth limits (BWL) apply to the shorter shorter of the two cross-correlated pulses, the time limits (TL) apply to the broader of the two pulses. For the time-bandwidth product we assume a gaussian pulse.

	Experimental		TBWP (Gaussian)	
Cross-Correlation	$\Delta\tau$	$\Delta\tilde{\nu}$	BWL	TL
SHBC - Twin	2.7 ps	$230\,\mathrm{cm}^{-1}$	$>5.5\,\mathrm{cm}^{-1}$	>70 fs
SHBC - PG711	16 ps	$9.7\,\mathrm{cm}^{-1}$	$>0.9\,\mathrm{cm}^{-1}$	>1.5 ps

2.2 Data Recording and Processing

This section describes the general procedure for recording and processing sum-frequency spectra with a broadband SFG setup. Additionally, it is described how to deal with spectra containing non-resonant background versus spectra that do not. In addition, we illustrate the procedure for processing the data of pump-probe experiments, both for varying pump wavelengths, as well as different pump delays.

2.2.1 Recording Spectra

Throughout this chapter, we use the term *frame* to describe a single image from the CCD. In this sense, a frame is the raw data from the camera. A fully processed spectrum is composed of multiple frames. These are *spectra frames*, which hold the spectral information, *dark frames* containing information about the background signal, and *flat frames*, which we use to normalize the spectrum.

Spectra Frames

Even with a broadband SFG setup, it may not be possible to probe the entire spectral region of interest at once. For example, at a wavenumber of around $3000\,\mathrm{cm}^{-1}$, the FWHM of the infrared probe pulse is approximately $150\,\mathrm{cm}^{-1}$, whereas the entire area of the CCD sensor covers a spectral range of about $375\,\mathrm{cm}^{-1}$. Therefore, if we want to probe a spectral range broader than the spectral width of the IR probe pulse, the central wavelength of the probe-IR has to change during the acquisition of a spectrum. In practice, there are two possibilities to illuminate the entirety of the sensor:

1. The central wavelength of the IR changes *frame-by-frame*.
2. The central wavelength of the IR changes during the acquisition of a *single frame*.

Figure 2.11 illustrates both approaches. Uniform illumination of the sensor is important because if we record the spectrum with just a single central wavelength, the signal will be low where the IR intensity is low. This would cause a low signal-to-noise ratio at the edges of the CCD. In this work, we only use the *frame-by-frame* method. The reason for doing this is explained later in this section.

Dark Frames

It is also necessary to record so-called dark frames in addition to the spectrum. Even if no photons hit the CCD sensor, its pixels will accumulate electrons due to heat. One area of the sensor might be warmer than other areas or, there can be "hot" and "cold" pixels which are not equally sensitive to heat. This leads to an unevenly distributed average count of

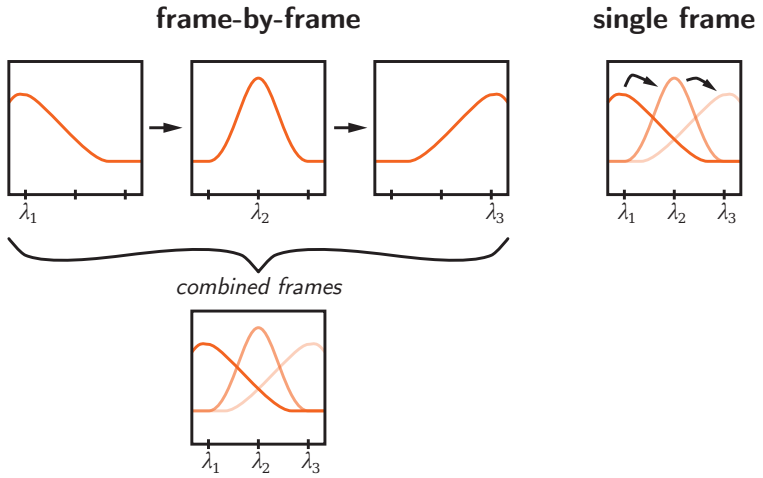

Figure 2.11: Illustration of possible acquisition approaches to illuminate the CCD sensor uniformly. In *frame-by-frame* acquisition (left), frames with different central IR wavelengths are recorded separately and later combined in data processing. in *single frame* acquisition (right), the central IR wavelength changes during the exposure time. Both approaches allow for a relatively uniform illumination of the entire sensor area.

electrons across the sensor. The count of these thermal electrons increases proportionally with exposure time [35].

Another source of electrons that causes an unwanted signal on the CCD is stray light. Stray light originates for the most part from the upconversion pulse. However, also other light sources in the laboratory can contribute to the stray light. Again, the stray light is typically not uniformly distributed across the sensor and varies between measurements. Also, the count of these photoelectrons generated in the CCD sensor is proportional to the exposure time.

In order to account for these two phenomena, we need to subtract our dark frames from our spectrum frames. For the recording of the dark frames, it is crucial to have the exposure time set to the same value as for the spectrum frames. This way, we ensure that the same amount of stray light photons hit the sensor as do in the spectrum frames and that the same amount of thermal electrons accumulate. To record the dark frames, we close the shutter of the probe-IR laser so that no sum-frequency signal is generated. This way, roughly the same amount of stray light should hit the sensor as with an open shutter. This disregards stray light originating from the probe-IR, which can, however, be neglected because of the insensitivity of the CCD sensor towards infrared light.

Subtracting dark frames increases random noise in our spectrum since the dark frames are noisy themselves. The noise we are inducing can be reduced by taking multiple dark frames and averaging them. The standard deviation of the counts in this averaged dark image decreases with a factor of $1/\sqrt{N}$ where N is the number of dark frames taken.

Flat Frames

As previously mentioned, it is not possible to illuminate the sample with a spectrally uniform IR probe pulse. Even if we take multiple frames with slightly different IR photon energies, there are always slight variations in IR intensity depending on the frequency. Another problem arises when we are operating at frequencies where the probe-IR is partially absorbed by molecules in the air like H_2O or CO_2. With fewer photons at a given IR frequency hitting the sample, fewer corresponding sum-frequency photons are generated. Therefore, to normalize our spectrum, we have to "boost" the spectral areas of low probe-IR power. Ultimately this is achieved by dividing the obtained spectrum by our flat image. We will discuss this in more detail later.

To obtain flat frames, we have to determine the power of the probe-IR at the sample. We can achieve this by generating a non-resonant sum-frequency signal. A suitable material for this is, for example, gold. Gold gives a strong non-resonant signal which is practically constant over the relevant spectral range. Therefore, the sum-frequency signal we detect with our CCD camera is proportional to the corresponding IR power at each wavenumber. This method also accounts for possible absorption or clipping of the generated sum-frequency beam between the sample and the CCD. In contrast to the dark frames, the flat frames do not require the same exposure time as the spectrum frames. However, as we alter the exposure time and the reflective properties of the sample, we also change the amount of stray light hitting the sensor. For this reason, we also have to take dark frames for our flat frames in the same manner as we do for our spectrum frames.

Figure 2.12 shows the recorded spectrum frames and corresponding flat frames alongside their dark images for a hexadecanethiol SAM on gold. For this example, five spectrum frames and five dark frames were recorded. The exposure time for the spectrum frames and the flat frames was set to the same value. The flat frames were recorded with a Au(111) crystal right after the spectrum frames.

Frame-by-Frame versus Single Frame Acquisition

As mentioned earlier, we use the *frame-by-frame* approach instead of the *single frame* approach to uniformly illuminate the CCD sensor. Out of the following reasons, the *frame-by-frame* approach is preferable:

1. Transitioning between central probe wavelengths takes up to 1 s. During this transition, the spectrum of the probe-IR is highly unpredictable due to optical components moving inside the *Orpheus*. In the *single frame* approach, this transition happens during acquisition. If we acquire the single frame with an exposure time of ∼120 s, this transition time is comparability low. However, we may acquire the flat frames with a much lower exposure time of just a few seconds. The transition time now

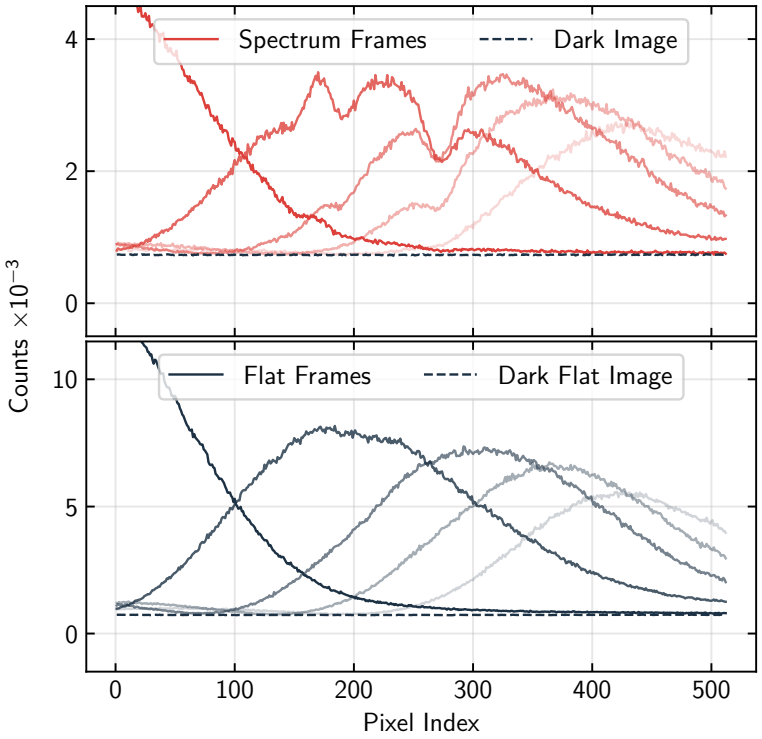

Figure 2.12: Spectra frames (upper plot) and corresponding flat frames (lower plot) of a hexadecanethiol SAM on gold alongside their matching averaged dark images. These frames were recorded with *full vertical binning*, i.e. a column of pixels on the CCD is treated as one single pixel.

takes a significant portion of the overall exposure time. As soon as the exposure time of the spectra frame deviates from that of the flat frame, the flat frame is no valid representation of the spectral distribution of the probe-IR in the spectra frame.

2. It is possible to record at a certain central probe-IR wavelength and acquire frames at different pump delays. Then we can change the central wavelength and scan the delay again. Switching the central wavelength less often may be beneficial for the stability of the probe-IR laser in terms of its spectrum and power. In this work, however, we changed through all central wavelengths first before changing the delay. So, this advantage is purely theoretical.

A disadvantage of the *frame-by-frame* approach is that we have an increased amount of readout noise compared to the *single frame* approach. However, this disadvantage only becomes relevant for low signal-to-noise ratios and does not apply to the spectra recorded in this work.

2.2.2 Processing Spectra

Subtracting Dark Frames

The first thing we do is averaging all dark frames D_i to a dark image $\bar{D}$ and subtracting that from each spectrum frame S'_m. The same is done for the dark flat frames D^*_j with its dark image $\bar{D}^*$ and the flat frames $S^{*\prime}_m$:

$$S_m = S'_m - \bar{D} \tag{2.11}$$

$$S^*_m = S^{*\prime}_m - \bar{D}^* \tag{2.12}$$

All D and S are pixel matrices representing the image from the CCD.

Combining the Frames

In the next step, we add up all the spectrum frames and flat frames to obtain a spectrum S and flat image S^* respectively. In case we encounter a non-resonant background, these are then normalized to the count values p and p^* of pixels that do not hold any spectral features.

$$S_{\text{sum}} = \frac{\sum_m S_m}{p} \tag{2.13}$$

$$S^*_{\text{sum}} = \frac{\sum_m S^*_m}{p^*} \tag{2.14}$$

The result of this processing step is shown in Figure 2.13 in the upper plot.

Flat Field Correction

After this, we divide the spectrum by the flat image. This promotes areas of the spectrum with low probe-IR intensity, and the baseline becomes relatively straight. The outcome is shown in the middle plot in Figure 2.13 as the red line.

$$S_{\text{flat}} = S_{\text{sum}}/S^*_{\text{sum}} \tag{2.15}$$

Baseline Correction

However, the baseline is still sloped upwards. A possible reason for this can be fluctuations in laser intensity. A second possibility is that the sum-frequency beam is not entering the

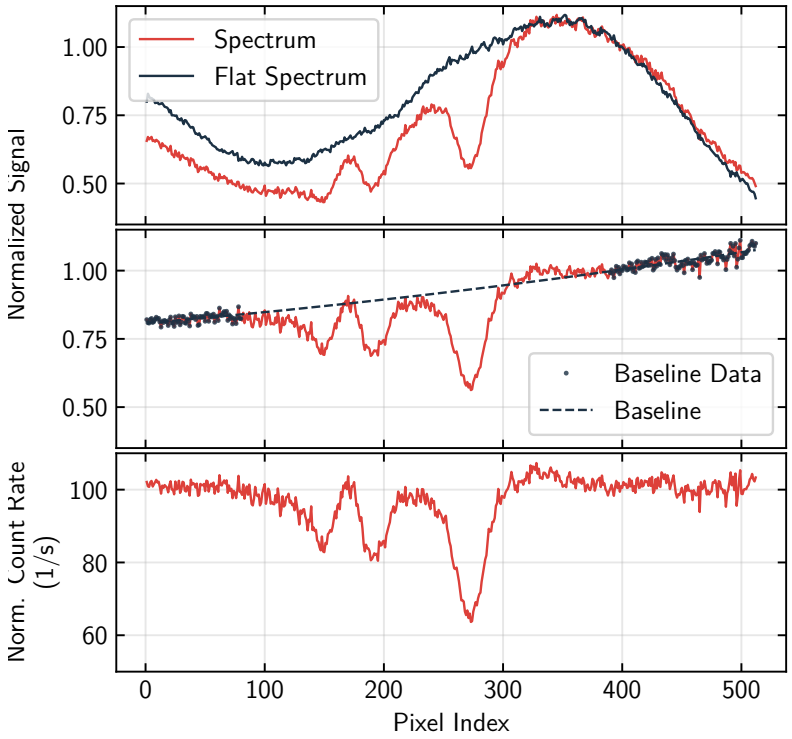

Figure 2.13: Illustration of further processing steps: Coming from Figure 2.12 spectrum frames and flat frames are combined (upper plot) and normalized the count value of the pixel with index 400. This yields the flat field corrected spectrum S_{flat} (middle plot) which is in turn baseline corrected and normalized to the total count rate, leading to the final result (lower plot).

spectrometer in the same way for both the spectrum frames and the flat frames. This can be caused by either a differing tilt angle or position of the sample and the flat frame reference. In any case, we can make a fit of this baseline and subtract it from the spectrum. For the fitting, we have to choose data points of the spectrum that should end up on the baseline after subtraction. We then fit these data points with a polynomial. Typically a second or third-order polynomial is sufficient. For spectra that do not have a non-resonant background, the baseline level β_0 is 0. For a spectrum with non-resonant background, β_0 has to be set to the value of the spectrum at normalization point p. Conveniently if we also normalize the spectrum, this value is 1. This normalization procedure ensures that the intensity ratio between the bands and the non-resonant background is not altered. The ratio is important because it contains meaningful information about the phase relation between the non-resonant background and the specific vibrations. In summary, we are subtracting the fitted baseline B from our spectrum S and add the baseline level β_0:

$$S_{\text{base}} = S_{\text{flat}} - B + \beta_0 \tag{2.16}$$

Count Rate Normalization

By dividing the spectrum by the flat image, we lost information about the count rate. However, the count rate can be useful to compare signal and noise between different spectra. We can recover this information by normalizing the integral of the spectrum S_x and multiplying by the count rate that is taken from the summed spectrum S_{sum}:

$$S_{\text{final}} = \frac{S_{\text{base}}}{\int S_{\text{base}}} \times \frac{\int S_{\text{sum}}}{\sum_m \tau_{\text{exp},m}} \tag{2.17}$$

Of course, this normalized count rate does not represent the count rate per pixel but rather an average count rate for the whole spectrum. In Figure 2.13 the overall count rate for the spectrum was around $50\,000\,\text{s}^{-1}$. This value is well represented by the normalized spectrum in the figure's lower plot.

Event Removal

High energetic particles might hit the sensor of the CCD camera. These particles cause a large number of electrons to be registered at the pixel (and sometimes also surrounding pixels) they hit. The source of these particles can be either cosmic rays originating from supernovae or pulsars [36] or are products of radioactive decay [37].

We can remove the majority of these events with the following algorithm:

1. Transform the N-dimensional data to a 1-dimensional array.
2. Compute the differences in counts between each subsequent pixel in the array.
3. For these count differences, set a threshold above which pixels are marked for potentially containing an event. The threshold is based on the standard deviation of the data.
4. Set a maximum pixel width of the events
5. Loop through every individual data point. Check if the difference in counts within a specific interval exceeds the chosen threshold in both positive and negative directions. The threshold value must first be exceeded in positive direction and then in negative direction.
6. Determine the width of the event.
7. Replace the data points belonging to the event with interpolated data.

A schematic representation of the event removing algorithm is shown in Figure 2.2.2. The algorithm itself can be found in Appendix 1.

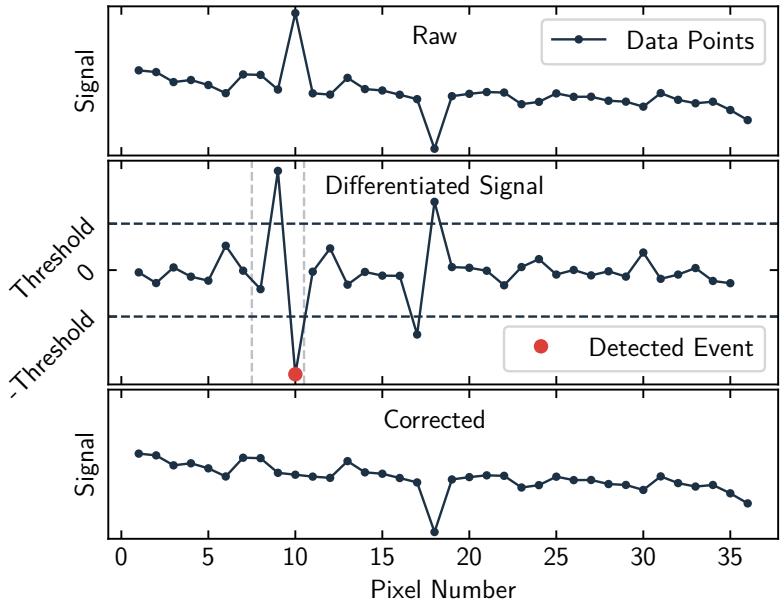

Figure 2.14: **Upper plot:** Exemplary raw data put in the event removal algorithm. **Middle plot:** Differentiated data with threshold at 1.5 times the standard deviation of the data. The maximum width of the events (indicated by the faint dashed lines) is, in this case, set to 2 pixels. **Bottom plot:** Cleaned data. The signal value of the detected event is replaced by the mean value of the data points just before and after the event.

2.2.3 Recording Pump-Probe Spectra

For the pump-probe experiments, we want to record a series of spectra where for each spectrum in the series, the probe pulse is at a different delay with respect to the pump pulses. Moreover, we do not go through the different delay positions in sequence but rather go through them randomly. The disadvantage is that the measurement will take longer since the delay stage often has to move long distances. The advantage, however, is that if parameters in the experiment like the ambient temperature, the pump energy change, or even if the sample degenerates, this change will not show up as a positive or negative trend in the processed signal data. It will rather show up as noise.

Every time the wavenumber of the pump laser changes during a measurement, its power is attenuated to a fixed value. In the case of our experiments, we kept the pump laser at a pulse energy of 35 μJ. To this end, the power of the pump laser is measured by PM3 (see Figure 2.2), and the measurement program attenuates the input energy to the *Ekspla: PG711 DFG* unit accordingly.

Other than that, the recording of the individual spectra is done as described in Chapter 2.2.1. The next step is to process these pump-probe spectra. We will take a look at that in the next section.

2.2.4 Processing Pump-Probe Spectra

For the pump-probe experiments, we have a series of recorded spectra. The processing for each spectrum in this series is the same as described in Section 2.2.2. In the case of our experiment, during long time measurements that take several hours, the power of the probe pulse decreases significantly. In addition to that, the center wavelength of the probe pulse often shifts. This can significantly alter the shape of the spectrum throughout the measurement. Thus, a big challenge in processing these spectra is that the last spectrum in the series still has to be comparable to the first in the series. For this reason, although we simultaneously record a reference to each spectrum, we have to reference all these reference spectra to a "master-reference". A good choice for the "master-reference" is to take the average of all reference spectra R_i that were recorded. This ensures a low signal-to-noise ratio for this master reference $\bar{R}$.

$$\bar{R} = \frac{1}{N} \sum_{i}^{N} R_i \tag{2.18}$$

Next, we divide all the reference spectra by the master reference. This way, for each pixel and spectrum we get a factor f_{R} with which we need to multiply the value of that pixel to get to the value of the master-reference.

$$f_{\mathrm{R},i} = R_i / \bar{R} \tag{2.19}$$

These per-pixel reference factors f_R do also apply to the signal spectra S_i. To correct the signal spectra, we have to multiply these with the factors we just obtained:

$$S_{i,\mathrm{corr}} = f_{\mathrm{R},i} \times S_i \tag{2.20}$$

The corrected spectra $S_{i,\mathrm{corr}}$ are now comparable to each other.

2.3 Calcium Arachidate Monolayers

In our experiments, we use calcium arachidate monolayers deposited on glass slides. Calcium arachidate monolayers – and more generally monolayers of saturated fatty acids – are a well-known system that is described in great detail in the literature [38–51]. This section gives an overview of the properties that are most relevant in the context of this thesis. In our group, the preparation of these monolayers is an established procedure [52, 53] so that the preparation technique will not be described in detail here. However, Section 2.3.3 has an overview of the used equipment and chemicals. We will also look at the IR and Raman spectra of arachidic acid in Section 2.3.4. This will help us interpret the sum-frequency spectra presented in Chapter 3.

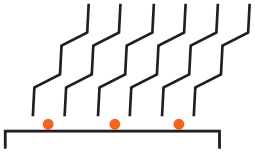

Figure 2.15: Schematic representation of a Langmuir-Blodgett monolayer of calcium arachidate. The arachidate molecules align themselves with each other and two at a time coordinate to one Ca^{2+} ion. The calcium ions are represented by the orange dots.

2.3.1 Properties

The system that we are probing in our experiment is a Langmuir-Blodgett (LB) monolayer of calcium arachidate deposited on glass. The arachidate ion ($C_{20}H_{39}O_2^-$) is mainly build up by a fully saturated alkyl chain with 18 methylene (CH_2) groups. The alkyl chain is terminated with a methyl group (CH_3) on one end and a carboxylate group (COO^-) on the other end. The carboxylate group coordinates to a Ca^{2+} ion (see Figure 2.16).

In the monolayer, the alkyl chains align themselves towards each other. This is shown schematically in Figure 2.15. Each calcium ion coordinates two carboxylate groups. Because of this coordination, the monolayer has overall increased stability compared to plain arachidic acid deposited on glass [54]. The tilt angle of the carbon chains relative to the surface for LB films of cadmium arachidate and calcium arachidate on a Si(111) surface

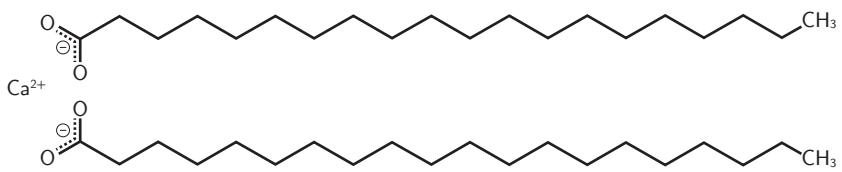

Figure 2.16: Skeletal structure of two arachidate molecules that are coordinated to one Ca^{2+} ion.

was found to be $0 \pm 15°$ and $33 \pm 5°$, respectively [40]. The experimentally found tilt angle for calcium arachidate is supported by molecular dynamics calculations [42]. With a C−C−C bond angle of 115° this translates to tilt angles of the CH_3 group of $33 \pm 15°$ for cadmium arachidate and $0 \pm 5°$ for calcium arachidate. These are just two examples of systems similar to the one in this work. These tilt angles are indicative of what we can expect for the tilt angles in our calcium arachidate/glass system.

2.3.2 Gauche-Defects

This section highlights gauche defects in alkyl chains and why they may be important for our experiment. The thermodynamically most favorable conformation for the alkyl chains in LB monolayers is the all-*trans* conformation. However, if we rotate one of the CH_2 groups on a C−C bond, we find two metastable conformations called gauche conformations. If a molecule in an LB monolayer forms one of these gauche conformations, the alkyl chain of this particular molecule will not be aligned with the alkyl chain of all the other molecules anymore. Therefore it is called a gauche defect. Gauche defects in calcium arachidate monolayers typically exist at room temperature [48]. Earlier work performed in our group shows that a significant amount of defects form at temperatures higher than 340 K [52, 55]

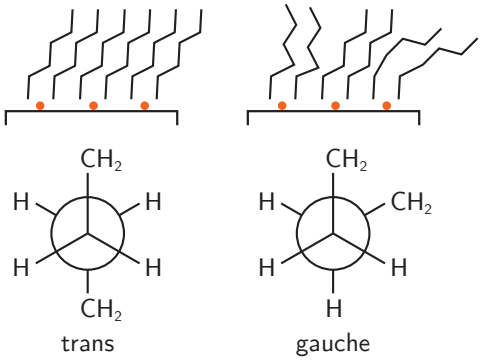

Figure 2.17: Illustration of the influence of gauche defects on the ordering of a LB-monolayer. On the left, all alkyl chains are in *trans* conformation resulting in a fully ordered monolayer. On the right some alkyl chains are in gauche conformation resulting in a disordered monolayer.

Gauche defects are relevant to our experiment because they influence the intensity of the sum frequency signal we obtain from the calcium arachidate monolayer. Thereby, three factors influence the SF intensity. Firstly, due to the change in conformation, the tilt angle of the alkyl chain changes. The tilt angle influences the susceptibility of the CH_3 mode, which directly impacts the SF intensity as we saw in Section 2.1.1. Secondly, the defects cause structural disorder in the calcium arachidate monolayer, effectively lowering its symmetry. Since vSFS is sensitive to the symmetry of the probed medium, this

generally leads to a reduction in signal intensity. The third aspect is that by breaking the symmetry of the alkyl chains, vibrational modes of the CH_2 groups become visible in the sum frequency spectrum [52, 53, 56]. In our experiment, by inducing energy into the calcium arachidate monolayer, we will inevitably heat it. This may increase the number of gauche defects and cause a disordering. The disordering could cause an intensity reduction for the observed CH_3 stretching vibrations, while the CH_2 stretching vibrations will increase their intensity in the SF spectra.

2.3.3 Sample Preparation

The preparation method is well established and was described in full detail before [52, 53, 55, 57]. This section gives a brief overview of the equipment and the chemicals used for the sample preparation.

The calcium arachidate monolayer was deposited on the glass slides ($1 \times 1\,\mathrm{cm}^2$, 0.5 mm thickness, *Plano GmbH* microscope coverslips) using the Langmuir-Blodgett technique. A 5 mM solution of $CaCl_2$ in deionized water (resistivity $\sim$18 MΩ cm) was used as a subphase. The pH of that subphase was adjusted with a saturated solution of $Ca(OH)_2$ to a value of 9.5. For spreading the arachidic acid (*Sigma Aldrich*; analytical grade) onto the subphase, 70 µL of a 1 mM solution in chloroform was used. The surface pressure during the transfer of the arachidate onto the glass slides was 32 mN/m. This transfer pressure ensures that the arachidate was in the highly ordered superliquid phase during transfer [58]. The molecule density on the subphase at this pH value is around $5.2\,\mathrm{nm}^{-2}$ [44].

2.3.4 Spectra

IR and Raman Spectra

Figure 2.18 shows the IR and Raman spectra of crystalline arachidic acid in the CH stretch region. In the IR spectrum, the most prominent features are the d^+ and d^- modes at $2852\,\mathrm{cm}^{-1}$ and $2921\,\mathrm{cm}^{-1}$ respectively. The smaller features can be assigned to the r^+ mode at $2878\,\mathrm{cm}^{-1}$ and the in-plane and out-of-plane r^- modes at $2959\,\mathrm{cm}^{-1}$ and $2966\,\mathrm{cm}^{-1}$. The shoulder on the blue side of the d^- band is the overtone of the CH_3 asymmetric bending mode that is in Fermi resonance with the r^+ mode. Hence, it is labelled r^+_{fr}.

The Raman spectrum differs from the IR spectrum in several ways. The most prominent feature in the Raman spectrum is the r^+ mode that is comparably weak in the IR spectrum. The d^- mode, on the other hand, is relatively weak in the Raman spectrum. Also, only one of the two r^- shows up at $2961\,\mathrm{cm}^{-1}$. The Raman spectrum shows two d^+ modes at $2842\,\mathrm{cm}^{-1}$ and $2852\,\mathrm{cm}^{-1}$ with an intensity ratio of 3 : 2.

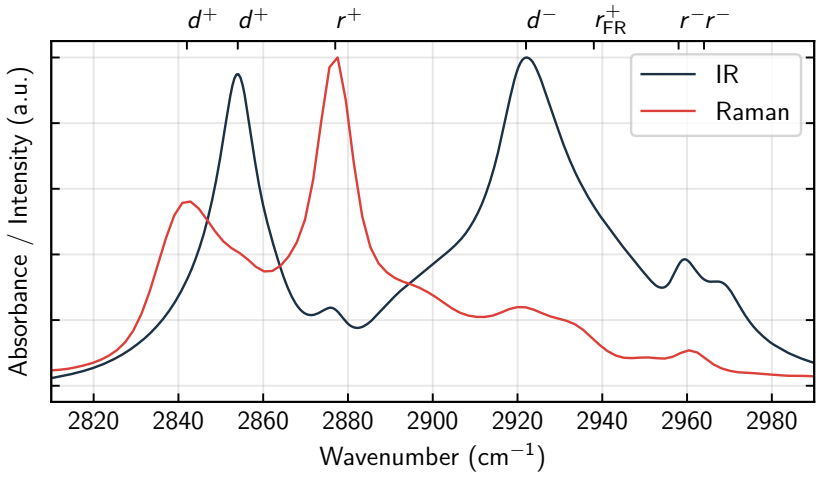

Figure 2.18: Normalized IR (black) and Raman (red) spectra of bulk arachidic acid in the CH stretch region. The y-axis shows the absorbance for the IR spectrum and the intensity for the Raman spectrum in arbitrary units.

Sum Frequency Spectrum

Here we will briefly discuss the main features of the sum frequency spectra of calcium arachidate. A detailed discussion on how to interpret the SF spectra will follow in Section 3. For the assignment of the resonant features of the spectrum to specific vibrational modes, we can rely on previous work. For this, we do not solely rely on our specific system – calcium arachidate on glass slides – but we can also refer to assignments that were suggested for similar systems of long, CH_3 terminated alkyl chains.

Sum frequency spectra of calcium arachidate were recorded in both *ssp* and *ppp* polarization combinations. These polarization combinations should provide us with the complete set of resonances that can be revealed by SF spectroscopy. The *sps* and *pss* polarization combinations were omitted because they do not give us information that is relevant in the context of this thesis. In essence, they show the same vibrational modes as in *ssp* and *ppp* polarization but with an overall lower intensity. This can be shown from the analysis of the respective tensor elements [33].

Sum-frequency spectra of calcium arachidate are shown in Figure 2.19. In the *ssp* and *ppp* polarization combinations, different modes are visible. At 2850 cm^{-1} the symmetric stretch (d^+) of the CH_2 groups is visible in the *ssp* polarization combination. The CH_3 symmetric stretch (r^+) as well as its Fermi resonance (r^+_{fr}) and its asymmetric stretching vibration are visible in both *ssp* and *ppp* spectra at 2879 cm, 2942 cm, and 2962 cm^{-1}, respectively. In the *ssp* spectrum, the r^- mode shows up only as a shoulder on the blue side of the r^+_{fr} mode. In the *ppp* spectrum, the r^+_{fr} mode is visible as a shoulder on the red side of the r^- mode. Another feature that can be seen in the *ppp* but not the *ssp* spectrum is a weak resonance at 2900 cm^{-1}. This feature may be attributed to the

Table 2.4: Wavenumbers of modes in sum-frequency spectra of adsorbate systems comparable to calcium arachidate monolayers on glass. For comparison, the table also lists the wavenumbers for IR and Raman spectra of crystalline arachidic acid. The latter two were recorded for this work. The molecules are octadecylsiloxane (ODS), docosanethiol (DT), palmitic acid (PA), and arachidic acid (AA). Adapted and extended from Ref. [59]

Reference	[59]	[60]	[61]	[62]	[62]		
Molecule	ODS	ODS	DT	PA	PA	AA	AA
Substrate	glass	silica	gold				
Method	vSFS	vSFS	vSFS	IR	Raman	IR	Raman
Mode							
r^+	2877	2873	2880	2871	2871	2878	2878
r^+_{fr}	2938	2935	2940	2938	2938	2936	2932
r^+_{fr}	2944						
r^-		2958					2961
r^-_b	2958		2954	2953	2955	2959	
r^-_a	2964		2968	2961	2964.5	2966	
d^+		2847	2855	2847.5	2846	2852	2842
d^+_ω	2862	2853	2864		2851		2852
d^-_ω	2885	2883				2894	2894
d^-_ω	2905						
d^-			2916	2916.5		2921	2921
d^-					2879.5		

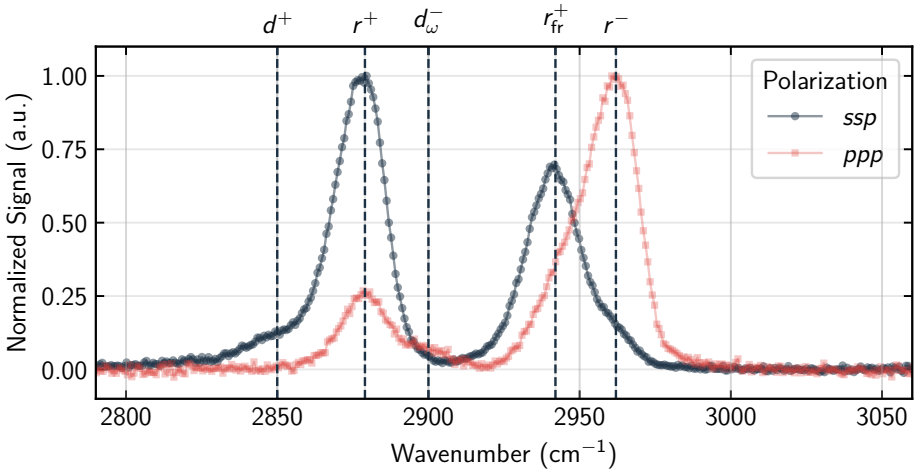

Figure 2.19: Sum frequency spectra of a calcium arachidate monolayer in *ssp* (black) and *ppp* (red) polarizations. Visible modes are indicated by dashed lines.

Table 2.5: Modes that are visible in a typical sum-frequency spectrum in our setup. The resonance positions are taken from Figure 2.19.

		visible	
Mode	ω (cm^{-1})	*ssp*	*ppp*
d^+	2850	✓	
r^+	2879	✓	✓
d^-_ω	2900		✓
r^+_{fr}	2942	✓	✓
r^-	2962	✓	✓

asymmetric stretching vibration of the methylene groups located at the end of the carbon chain of the arachidic acid (d^-_ω) [59]. Table 2.5 gives an overview of the resonances that are visible to the naked eye in the calcium arachidate sum-frequency spectra.

In Section 3 we will see that this is an overly simplistic description of the sum frequency spectra. Fitting the spectra will reveal additional resonances that are not immediately apparent when looking at the sum frequency signal in Figure 2.19. We will then refer to Table 2.4 for additional assignments of resonant features.

3 Results and Discussion

In this chapter, we present the results of the 2-color pump-probe experiment that we outlined in the previous chapter. Essentially, these are two experiments that build upon each other. The first experiment is going to determine which modes of the arachidate molecule are worth pumping. In the second experiment, we are going to investigate the vibrational dynamics of the arachidate molecule. For this purpose, we are going to pump those modes we found worthy in the first experiment. In the final step, we are going to develop a model to be able to account for the results.

3.1 Resonant Pump-Probe Effects

Ultimately we are interested in the vibrational dynamics of the calcium arachidate molecule as part of the adsorbate system. However, to figure out these dynamics, we first have to evaluate how we can put energy into the system to move it out of equilibrium. The aim is to insert the energy selectively into a particular vibrational mode of the adsorbed arachidate molecules.

3.1.1 Experiment Description

To figure out which vibrational modes are most suitable for this task, we set up an experiment where we sequentially change the energy of the pump-IR pulse. Then, for each pump energy, we record the spectrum. This lets us determine which pump energies have the strongest effect on the sum-frequency spectrum. To set this up, we tuned the delay between pump and probe so that the sum-frequency spectrum was affected the most.

Figure 3.1 shows the results of this experiment. The difference spectra are calculated by subtracting the signal of the non-pumped spectrum (ref) from the signal of the pumped spectrum:

$$\Delta I_{\mathrm{SF}} = I_{\mathrm{SF,pumped}} - I_{\mathrm{SF,ref}} \tag{3.1}$$

and displayed as a heatmap in Figure 3.1. Each row in the heatmap represents a spectrum with the pump laser fixed at the respective wavenumber. For a better orientation, the sum-frequency spectrum in the respective polarization combination is displayed above

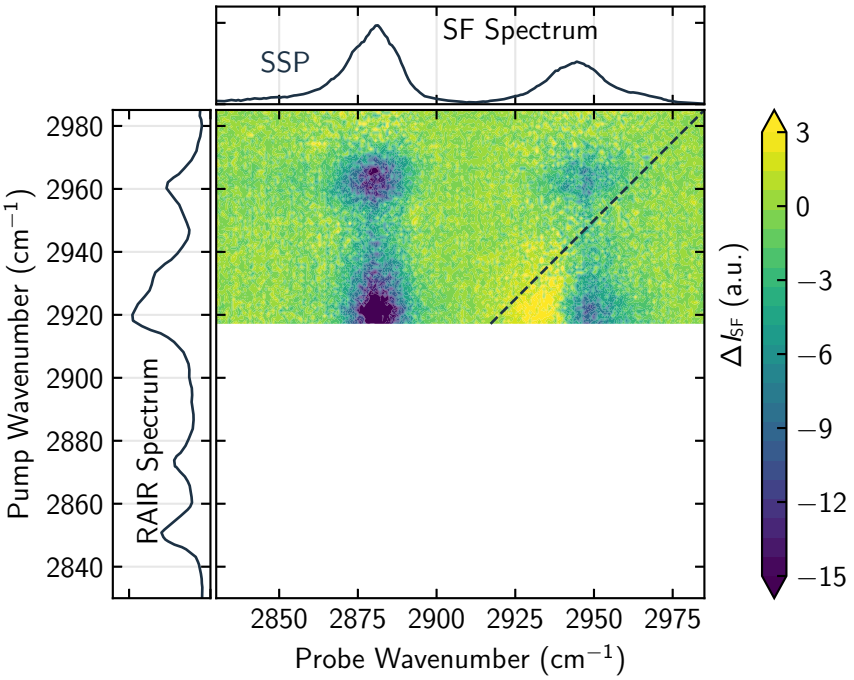

Figure 3.1: Two-dimensional difference-spectrum in *ssp* polarization showing the relation between pumped wavenumber and signal decrease in the spectrum. The top plot shows the unpumped sum-frequency spectrum in *ssp* polarization. The plot on the left shows the RAIR spectrum, indicating the absorption of the pump-IR for different wavenumbers. The dashed line marks where the wavenumber in the difference-spectrum is equal to the wavenumber of the pump pulse.

the difference spectrum. On the left, the reflective-absorption infrared (RAIR) spectrum of arachidic acid on gold is shown. The RAIR spectrum indicates the amount of energy absorbed by the calcium arachidate molecules. With this data, we have a way to determine which pump energies have the largest effect on the sum-frequency spectrum.

3.1.2 Data Description

In Figure 3.1 we can see two strong features in each dimension. In the probe wavenumber dimension, we observe the strongest differences in signal for wavenumbers of 2880 cm^{-1} and 2940 cm^{-1}. This is not surprising since these are the energies where the sum-frequency spectrum shows the most prominent features. We can assign these two features to the r^+ and the r_{fr}^+ modes, respectively. Other modes in the sum-frequency spectrum are not strong enough to show an immediately apparent decrease in signal intensity. In the pump wavenumber dimension the features in the difference-spectrum in Figure 3.1 show up at 2922 cm^{-1} and 2960 cm^{-1}. These two modes correspond to the most prominent features

in the RAIR spectrum in the spectral range of the pump pulse (see Figure 3.1). These energies correspond to the d^- and r^- modes, respectively. For the r^+ mode, the signal decrease when pumping the d^- mode is about 1.5 times as large as when pumping the r^- mode. I.e., the wavenumbers at which the most molecules get excited by the pump laser.

If we look at the *ssp* difference-spectrum in Figure 3.1 more closely, we can observe an increase in signal intensity on the red flank of the r^+_{fr} band when pumping the d^- mode. Two possibilities come to mind how this could be possible:

1. The center wavenumber of the r^+_{fr} mode may shift to higher energies upon exciting asymmetric CH_2 stretch (d^-).

2. The signal increase is caused by a convolution of r^+_{fr} with another resonance. The possibility that this might be the case is demonstrated in Figure 3.2. The spectral profiles I_{SF} and signal differences ΔI_{SF} in this figure were calculated by

$$I_{\mathrm{SF}} = \left| \sum_q \frac{a_q A_q}{\omega_q - \omega + i\Gamma_q} \right|^2 \tag{3.2}$$

and

$$\Delta I_{\mathrm{SF}} = \left| \sum_q \frac{a_q A_q}{\omega_i - \omega + i\Gamma_q} \right|^2 - \left| \sum_q \frac{A_q}{\omega_q - \omega + i\Gamma_q} \right|^2 . \tag{3.3}$$

The parameters that were used for the calculation are listed in the figure caption. The parameters of the first resonance loosely resemble values that we can expect for the r^+_{fr} of a calcium arachidate monolayer (see Table 2.4). The second resonance is hypothetical. It is important to note here that the two resonances must be energetically close to each other and exhibit opposite phase. The latter would indeed be the case for the r^+_{fr} and the r^- modes. The phase of these two modes was resolved by Shen and coworkers [60] using phase-sensitive sum-frequency spectroscopy in octadecyltrichlorosilane monolayers. However, the r^+_{fr} and r^- modes are $\sim$20 cm^{-1} apart whereas in this example the spectral distance is only 10 cm^{-1}. It is therefore unlikely that the signal increase is caused by a convolution between the r^+_{fr} and r^- modes but may be attributed to a yet unrevealed mode.

3.1.3 Correlation between Energy Input and Signal Difference

Let us take a closer look at the correlation between energy input and effect on the r^+ band. Figure 3.3 shows the RAIR spectrum of arachidic acid on gold alongside the signal difference of the r^+ mode in the sum-frequency spectrum. As a premise, we can assume that the strength of the bands in the RAIR spectrum is a proxy for the amount of energy

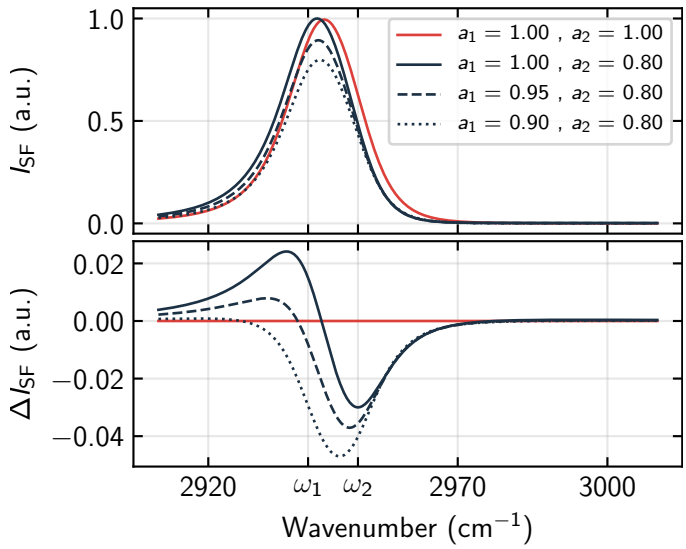

Figure 3.2: Calculated curve shapes (upper plot) and signal differences (bottom plot) of two convoluted vibrational modes in a sum-frequency spectrum. This shows the possibility of an increase in signal, even though the population in both modes decreases. Parameters that were used for the calculation of the line shapes are $A_1 = 6$, $A_2 = -5$, $\omega_1 = 2940\,\mathrm{cm}^{-1}$, $\omega_2 = 2950\,\mathrm{cm}^{-1}$, $\Gamma_1 = 10\,\mathrm{cm}^{-1}$ and $\Gamma_2 = 10\,\mathrm{cm}^{-1}$. The attenuation parameters a_i are shown in the legend.

the pump pulse induces into the system. Note that in our experiment, we are using glass as a substrate instead of gold. Therefore, the correlation between energy input into our system and absorption strength in the RAIR spectrum shown here will not be exact. However, the general correlation should be similar. On the one hand the signal difference and the IR absorption are correlated almost 1 : 1 for the d^- and r^- modes (here at around $2920\,\mathrm{cm}^{-1}$ and $2960\,\mathrm{cm}^{-1}$ respectively). On the other hand, the difference in signal when pumping the r_{fr}^{+} mode (which is showing up as a shoulder on the blue side of the r^- absorption band at around $2935\,\mathrm{cm}^{-1}$) is insignificant. Let us keep this finding in mind as we will elucidate why this is the case at a later point in time.

It is worthy to note that we could not pump modes lower in energy than $2917\,\mathrm{cm}^{-1}$. This is because, at this wavenumber, the pump laser switches from the idler to the DFG regime. This change requires a realignment of the pump and probe beams in both space and time so that a continuous measurement was not possible. A discontinuous measurement was not performed at the time of writing this thesis.

3.1.4 Summary

What can we learn from this experiment? The most obvious thing is that if we want to observe the vibrational dynamics of the system, we should primarily pump the d^- and r^- modes. We will take a look at the transients of the signal when pumping the d^- versus the r^- mode closely in Section 3.3 and even more closely in Section 3.4. We do not expect a

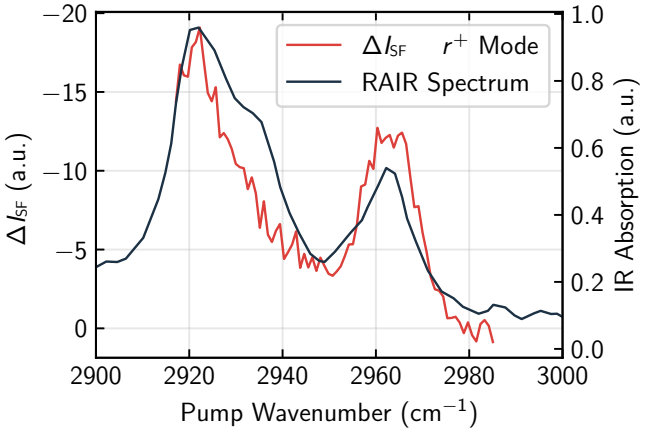

Figure 3.3: Comparison between the signal difference of the r^+ mode (red line / left y-axis) and IR absorption in the RAIR spectrum (black line / right y-axis). The data in the red plot was calculated by taking an average of the signal difference of the r^+ mode in the difference-spectrum (Figure 3.1) over a range of $20\,\mathrm{cm}^{-1}$.

strong effect on the prominent resonances in the sum-frequency spectrum when pumping the r^+_{fr} mode. However, according to the RAIR spectrum, the system absorbs energy at this frequency. Why do we not observe a signal change of the r^+ or r^- modes then? We will address this issue in Section 4.1. Lastly, as we can see from the data in Figure 3.2, the description of the transients becomes complicated when we are dealing with modes that are close in energy and have opposite phase. In order to describe the transients of these modes, a thorough mathematical description of the spectral data is necessary. This means that we have to fit the spectra, which we will do in the following section.

3.2 Fitting the SF Spectra

In order to be able to analyze the SF spectra quantitatively, we need to fit our data. This is especially the case if we want to decipher the transient signal of convoluted modes. For example, as we could see in the previous section, this is the case with the r_{fr}^{+} mode. Here, the convolution possibly causes an increased signal in the pumped spectrum even though the oscillator strengths do not increase. Before we take a look at the transient signal, we will fit the spectra.

3.2.1 Data Sets for Fitting

In our case, as we can see in Figure 3.4, there are four different datasets that we have to fit. These four data sets are the r^{-}-pumped and d^{-}-pumped spectra, both in *ssp* and *ppp* polarization.

ssp	*ssp*
d^{-}	r^{-}
ppp	*ppp*
d^{-}	r^{-}

The data were not taken from Figure 3.1 but from the experiments described in Section 3.3. In order to increase the signal-to-noise ratio of the pumped spectra, we took the mean value of those spectra that show a pronounced change in signal. Specifically, these are the spectra with pump delays of $t_0 - 5\,\mathrm{ps}$ to $t_0 + 15\,\mathrm{ps}$ where t_0 is the delay time at which the r^{+} mode shows the strongest signal decrease. An exception is the d^{-}-pumped *ppp* spectrum. Here, the upper bound is $t_0 + 40\,\mathrm{ps}$ to increase the signal-to-noise ratio.

3.2.2 Fit Model

We can express the intensity of the recorded SF spectra as a sum of Lorentzians (see Section 1.1.5):

$$I_{\mathrm{SF}} = \left| \chi_{\mathrm{NR}}^{(2)} + \sum_{q} \frac{A_q}{\omega_q - \omega + i\Gamma_q} \cdot e^{-i\varphi_q} \right|^2 \tag{3.4}$$

Since the glass substrate does not show a non-resonant background $\chi_{\mathrm{NR}}^{(2)} = 0$. Also, for calcium arachidate, we expect the relative phase of the resonances to be either $\pm\pi$ or 0 so that $e^{-i\varphi_q} = -1 + 0i$ or $1 + 0i$, respectively. We can model these phase relations by letting A_q take on either negative or positive values. In our case, in addition to the plain spectra (black plots in Figure 3.4), the difference spectra contain information that can help us to fit the spectra more accurately, provided we have a good mathematical description of how

the SF spectrum changes under the influence of the pump pulse. In order to describe this mathematically, we extend the model in Equation 3.4. Several possibilities come to mind how we can describe the effect of the pump pulse on the system:

1. The sum-frequency line strength changes. The line strength is, among other things, a measure of how many available oscillators there are. If we pump the system and thereby excite molecules to their vibrationally excited states, these vibrationally excited molecules will not contribute to the sum-frequency signal. In order to describe this, we can introduce an attenuation coefficient a_q which, like the name suggests, attenuates the line strength in the pumped spectrum:

$$I_{\mathrm{SF,pumped}} = \left| \sum_q \frac{a_q A_q}{\omega_q - \omega + i\Gamma_q} \right|^2 \tag{3.5}$$

   In this case, we can express the difference spectrum by

$$\Delta I_{\mathrm{SF}} = \left| \sum_q \frac{a_q A_q}{\omega_q - \omega + i\Gamma_q} \right|^2 - \left| \sum_q \frac{A_q}{\omega_q - \omega + i\Gamma_q} \right|^2 . \tag{3.6}$$

2. A shift of the resonance frequency may occur. If a mode in a molecule is vibrationally excited, this can cause other vibrational modes to shift their frequency due to anharmonic coupling. Mathematically this is not as straightforward to implement as the change in oscillator strength. In theory, we now have to consider that for each excited vibrational mode p the frequency ω_q of an observed resonance q may shift. This can be expressed by

$$\Delta I_{\mathrm{SF}} = \left| \sum_q \sum_p \frac{a_{q,p} A_q}{\omega_{q,p} - \omega + i\Gamma_q} \right|^2 - \left| \sum_q \frac{A_q}{\omega_q - \omega + i\Gamma_q} \right|^2 , \tag{3.7}$$

   where for a given resonance q the sum of attenuation factors $\sum_p a_{q,p} = 1$.

3. The damping coefficient may change. Mathematically this is similar to the previous point, except here, we would have to iterate through all $\Gamma_{q,p}$ instead of $\omega_{q,p}$.

Of course, there is also the possibility that we have a combination of these three phenomena. In order to simplify things for our fitting procedure, we will only consider the first model where the oscillator strengths change.

As mentioned previously, we have four datasets that we want to fit. The resonance frequencies ω_q and the damping constants Γ_q should not change across these data sets since they depend neither on the polarization combination nor on the pumped mode. We can take advantage of that by not fitting each dataset independently but rather make one

optimization taking all datasets into account. The loss function to optimize is then

$$\text{loss} = \int \left| \sum_i \sum_j I'_{\text{SF}} - \left| \sum_q \frac{A_{q,i,j}}{\omega_q + \Delta\omega_{i,j} - \omega + i\Gamma_q} \right|^2 \right|^2 \mathrm{d}\omega + \int \left| \sum_i \sum_j I^{*\prime}_{\text{SF}} - \left| \sum_q \frac{A^*_{q,i,j}}{\omega_q + \Delta\omega_{i,j} - \omega + i\Gamma_q} \right|^2 \right|^2 \mathrm{d}\omega \,, \tag{3.8}$$

where the index i denotes the polarization combination $i = \{ssp, ppp\}$ and the index j denotes the pumped mode $j = \{d^-, r^-\}$. I'_{SF} and $I^{*\prime}_{\text{SF}}$ are the experimental intensity data for the plain and the pumped spectra, respectively. $A^*_{q,i,j}$ is the oscillator strength of the pumped spectrum. The attenuation parameter can then be calculated as $a_{q,i,j} = A^*_{q,i,j}/A_{q,i,j}$. So the only parameter that is allowed to change between the datasets is the oscillator strength A. Each dataset also has an offset frequency $\Delta\omega$. This accounts for the fact that the calibrated frequencies of the individual datasets do not match exactly. For example all resonance frequencies of the r^--pumped *ssp* spectrum could be blue-shifted by $1\,\text{cm}^{-1}$ in comparison to the d^--pumped *ppp* spectrum.

3.2.3 Fit Results

Table 3.1: Fit parameters for the *ppp* and *ssp* spectra.

q	ω_q	Γ_q	$A_{q,ssp}$	a_{q,ssp,d^-}	a_{q,ssp,r^-}	$A_{q,ppp}$	a_{q,ppp,d^-}	a_{q,ppp,r^-}
d^+	2845	5.1	0.2	1.03	0.97	0.2	0.84	0.90
r^+	2876	9.6	10.8	0.94	0.96	6.0	0.94	0.97
d^-_ω	2887	7.3	−4.2	0.87	0.94	−1.4	0.79	0.90
d^-_ω	2906	12.5	−3.5	0.97	0.98	−3.2	0.96	0.99
r^+_{fr}	2938	11.8	11.5	0.99	0.98	6.0	1.04	1.00
μ	2949	11.2	−6.8	0.89	0.94	−0.4	5.08	0.95
r^-_b	2960	6.2	−0.9	0.81	0.95	−3.7	0.97	1.01
r^-_a	2966	5.2	−1.0	1.09	1.08	−3.4	0.82	0.94

By applying the previously discussed model to the data, we get the fits in Figure 3.4 with the parameters listed in Table 3.1. Fitting the data shows that we have to take into account at least eight resonances. The most prominent vibrational mode in the *ssp* spectrum is the r^+ mode alongside its Fermi resonance r^+_{fr}. As expected, the oscillator strengths of these two modes are comparable in both *ssp* and *ppp* polarization. In *ppp* polarization, the most prominent vibrational mode is r^- if we sum up the in-plane and out-of-plane vibrations r^-_a and r^-_b. As expected from theory, the phase shift of these modes with respect to the r^+ mode is $\pm\pi$. Surprisingly, we are able to distinguish between the r^-_a and the r^-_b mode. An indication that we resolved this correctly is that both modes

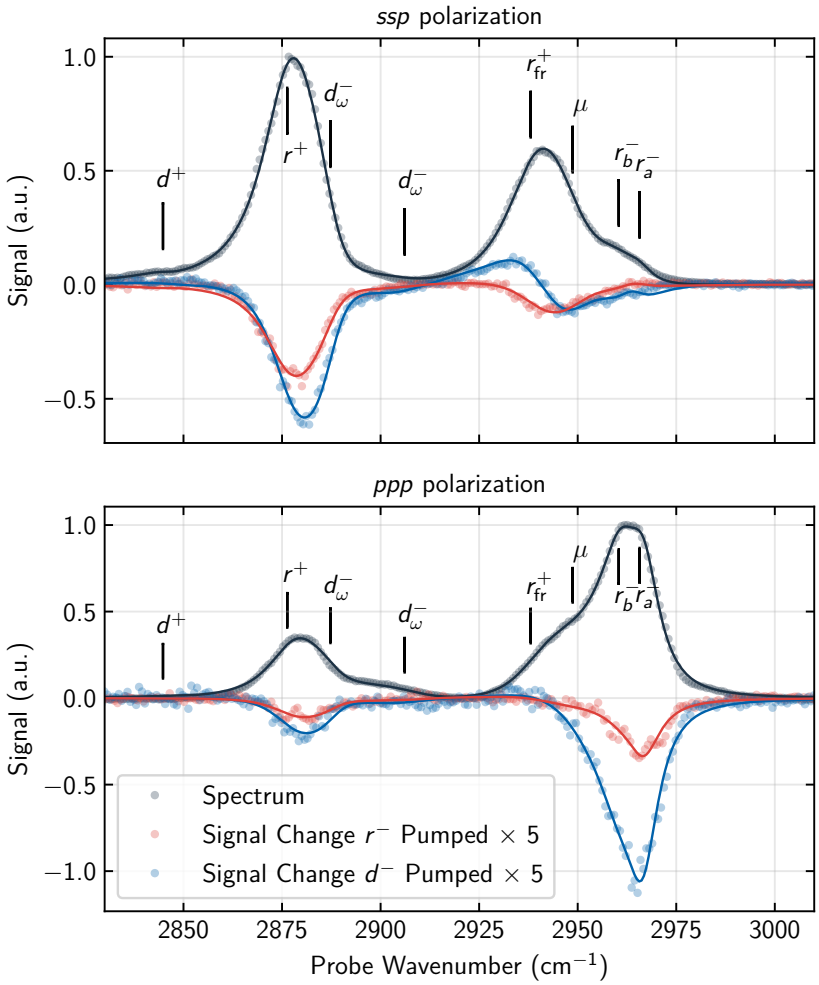

Figure 3.4: Calcium arachidate spectra in *ssp* (top) and *ppp* polarization (bottom) alongside scaled difference spectra for the r^--pumped case (red) and the d^--pumped case (blue). The data were taken from the experiments in Section 3.3. The solid lines are fits to the data.

have comparable oscillator strengths since, in theory, the susceptibility of the in-plane and out-of-plane modes is identical (see Section 2.1.1). The d^+ mode is weak in both *ssp* and *ppp* polarization, indicating that the calcium arachidate is assembled in a well-ordered monolayer. This is also the reason the d^- mode does not show up in any of the two polarization combinations. However, we see two d^-_ω modes corresponding to the asymmetric stretching vibration of the CH_2 groups located at the ends of the alkyl chain. These are in-phase with the r^- modes. Then we have the resonance at $2949\,\mathrm{cm}^{-1}$ which is labeled μ. This one can not be assigned to any known vibrational mode. It is in-phase with the r^- modes and has a relatively strong oscillator strength in *ssp* polarization. However, it is weak in *ppp* polarization. Nonetheless, this vibrational mode is crucial to describe the data in the *ssp* spectra appropriately. Firstly, it is necessary to reproduce the marked shoulder on the blue side of the r^+_{fr} mode. Secondly, we need it to account for the signal increase on the red side of the r^+_{fr} mode in the d^--pumped difference spectrum.

Theoretical Intensity Ratio

The authors of references [63] and [29] discuss how to calculate the theoretically expected intensity ratio of the r^+_{fr} and r^+ modes. The r^+ mode is in Fermi resonance with the overtone of the asymmetric out-of-plane bend of the CH_3 group. For hexadecanoic acid, this bending mode is located at $1454\,\mathrm{cm}^{-1}$ [62]. We do not expect a significant deviation for the position of this mode for arachidate. Therefore, we would expect to find the overtone of the bend without a shift at approximately $\omega_0 \approx 2 \times 1454\,\mathrm{cm}^{-1} = 2908\,\mathrm{cm}^{-1}$. From Table 3.1, we obtain the actual positions of r^+ and r^+_{fr}. These are $\omega_{r^+} = 2878\,\mathrm{cm}^{-1}$ and $\omega_{r^+_{\mathrm{fr}}} = 2938\,\mathrm{cm}^{-1}$. With this information, we can evaluate the mixing coefficient b^2 to

$$b^2 = \frac{\omega_0 - \omega_{r^+_{\mathrm{fr}}}}{\omega_{r^+} - \omega_{r^+_{\mathrm{fr}}}} \approx 0.48 \tag{3.9}$$

With the property $a^2 + b^2 = 1$ and the relation of the mixing coefficients with the intensity ratio $I_{r^+_{\mathrm{fr}}}/I_{r^+} = A^2_{r^+_{\mathrm{fr}}}/A^2_{r^+} = R = b^2/a^2$, we get a theoretical intensity ratio of $R = 0.93$. If we consider the anharmonicity of the bending mode, the position ω_0 of the overtone will be shifted to lower wavenumbers. Even a slight shift of $14\,\mathrm{cm}^{-1}$ yields an implausible theoretical intensity ratio of $R \approx 2.6$. Therefore the values calculated here should be treated with caution.

The fitted intensity ratios are $R_{ssp} = 1.5$ and $R_{ppp} = 1.0$. The fitted ratio in *ssp* polarization is much higher than we expect from theory, while the ratio in *ppp* polarization is still reasonable. The discrepancy in *ssp* polarization could indicate two things. We either overestimated the intensity of the r^+_{fr} or underestimated the intensity of the r^+ mode. In the future, we could try to take the theoretical intensity ratio into account when fitting

the spectra.

3.2.4 Summary

With this, we have a good quantitative description of our SF spectra that can serve as a basis to perform the fitting of the transient signal. In the next section, we will take a first look at the time-dependent signals.

3.3 Transients

In the last section, we took a look at the "static" sum-frequency signal of a calcium arachidate monolayer. In this section, we take a first glance at the transients of the pumped spectra.

3.3.1 A First Look at the Transients

The results are displayed in Figure 3.5. Here, the signal difference is shown whereby the spectra were normalized so that the highest signal value corresponds to a value of 1. What can we learn from looking at the data? For the *ssp* spectra, we see the largest change in signal around the r^+ and r^+_{fr} modes. For the *ppp* spectra, the most substantial change in signal occurs around the r^- mode, followed by the $r+$ mode. This is expected since these are the major resonances observed in the respective polarization combinations, and the heatmap displays the absolute change in signal. In both *ssp* data sets, we observe an increase in signal for pump delays $> 25\,\mathrm{ps}$ around the d^+ mode. We do not observe this in the *ppp* difference spectra because here the d^+ mode does not show significant intensity. We can also observe a minor increase in signal on the blue side of the r^- mode for the same pump delays. What could cause this signal increase of the d^+ mode at pump delays $> 25\,\mathrm{ps}$? If the energy gets redistributed from the pumped modes into the low-energy torsion and bending modes of the alkyl chain of the arachidate, this could cause the chain to undergo so-called gauche defects, i.e., the alkyl chain kinks (see Section 2.3.2). This may cause a local breakdown of the isotropy of the CH_2 groups of the alkyl chain, causing their second-order susceptibility to be non-zero. We already saw the increase in signal on the red side of the r^+_{fr} in Figure 3.4 in the previous section. We explained the increase in signal with the convolution of the resonances in the spectral region of the CH_3 Fermi resonance. In the data in Figure 3.5 there may be an indication that this is also happening in the d^--pumped *ppp* spectra. However, the data are too noisy to determine this definitively.

What differences are there between the d^- and r^--pumped spectra? To answer this, we concentrate on the r^+ mode in the *ssp* spectra. In the d^--pumped case, we see a comparably slow recovery of the signal compared to the r^--pumped case. At a closer look, this is also the case for the *ppp* spectra, although the signal-to-noise ratio is significantly lower here. The r^- mode in the *ppp* spectra shows similar behavior to the r^+ mode. However, this is not obvious from the plots in Figure 3.5. For a better comparison, we plot the integrated signal intensity of these modes of interest in Figure 3.6. Note that we do not plot such data for the r^+_{fr} and any of the d^-_ω modes since these are heavily convoluted with their neighboring resonances. Therefore, their integrated signal would not just represent these resonances themselves but also their neighboring resonances. The same is true for the r^- modes in *ssp* polarization. What we end up with are therefore the

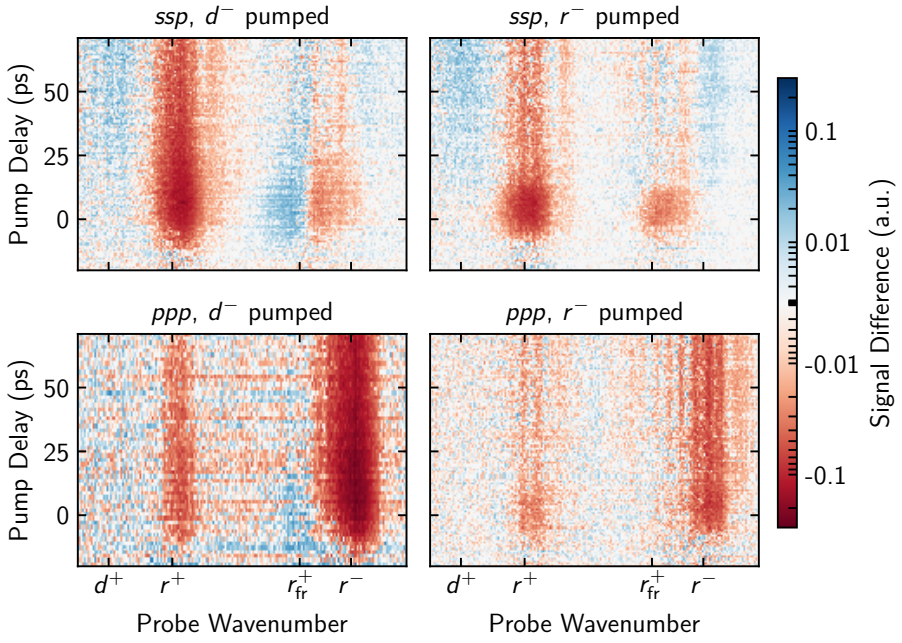

Figure 3.5: Transient difference spectra for all four datasets. The polarization combination, as well as the pumped mode, are indicated above the respective plot. The signal difference is scaled logarithmically to emphasize the slight increases in signal. On the wavenumber axis, the most prominent resonances are indicated.

d^+ mode from the *ssp* spectra, the r^+ mode from both the *ssp* and *ppp* spectra and the r^- modes from the *ppp* spectra. For these modes, it seems we can regard the integrated signal as representative of the temporal evolution of the signal. As we will see later on, this may not apply to the r^- mode, as the fitted line strengths are inconclusive (see Section 3.3.3).

How can we describe these "delay slices"? First we concentrate on the r^+ mode in both *ssp* and *ppp* polarization (the red and yellow plots in Figure 3.6). From here, one can clearly see that in the d^--pumped case, the signal of the r^+ mode recovers on a time scale of $\approx 100\,\text{ps}$. In the r^--pumped case, we see a rapid signal decrease and recovery that roughly coincides with the shape of the pump pulse. However, the signal does not recover fully. It kind of plateaus at pump delays $> 25\,\text{ps}$. From the data in Figure 3.6, we can estimate that the recovery time from this plateau is substantially longer than the recovery time of the r^+ mode in the d^--pumped case. In both cases (d^- and r^--pumped) the r^- mode shows a behavior similar to the r^+ mode. The d^+ mode has an almost linear increase in signal strength over the time scale of the experiments. From the data, we can also see that the signal difference for any of the CH_3 modes is larger when we pump the d^- mode compared to pumping the r^- mode. However, there is one caveat. All experiments were conducted using the same power for the pump pulse. Nonetheless, it is not necessarily true that the overlap of the probe and pump pulses was exactly the same throughout all

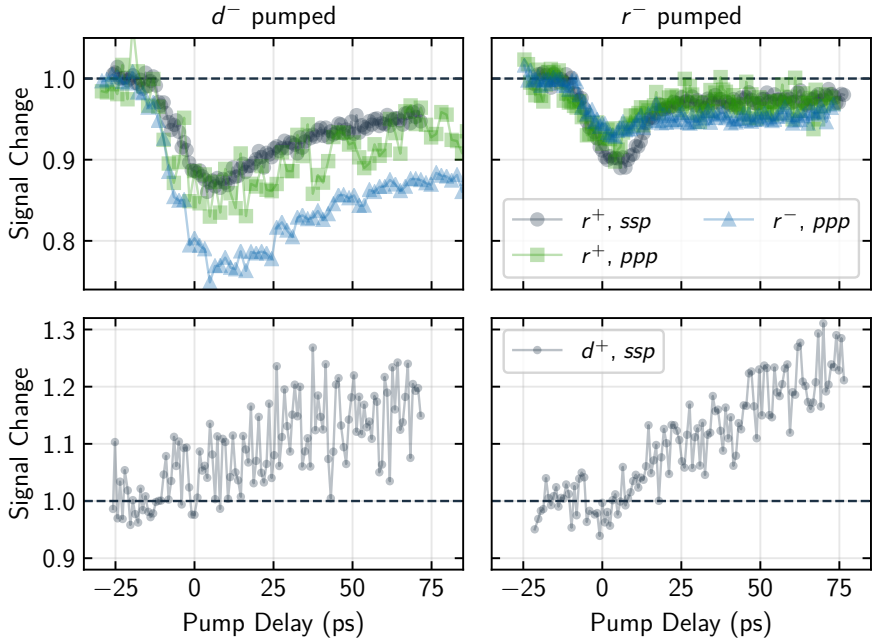

Figure 3.6: Fractional signal change with respect to the pump delay around the resonance frequencies of the d^+ and r^+ modes in *ssp* polarization as well as the r^+ and r^- modes in *ppp* polarization.

measurements. Consequently, the change in signal can vary between single measurements and makes them incomparable in this regard. However, we found that the signal decrease is generally smaller when pumping the r^- than when pumping the d^- mode. We got the same result from the data of the resonant experiment in Section 3.1.

3.3.2 Obtaining Attenuation Parameters

Before we get to a possible explanation for the different transients depending on the pumped mode, we try to get a more accurate procedure than mere integration to determine the signal change of the resonances. Currently, we run into the problem that the signals of adjacent resonances are convoluted. For example there is an indication that the r^+_{fr} resonance is heavily convoluted with another resonance (see Figure 3.2). In this case, the change in the observed signal does not directly correlate to the change in the line strength. If we only had one resonance in our spectrum, the observed intensity I_{SF} would be proportional to A^2:

$$I_{\mathrm{SF}} \propto A^2 \tag{3.10}$$

However, this is not the case if the resonance in question is convoluted with another resonance, as is the case in our spectra. So, what we want to try now is assigning oscillator

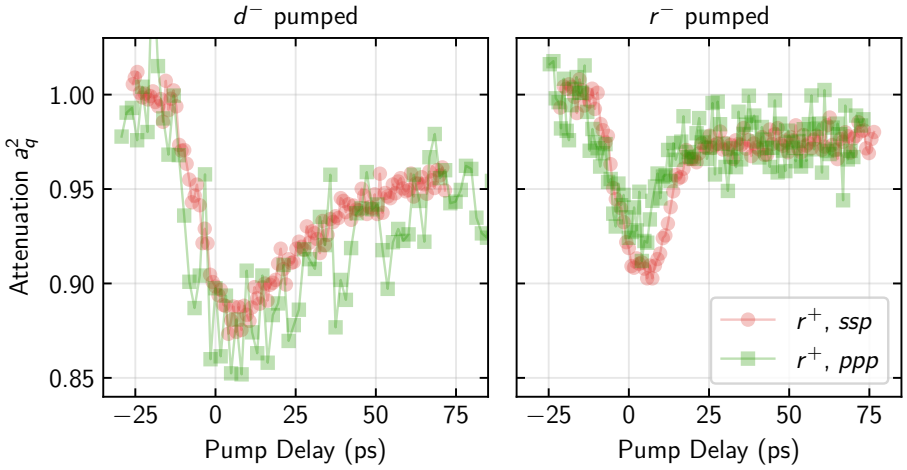

Figure 3.7: Attenuation parameters for the r^+ mode in *ssp* and *ppp* polarization. The attenuation of the oscillator strength a_q is squared for better comparability with the change in signal shown in Figure 3.6.

strengths A_q^* to every single spectrum in the delay scan series in Figure 3.5. We already evaluated the resonance frequencies ω_q and damping coefficients Γ_q so that we can treat them as fixed. This approach is not necessarily exact. However, this will considerably reduce the scatter of the fitted oscillator strengths A_q^*. We can obtain the attenuation coefficients a_q of the oscillator strengths from

$$a_q = \frac{A_q^*}{A_q} \tag{3.11}$$

where A_q^* and A_q are the oscillator strengths of the pumped and non-pumped spectra, respectively (see Equation 3.8). In order to compare these attenuation coefficients to the integrated signal in Figure 3.6, we have to consider that $I_{\mathrm{SF}} \propto a_q^2$ in case there is no convolution with other modes.

3.3.3 Fit Results

Upon fitting each spectrum in the delay-series, we find that for the r_{fr}^+ as well as the d_ω^- at 2906 cm^{-1} modes, the oscillator strength does not significantly change when pumping the system. If we redo the procedure keeping the oscillator strengths for these two modes fixed, we can reduce the scatter in the fitting parameters for the other vibrational modes considerably. The modes which are allowed to change their oscillator strengths are then d^+, r^+, d_ω^- at 2887 cm^{-1}, μ, r_b^-, and r_a^-. How do the fitted attenuation coefficients compare to the integrated signal?

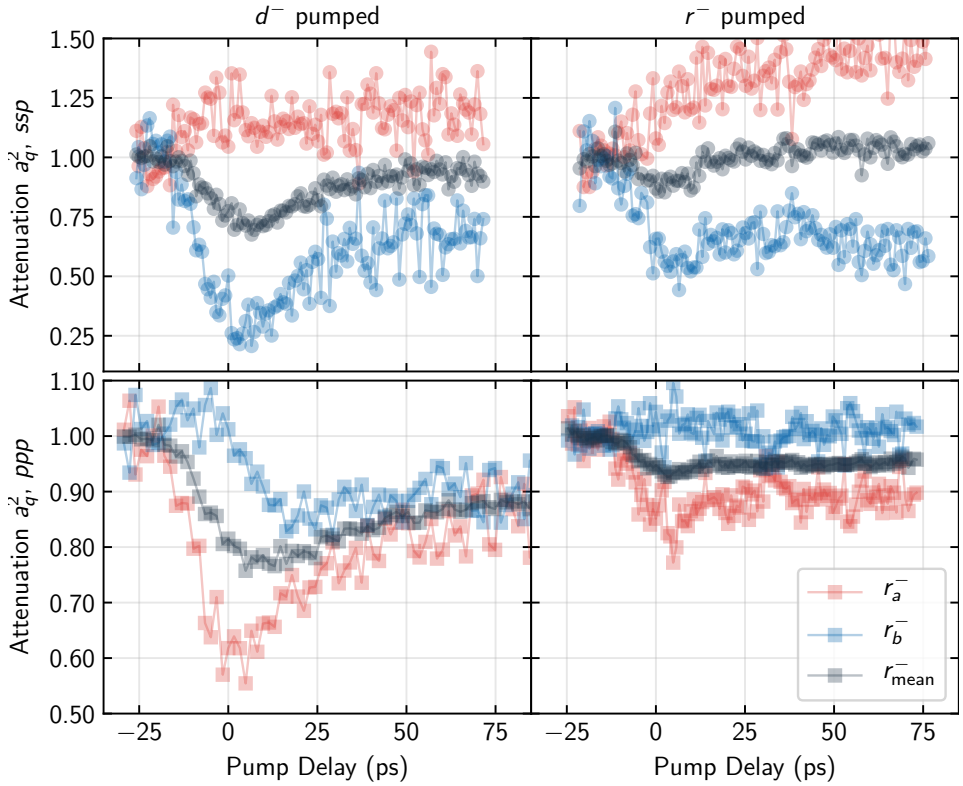

Figure 3.8: Change in oscillator strengths for the r_a^- (red) and r_b^- (blue) modes in *ssp* (upper plots) and *ppp* (lower plots) polarization. The mean of the values for both modes is plotted in black. The attenuation of the oscillator strength a_q is squared for better comparability with the change in signal shown in Figure 3.6.

CH_3 Symmetric Stretch

First, we take a look at the r^+ mode of which we already plotted the integrated signal in Figure 3.6. The data are shown in Figure 3.7. By just looking at the data, there is no qualitative difference to the integrated signal in Figure 3.6. Also, the signal-to-noise ratio seems to be similar. The quantitative difference with respect to the absolute amount of change between the signal change and a_q^2 is only around 1 %. Concerning the r^+ modes, we can conclude that there is no advantage in fitting the spectra to obtain the a_q^2 values compared to simply integrating the signal.

CH_3 Asymmetric Stretch

We can expect that fitting becomes more relevant for the convoluted modes like r^- though; notably, because we claimed that we could resolve both the r_b^- and r_a^- modes (see Figure 3.4 and Table 3.1). The squared attenuation coefficients a_q^2 for both r^- modes alongside their mean value are plotted in Figure 3.8. The upper plots show the squared attenuation coefficients for the *ssp* spectra. In both cases, d^--pumped (left) and r^--pumped (right), we can see that the r_a^- mode has an attenuation coefficient > 1, indicating that this

resonance shows an increase in oscillator strength. In both cases, the r_b^- mode shows a decrease in signal strength. In the *ppp* spectra, where the r^- modes are the predominant modes in the spectrum, this is not the case. Here, the fitting procedure suggests that in the d^--pumped case, both the r_a^- and r_b^- modes show a decrease in oscillator strength. In this case, the decrease for the r_a^- mode is more pronounced than for the r_b^- mode. In addition, the oscillator strength of the r_b^- mode starts to decrease 25 ps later than the oscillator strength of the r_a^- mode. In the r^--pumped case, we see practically no change in oscillator strength of the r_b^- mode in the *ppp* spectra. For all four data sets, we also plotted the mean values of both traces (black). We can see that the signal-to-noise ratio is much better for this trace. This data suggests that it might not be a good idea to fit the two r^- modes independently from one another, after all.

The transients in Figure 3.8 are not at all what we would expect in two ways:

1. We would expect that both the r_b^- and r_a^- modes show the same transient quantitatively as well as qualitatively.

2. In case there is any reason why point one should not be true, we would at least expect that the transients in *ssp* and *ppp* polarization are similar. This is to be expected because these are merely two ways of probing the system, and the polarization of our probing laser should, in the best case, not have any influence on the system itself.

Other Resonances

What we are missing now are the various CH_2 modes d^+, d_ω^- at 2887 cm^{-1} and the unknown resonance μ. Remember that the line strength of the r_{fr}^+ mode and d_ω^- mode at 2906 cm^{-1} did not show a significant change with the pump delay. The fractional change in line strength of these modes is shown in Figure 3.9. Starting with the d^+ mode in the upper plots, we see that in both cases, d^- pumped and r^- pumped, we see a strong decrease to $\sim$30 % of the original line strength. For longer delay times, we see that the line strength seems to increase steadily. There is no observable d^+ mode in *ppp* polarization, so it is impossible to determine if we fitted the attenuation reasonably well. The same is true for the μ mode, which is also only visible in *ssp* polarization. For the μ mode, with the d^- mode pumped, we see a decrease and a recovery of the line strength on the same time scale as for the r^+ and r^- modes. With the r^- mode pumped instead, we see an increase of the line strength followed by the attenuation going back to normal on the time scale of the pump pulse. For the d_ω^- mode at 2887 cm^{-1}, we see a decrease and a recovery of the line strength for both cases. However, we see that the decrease in line strength is much larger in *ppp* polarization than in *ssp* polarization. The data presented in Figures 3.7 and 3.8 suggest however, that the pump strength is approximately the same in both *ssp* and *ppp* polarization. We can thus deduce that the assignments we did in the fitting are

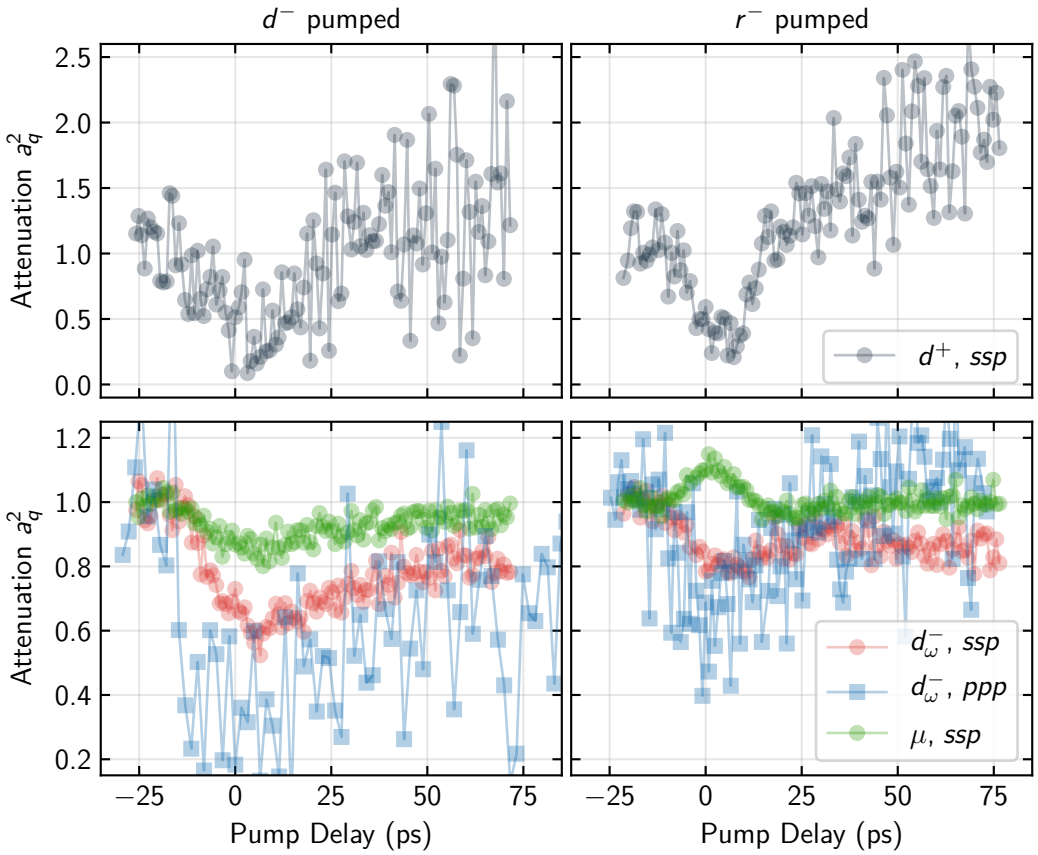

Figure 3.9: Change in oscillator strengths for the d^+ mode in *ssp* polarization (upper plots), the μ mode in *ssp* polarization (lower plots, yellow) and the d_ω^- mode at $2887\,\mathrm{cm}^{-1}$ for both *ssp* and *ppp* polarization (lower plots, red and blue). The attenuation of the oscillator strength a_q is squared for better comparability with the change in signal in Figure 3.6.

not accurate. We are probably looking at two different modes or, we missed additional resonances in the spectra.

In Figure 3.2 we discussed the possibility of observing a signal increase in the SF spectrum even though no mode shows an increased line strength. We presumed that this was caused by the convolution of the r_{fr}^{+} mode with another resonance. The data indicate that the signal increase is caused by the convolution of the r_{fr}^{+} and the μ mode. The r_{fr}^{+} signal does not change over time while the signal of the μ mode does.

3.3.4 Recovery of the slow component

From the r^{-}-pumped spectra in Figure 3.7, it is apparent that the signal of the r modes does not fully recover within ∼200 ps after the pump pulse hits the sample. This is also true for the d^{-}-pumped spectra, however, not apparent on the time scale of the measurements displayed here. Therefore, we performed measurements with delay times up to 1.25 ns. Figure 3.10 shows the signal decrease of the r^{+} band in such a measurement. Even at delay times of 1.25 ns, the signal has not recovered completely. Furthermore, the signal-to-noise ratio does not allow for an estimate of the time constant of this slow component in the recovery. To access longer delay times, we altered the synchronization of the *PG711* pump-IR laser with the *Pharos*. The pump laser is seeded from the oscillator of the *Pharos* which runs at 76 MHz. Therefore, picking different pulses from the oscillator to seed the pump laser, allows us to take measurements with pump delays of more than 13 ns. However, the temporal resolution of these measurements is limited by the oscillator frequency of the *Pharos* with pump delay steps of ∼13.2 ns. These measurements show that the signal has already recovered after 13 ns. Based on this data, we can estimate a recovery time for the

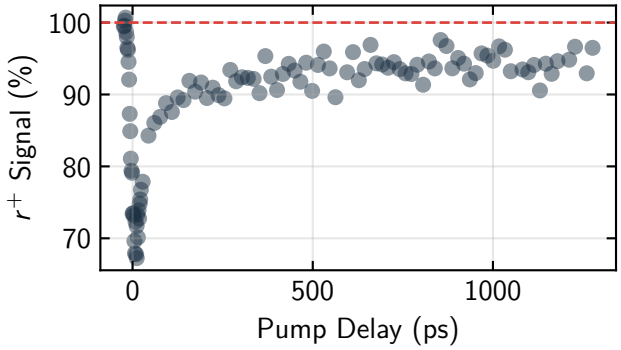

Figure 3.10: Signal change of the r^{+} band in d^{-}-pumped spectra with pump delays up to 1.25 ns. Signal recovery is very slow and can not be resolved by the delay accessible in our experimental setup. Measurements with pump delays of 13 ns on the other hand indicate a complete recovery of the signal in this time span.

slow component between 2 and 13 ns.

3.3.5 Summary

So, what can we learn from this? We can not describe the spectra appropriately with the number of resonances and the assignments we got from the fitting procedure. While we can fit the static spectra each for itself reasonably well, we can see that there are flaws as soon as we compare the change in line strengths between *ssp* and *ppp* polarization. While the attenuation of the r^+ mode shows the same transient in both polarization combinations, this is not the case for the r^- modes and d^-_ω mode at 2889 cm^{-1}. However, taking the mean of the attenuation parameters of the r^-_a and r^-_b modes results in similar transients. The transients of the attenuation parameter of the r^+ modes fulfill our expectations. This suggests that at least the fitting of the r^+ resonance is valid in both polarization combinations. The transients of the attenuation parameters of all the other modes either have a low signal-to-noise ratio or are unique to one polarization combination (for example, d^+ and μ) so that we must consider the fitted attenuation parameters for these modes as too uncertain to be worthwhile for further consideration – at least quantitatively. In general, the transients are substantially different between the r^- and d^--pumped cases. This difference is especially apparent for the r^+ mode. In the next section, we will work out how we can explain the differences in the transients.

3.4 Reservoir Model

In the previous chapter, we took a look at the attenuation of the various modes. Let us again take a look at the d^--pumped case displayed Figure 3.7. Here, the attenuation slowly goes back to a value of 1.0 with a time constant of $\sim$20 ps. On the other hand, in the r^--pumped case, the attenuation value goes immediately back to (almost) 1.0. In the latter case, the transient closely follows the temporal shape of the laser pulse. Keep in mind that the FWHM of the pump pulse was approximately 20 ps. In this chapter, we will develop a model to help us answering the following questions:

- How can we explain the difference in transients between the d^- and r^- pumped cases?
- Which vibrational modes are coupled and how strong is this coupling?
- What are the population relaxation times of the involved vibrational modes?
- What is the preferred pathway of vibrational energy relaxation from the high-energy CH stretches?
- To which extent does structural disorder in the calcium arachidate monolayer play a role in the attenuation of the sum-frequency signal?

To this end, we will first develop a rough model to qualitatively explain the difference in transients. Next, a thorough mathematical description of the model follows. In the last part, we will fit the model to the data and interpret the results to answer the questions posed above.

3.4.1 A Makeshift Explanation

The calcium arachidate molecule ($CaC_{20}H_{39}O_2$) with its $N = 62$ individual atoms has $3N - 6 = 180$ individual normal modes. Here, of course, we disregard that two arachidate ions share one calcium ion. As we can guess, it would be a highly complex task to keep track of the energy content in every single vibrational mode. Luckily, we may combine multiple of these normal modes into reservoirs, making the task of keeping track of the energy flow in the molecule more manageable. The criteria for combining several normal modes could be:

1. The modes are similar in energy.
2. The modes can not be distinguished experimentally.
3. The energy exchange between the modes is so fast it can not be resolved experimentally.

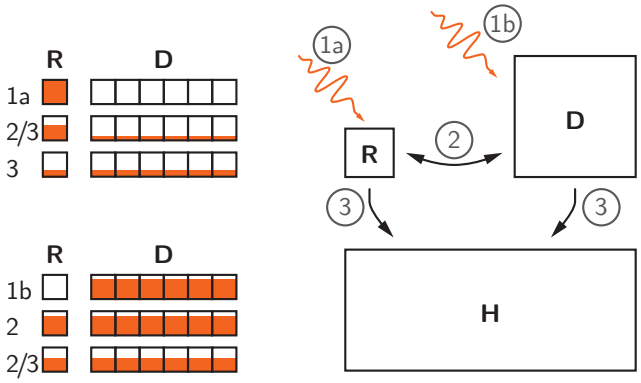

Figure 3.11: A qualitative explanation of the different recovery times observed when pumping the r^- and d^- modes: In the r^--pumped case, the energy is initially induced in the R reservoir. From there, the system quickly transfers most of the energy into the H reservoir. In the d^--pumped case, the energy is induced in the D reservoir. From there, the energy redistributes relatively slowly between the R and D reservoirs. The energy transfer to the H reservoir may happen from the R and/or D reservoir.

In our model, we combine all deformation modes since all of these are low in energy ($500\,\mathrm{cm}^{-1}$ to $1800\,\mathrm{cm}^{-1}$), and we can not resolve them in our experiment. We have one normal mode per CH bond that can be attributed to either a CH_2 or CH_3 stretching vibration. With this, we have 36 normal modes that we can count towards the CH_2 stretching vibrations and 3 normal modes that we can attribute to the CH_3 stretching vibrations. That leaves 141 low energy stretching and deformation modes of the various C–C and C–O bonds. Let us also combine all CH_2 modes and CH_3 modes in their respective reservoirs. Of course, we can distinguish between, for example, the r^+ and the r^- mode in our experiment. However, to a first approximation, let us assume the energy transfer between those modes is so fast that we can not resolve it experimentally and is faster than the coupling to other vibrational modes.

We now have three energy reservoirs:

1. The R reservoir, representing all CH_3 stretching modes,
2. the D reservoir, representing all CH_2 stretching modes and
3. the H reservoir, representing all low-energy deformation modes.

With these, we can explain the transients in the following way.

r^--Pumped

In the r^--pumped case, the energy is put in the asymmetric stretching vibration of the CH_3 mode and redistributes rapidly between the asymmetric and symmetric stretching vibrations. A small amount of vibrational energy redistributes to the stretching vibrations

of the CH_2 modes. However, the relaxation pathway to the deformation modes is much quicker. This energy relaxation happens most likely through the Fermi resonance of the CH_3 symmetric stretch [16, 25–27]. This quick energy relaxation process is the reason why the signal closely follows the temporal profile of the laser pulse.

d^--Pumped

In the d^--pumped case, the energy is induced into the asymmetric CH_2 stretching modes. From here, the energy slowly redistributes to the CH_3 stretching vibrations and relaxes relatively quickly into the deformation modes. However, because the CH_3 modes are constantly "fed" by the vibrational energy coming from the CH_2 vibrations, they appear to relax at a longer time scale. This explains the slow recovery compared to the r^--pumped case. Figure 3.11 shows this process schematically. Additionally, more energy gets absorbed by the asymmetric CH_2 stretching modes than by the asymmetric CH_3 stretching modes. Because of this, the overall attenuation of the modes is more pronounced in the d^--pumped case.

With this model in place, we can further specify the question about the energy relaxation pathway. The question now arises whether the preferred relaxation pathway to the H reservoir is from the D or the R reservoir. It is also possible that both pathways are equally involved in the relaxation.

3.4.2 Mathematical Model

The previous section showed that we could employ a model with three reservoirs representing the CH_3 stretching modes, CH_2 stretching modes, and deformation modes to describe the different transients in the pump-probe experiments. This section gives a thorough mathematical description of this model and shows how to relate the data we get from this model to the experimental data.

Transitions Between Modes with Similar Energy

Let us assume a system with two normal modes R, and D. We can represent each state the molecule can be in with $\langle R|D\rangle$ where $R = 1$ if the R mode is excited and $R = 0$ if it is not. The same applies to the D mode. The system can be in the following four states: $\langle 0|0\rangle$, $\langle 1|0\rangle$, $\langle 0|1\rangle$ and $\langle 1|1\rangle$.

It is not convenient to model the population in these states directly. If we added more modes to the model, the number of possible states of the system would grow exponentially. Rather than assigning a population to a certain state of the molecule, we can express this with the probability that a certain normal mode in a randomly selected molecule is excited. These probabilities are u_R for the R modes and u_D for the D modes. Let us say we can

prepare the system in such a way, so the probability of finding an excited R mode is $u_R = 0.4$, and the probability of finding an excited D mode is $u_D = 0.3$. This is all the information we need to calculate the relative population N in each of the four states of the system.

$$\begin{aligned} N_{\langle 1|1\rangle} &= u_R \cdot u_D && = 0.12 \\ N_{\langle 1|0\rangle} &= u_R \cdot (1 - u_D) && = 0.28 \\ N_{\langle 0|1\rangle} &= (1 - u_R) \cdot u_D && = 0.18 \\ N_{\langle 0|0\rangle} &= (1 - u_R) \cdot (1 - u_D) && = 0.42 \end{aligned} \tag{3.12}$$

A caveat of this approach is that we always have to assume a random distribution of excited normal modes across all molecules. For example, if we somehow prepared a system with relative populations $N_{\langle 0|0\rangle} = 0.42$, $N_{\langle 1|1\rangle} = 0.58$ and $N_{\langle 1|0\rangle} = N_{\langle 0|1\rangle} = 0.0$, there is no solution for the system of equations above. We could not describe the state of the system via probabilities u_R and u_D. In this case, we have to assume the system equilibrates itself rapidly, meaning the distribution of normal modes randomizes itself across all molecules in the system. This would then again yield the relative populations in Equations 3.12. Physically, we can justify this by taking the intermolecular transfer of vibrational energy into account. In Section 1.3 we saw that this intermolecular transfer happens on a short time scale of just a few picoseconds [25].

How do the probabilities change if there is a process causing the system to transfer energy from the R to the D mode and vice versa? To illustrate this, let us assume we manage to do this transition for 50 % of the molecules in the system per time step. The rate constants for the transitions are then $k^*_{R\leftrightarrow D} = 0.5\,[\mathrm{T}^{-1}]$. If we assume that the normal modes R and D are similar in energy, it is a valid assumption that the probabilities are the same both ways. The transition from R to D is only possible if the molecule has an excited R mode, but the D mode is not excited. The transition from R to D is only possible if R is excited, but D is not. Hence, the transition rate r from R to D is

$$\begin{aligned} r_{R\to D} &= k^*_{R\leftrightarrow D} \cdot N_{\langle 1|0\rangle} \\ &= k^*_{R\leftrightarrow D} \cdot (u_R - u_R u_D) = 0.14 \end{aligned} \tag{3.13}$$

and the rate from D to R is

$$\begin{aligned} r_{D\to R} &= k^*_{R\leftrightarrow D} \cdot N_{\langle 0|1\rangle} \\ &= k^*_{R\leftrightarrow D} \cdot (u_D - u_R u_D) = 0.09\ . \end{aligned} \tag{3.14}$$

Since we want to describe the dynamics of the populations, we are interested in the change in probabilities. The change in probability for a randomly selected molecule to have an

excited R is then

$$\begin{aligned}\frac{\mathrm{d}u_R}{\mathrm{d}t} &= r_{R\leftrightarrow D} - r_{R\leftrightarrow D} \\ &= k^*_{R\leftrightarrow D}\cdot(u_D - u_R u_D) - k^*_{R\leftrightarrow D}\cdot(u_R - u_R u_D) \\ &= k^*_{R\leftrightarrow D}\cdot(u_D - u_R) = -0.05\end{aligned} \tag{3.15}$$

and the change in probability to have an excited D is

$$\frac{\mathrm{d}u_R}{\mathrm{d}t} = k^*_{R\leftrightarrow D}\cdot(u_R - u_D) = 0.05 \tag{3.16}$$

giving $u_R = u_D = 0.35$.

The relative populations in each state are now the following:

$$\begin{aligned}N_{\langle 1|1\rangle} &= u_R \cdot u_D && = 0.123 \\ N_{\langle 1|0\rangle} &= u_R \cdot (1-u_D) && = 0.227 \\ N_{\langle 0|1\rangle} &= (1-u_R)\cdot u_D && = 0.227 \\ N_{\langle 0|0\rangle} &= (1-u_R)\cdot(1-u_D) && = 0.423\end{aligned} \tag{3.17}$$

States $N_{\langle 1|0\rangle}$ and $N_{\langle 0|1\rangle}$ are now in an equilibrium and the relative populations will not change anymore. Note that the relative populations add up to 1.

Transitions Between Reservoirs that Represent a Different Number of Normal Modes

What happens to the transition rates and relative populations if R and D now each represent a number N_R and N_D of normal modes? To keep things simple let us say that $N_R = 1$ and $N_D = 2$. Since the system now has a total of three different normal modes the number of states increases to $N_{\text{states}} = 2^{N_{\text{modes}}} = 8$. Let us revert to the initial probabilities $u_R = 0.4$ and $u_D = 0.3$. The relative populations in each state are then the following:

$$\begin{aligned}N_{\langle 1|\{1|1\}\rangle} &= u_R \cdot u_D^2 && = 0.036 \\ N_{\langle 1|\{0|0\}\rangle} &= u_R \cdot (1-u_D)^2 && = 0.196 \\ N_{\langle 1|\{1|0\}\rangle} &= u_R \cdot u_D \cdot (1-u_D) && = 0.084 \\ N_{\langle 1|\{0|1\}\rangle} &= u_R \cdot (1-u_D)\cdot u_D && = 0.084 \\ N_{\langle 0|\{1|1\}\rangle} &= (1-u_R)\cdot u_D^2 && = 0.054 \\ N_{\langle 0|\{1|0\}\rangle} &= (1-u_R)\cdot u_D \cdot (1-u_D) && = 0.126 \\ N_{\langle 0|\{0|1\}\rangle} &= (1-u_R)\cdot(1-u_D)\cdot u_D && = 0.126 \\ N_{\langle 0|\{0|0\}\rangle} &= (1-u_R)\cdot(1-u_D)^2 && = 0.294\end{aligned}$$

Following Equations 3.13 and 3.14 the transfer rate between the R mode and the D modes is

$$\begin{aligned}\frac{\mathrm{d}u_R}{\mathrm{d}t} &= k^*_{R\leftrightarrow D}\cdot(N_{\langle 0|\{1|0\}\rangle} + N_{\langle 0|\{0|1\}\rangle} + 2N_{\langle 1|\{0|0\}\rangle} - 2N_{\langle 1|\{0|0\}\rangle} - N_{\langle 1|\{1|0\}\rangle} - N_{\langle 1|\{0|1\}\rangle}) \\ &= 2k^*_{R\leftrightarrow D}\cdot(u_D - u_R)\ . \end{aligned} \tag{3.18}$$

And

$$\begin{aligned}\frac{\mathrm{d}u_D}{\mathrm{d}t} &= k^*_{R\leftrightarrow D}\cdot(N_{\langle 1|\{0|0\}\rangle} + N_{\langle 1|\{0|1\}\rangle} - N_{\langle 0|\{1|0\}\rangle} - N_{\langle 0|\{1|1\}\rangle}) \\ &= k^*_{R\leftrightarrow D}\cdot(u_R - u_D) \end{aligned} \tag{3.19}$$

between one of the D modes and the R mode. This shows that effectively, for a combination of arbitrary many R and D the transfer rates are

$$\frac{\mathrm{d}u_R}{\mathrm{d}t} = N_D\cdot k^*_{R\leftrightarrow D}(u_D - u_R) \tag{3.20}$$

and

$$\frac{\mathrm{d}u_D}{\mathrm{d}t} = N_R\cdot k^*_{R\leftrightarrow D}(u_R - u_D)\ . \tag{3.21}$$

We then have effective transfer rates $k_{R\to D} = N_D k^*_{R\leftrightarrow D}$ and $k_{D\to R} = N_R k^*_{R\leftrightarrow D}$.

Transitions to the Low-Energy Vibration Regime

As discussed earlier in Section 1.2, a high energy vibration may relax into multiply low energy vibrations and and phonons. This does not change the fundamentals discussed in the previous paragraphs. In our model, we can represent the low energy states with H. So the transfer rate from R to H is

$$\frac{\mathrm{d}u_R}{\mathrm{d}t} = N_H\cdot k^*_{R\leftrightarrow H}(u_H - u_R)\ . \tag{3.22}$$

However, there is a difference in how we must interpret the population u_H. In contrast to the interpretation of u_D and u_R, this is not the probability of finding a random molecule with a specific low energy mode excited. In this case, we have to interpret it as the probability that the specific set of vibrations and phonons is excited. More specifically, those into which the high-energy vibrations relax. For example, a high-energy vibrational mode Q_1 relaxes into two low-energy vibrational modes Q_2 and Q_3 plus a phonon q_4. We can now interpret u_H as the probability that in a randomly selected molecule Q_2, Q_3, and q_4 are all excited at the same time.

Redistribution to the Heat Bath

To remove the energy from the system, we can let it redistribute into a heat bath. In our system, the heat bath is represented by the phonons of the glass substrate. We can assume that the energy transfer to the heat bath happens preferably from the low-energy vibrational modes of the molecule represented by reservoir H. A direct energy transfer from the high-energy modes would be very unlikely (see Chapter 1.2). The transfer rate from reservoir H to the heat bath is then

$$\frac{\mathrm{d}u_R}{\mathrm{d}t} = -k_{H\rightarrow} \cdot u_H \ . \tag{3.23}$$

Stimulated Transitions

Transitions can be stimulated by a laser pulse. Let us assume the case in where we drive the transition into or from an R mode. We have two possibilities. Firstly, we can excite the R mode. This is only possible if the specific R mode is not yet excited. The excitation rate is then

$$\frac{\mathrm{d}u_{R,\mathrm{ex}}}{\mathrm{d}t} = f_{\mathrm{Laser}}(t) \cdot x_{\leftrightarrow R} \cdot (1 - u_R) \tag{3.24}$$

where $f_{\mathrm{Laser}}(t)$ is a function that describes the time-dependent intensity of the laser pulse and $x_{\leftrightarrow R}$ is the transition rate constant to the R mode. $(1 - u_R)$ is the probability that the R mode is currently not excited. Similarly, for the de-excitation to occur an R mode has to be excited. The de-excitation rate is therefore

$$\frac{\mathrm{d}u_{R,\mathrm{deex}}}{\mathrm{d}t} = -f_{\mathrm{Laser}}(t) \cdot x_{\leftrightarrow R} \cdot u_R \ . \tag{3.25}$$

If we add those two rates, we derive an overall transition rate of

$$\frac{\mathrm{d}u_R}{\mathrm{d}t} = x_{\leftrightarrow R} \cdot (1 - 2u_R) \tag{3.26}$$

where $x_{\leftrightarrow R}$ is the effective pump rate constant.

We can describe the time-dependent intensity of the laser pulse $f_{\mathrm{Laser}}(t)$ by a Gaussian profile

$$f_{\mathrm{Laser}}(t) = e^{-\frac{(t-t_0)^2}{\sigma^2}} \ . \tag{3.27}$$

Here, t_0 is the point in time at which the pump pulse has its maximum intensity and σ is its standard deviation. The relation between FWHM and the standard deviation of a Gaussian distribution is given by $\mathrm{FWHM} = 2\sqrt{2\ln 2} \cdot \sigma$.

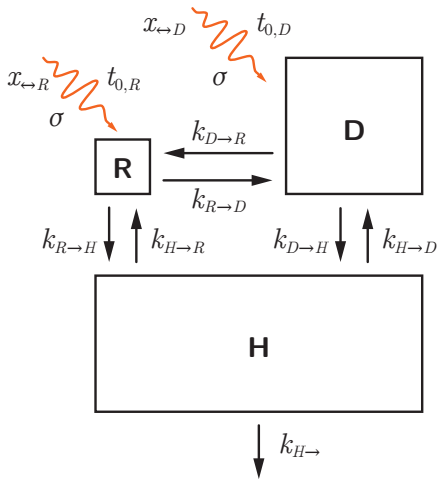

Figure 3.12: Illustration of the proposed model with reservoirs R, D and H and all parameters.

Summary

For a model with three states R, D and H the full set of differential equations that describe the population in each of these states is

$$\begin{aligned}
\frac{\mathrm{d}u_R}{\mathrm{d}t} &= k_{R\to D}(u_D - u_R) + k_{R\to H}(u_H - u_R) + x_{\leftrightarrow R}(1-2u_R)\cdot f_{\text{Laser}}(t) \\
\frac{\mathrm{d}u_D}{\mathrm{d}t} &= k_{D\to R}(u_R - u_D) + k_{D\to H}(u_H - u_D) + x_{\leftrightarrow D}(1-2u_D)\cdot f_{\text{Laser}}(t) \\
\frac{\mathrm{d}u_H}{\mathrm{d}t} &= k_{H\to R}(u_R - u_H) + k_{H\to D}(u_D - u_H) - k_{H\to}\cdot u_H\ .
\end{aligned} \tag{3.28}$$

Note that in the case where we pump the r^- mode $x_{\leftrightarrow D} = 0$ and when we pump the d^- mode $x_{\leftrightarrow R} = 0$. The model is illustrated in Figure 3.12.

3.4.3 Calculate Attenuations

Still, we have to relate the experimental data to the data obtained by the reservoir model. To do this, we have to calculate the attenuation parameters a from the modeled excitation probabilities u. Hereby, we will take a look at two kinds of transitions: fundamental transitions and hot band transitions.

Note that the sum-frequency intensity I_{SF} changes quadratically with a. Since $I_{q,\text{SF}} \propto |a_q \cdot A_q|^2$, an attenuation of $a_q = 0.9$ would mean that the sum-frequency intensity decreases by 19 %.

Fundamental Transitions

Fundamental transitions are those between the vibrational ground state and the first excited state ($v = 0 \leftrightarrow v = 1$). The idea is the same as for the stimulated transitions

discussed in the previous section. For the excitation to occur, the excited state has not yet to be excited. The probability p_{ex} for the excitation into one of the R modes is

$$p_{\text{ex}} \propto 1 - u_R \ . \tag{3.29}$$

Analogously, the probability for the de-excitation is

$$p_{\text{deex}} \propto u_R \ . \tag{3.30}$$

Therefore, the oscillator strength of any R mode A_R will be

$$A_R \propto p_{\text{ex}} - p_{\text{deex}} \propto 1 - 2u_R. \tag{3.31}$$

The attenuation parameter $a_R = a_{r^+} = a_{r^-}$ is then

$$a_R = 1 - 2u_R \ . \tag{3.32}$$

Hot Band Transitions

Hot band transitions are transitions between excited vibrational states, for example ($v = 1 \leftrightarrow v = 2$). For the transition from $v = 1$ to $v = 2$ to occur the fundamental has to be excited: $p_{\text{ex,hot}} = u_q$. In our model, we do not consider the second excited state. Realistically, we can expect that the population in this state is near 0 and with that $p_{\text{deex,hot}} \approx 0$. The observed time-dependent oscillator strength $A^*_{q,\text{hot}}(t)$ is then proportional to the population of the first excited state of mode q. Furthermore, from this, we can deduce the "real" oscillator strength of the hot band by

$$A_{q,t,\text{hot}}(t) = u_q(t) \cdot A_{q,\text{hot}} \ . \tag{3.33}$$

Signal Change through Structural Disorder

The sum-frequency signal strongly depends on the ordering of the probed molecular layer (see Section 2.1). Disorder can, for example, be caused by heating the molecular layer. For a single layer of long-chain fatty acid molecules, the disorder is mainly caused by gauche defects. On the one hand, this disorder leads to an attenuation of the signal of the non-isotropically distributed CH_3 groups. On the other hand, we can expect a signal enhancement of the isotropically distributed CH_2 groups. In the context of our model, we have to have a reservoir whose population represents the amount of heat that is currently in the system. This is what the H reservoir that we discussed in Section 3.4.1 does. The

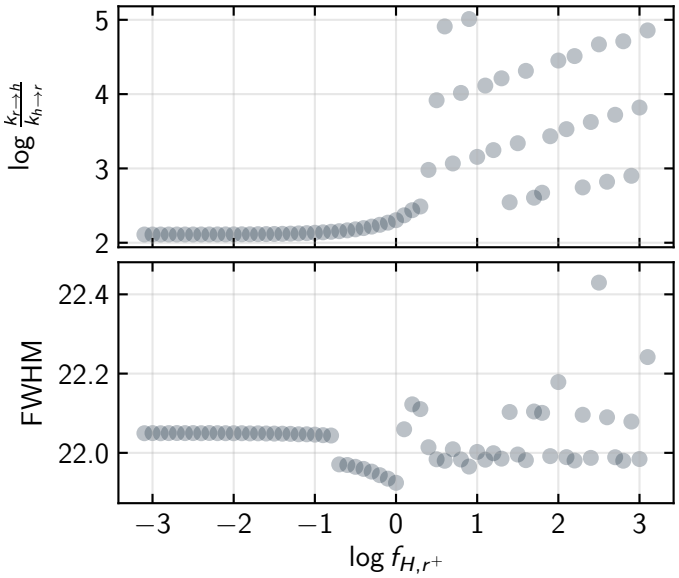

Figure 3.13: Influence of the choice of the model parameter f_{H,r^+} on other model parameters. For choices between $f_{H,r^+} = 10^{-3}$ and 10^{-1} all other model parameters are stable, i.e. they do not show a significant change or fluctuation in value. For values of $f_{H,r^+} > 10^{-1}$ the fitted values for the other model parameters show significant change in value as well as fluctuations. The goodness of the fit does not depend on the choice of f_{H,r^+}. For this reason we fixed f_{H,r^+} to a value of 10^{-2}.

attenuation a of a resonance q is then

$$a_{H,q} = 1 - u_H \cdot f_{H,q} \; . \tag{3.34}$$

Here, u_H represents the population of the H reservoir, and $f_{H,q}$ is a parameter that scales the attenuation of a mode with its population. For CH_3 modes $f_{H,q}$ should be positive, and negative for CH_2 modes. For simplicity, we assume a linear correlation between the attenuation of a mode and the population of the H reservoir. The total attenuation of the fundamental transition of any mode q is then

$$a_q = (1 - 2u_q) \cdot (1 - u_H \cdot f_{H,q}) \; . \tag{3.35}$$

With Equations 3.28 and 3.35 we have a theoretical model to which we can directly compare our experimental data. We will fit this model to the transients of the r^+ attenuation parameters in the next section.

3.4.4 Fit Results

By fitting the model described above, we obtained the results that are presented in this section. We fitted the model detailed in Section 3.4 to the attenuation parameters of the

symmetric CH_3 stretch a_{r^+}. Also, we constrained ourselves to the attenuation parameter obtained from the *ssp* spectra in the data set that we discussed previously. The attenuation of the r^+ mode in the *ppp* spectra looks very similar to the attenuation in the *ssp* spectra (see Figure 3.7). Therefore, we do not expect dissimilarities in the fit result that would be obtained from this data set.

In the optimization process, we fixed some of the model parameters to physically reasonable values. We did this primarily to reduce computation time but also to avoid "instabilities" in other model parameters, as we will see below. The following parameters are fixed or limited in the fitting process:

- The parameter f_{H,f^+} that relates the population in the H reservoir to the signal change through structural disorder is fixed to a value of 1×10^{-2}. We did this to avoid fluctuations in other parameters of the model, as Figure 3.13 shows. However, the model fits the data well for a wide range of f_{H,r^+} values, whereby other parameters depend heavily on the choice of f_{H,r^+}.

- The pump rate ratio $N_D x_{\leftrightarrow D}/N_R x_{\leftrightarrow R}$ is limited to values between 1.5 and 3.0. This implies that the asymmetric CH_2 stretch absorbs at a maximum tree times more photons than the asymmetric CH_3 stretch. The RAIR spectrum in Figure 3.3 suggests that this is a reasonable value range.

- The ratio of population transfer rates $k_{R\to D}$ and $k_{D\to R}$ is fixed to 12. As discussed previously, this is the value that we would theoretically expect from the ratio of CH_2 to CH_3 stretching modes. In Section 4.2 we will discuss if we can expect significantly different transients for different alkyl chain lengths.

- The FWHM of the pump pulse is limited to an upper bound of 22 ps. The cross-correlation data in Figure 2.9 suggests that this is a reasonable upper bound.

- Also, we set the population transfer rate from the deformation modes to the heat bath $k_{H\to}$ to 0. The time scale of the data set is too short for this parameter to have any significant relevance.

Table 3.2 and Figure 3.15 show the fitted parameters. Figure 3.14 shows the fitted transients alongside the data. To estimate the confidence intervals of the various fit parameters, we can use the bootstrap method. The following section briefly describes this method. The fit results follow after that.

Obtaining Confidence Intervals with the Bootstrap Method

Doing data fitting as we did here always begs the question of how accurate the estimated parameters are. By looking at the fit to the data, we see that the model with the estimated

Table 3.2: Fit parameters for the model. The fit results are plotted in Figure 3.14. The FWHM of the pump laser was fitted to 22 ps. The upper bounds of the population transfer rates between the D and H reservoirs are $k_{D\to H} < 0.005\,\mathrm{ps}^{-1}$ and $k_{H\to D} < 1\times10^{-5}\,\mathrm{ps}^{-1}$. All values are given in ps^{-1}.

Parameter	Estimate	95 % Confidence Interval	
$k_{R\to D}$	0.80	[0.74 ,	0.86]
$k_{D\to R}$	0.066	[0.062,	0.072]
$k_{R\to H}$	1.4	[0.9 ,	2.2]
$k_{H\to R}$	0.010	[0.008,	0.012]
$x_{\leftrightarrow R}$	0.046	[0.036,	0.064]
$x_{\leftrightarrow D}$	0.008	[0.006,	0.012]

parameters describes the data reasonably well. However, by just fitting the model to the data, we have no way to tell if the data could not also be well described if we doubled

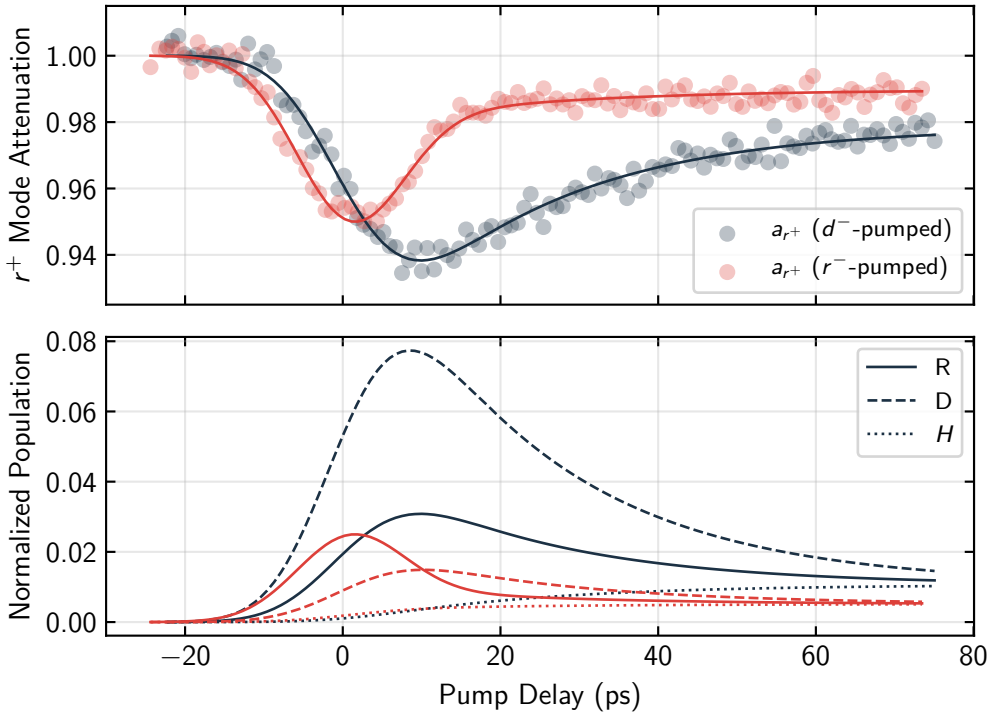

Figure 3.14: The upper plot shows the r^+ mode attenuation data for both the case where the d^- mode (black) and the case where the r^- mode (red) was pumped. The solid lines are the attenuation values that were calculated from the fitted population data that is shown in the bottom plot. Here, the colors show the affiliation to the respective pump-case. The solid lines indicate the population of the R states which are amplified by a factor of 10. The dashed lines and the dotted lines represent the populations of the D and H states respectively. All transients are corrected for the fitted pump-delay-offset t_0 (see Equation 3.27).

a certain parameter. Hence, the question we have to ask is: How much can we change a specific parameter and still describe the data well? In other words, we want to obtain the confidence intervals of the parameters. A convenient way to do this is the bootstrap method [64].

Obtaining confidence intervals with the bootstrap method works by resampling with replacement from the original data. This is the bootstrap sample. The bootstrap sample has the same amount of data points as the original sample. Next, we fit the bootstrap sample and obtain estimates for the model parameters. The sampling and fitting process has to be repeated n times to obtain a Monte Carlo approximation of the estimate. From this distribution of the estimates, we can then obtain the confidence intervals of the individual parameters. n should be at least 1000 to estimate confidence intervals [64].

We use a total of 1000 samples to obtain the distributions of the parameter estimates. The 95 % confidence intervals are then computed with the percentile method. The advantage of this method is that the confidence intervals are easy to compute. However, there can be a substantial coverage error in case the estimates are not distributed normally [65]. This is partially the case for our parameters. Nonetheless, the confidence intervals are accurate enough to give a good idea about the sensitivity of the parameters. The distributions of the estimates are shown in Figure 1 in the appendix.

Fit Results Discussion

Although the model describes the data well, it is important to make sure that the fit parameters are physically reasonable.

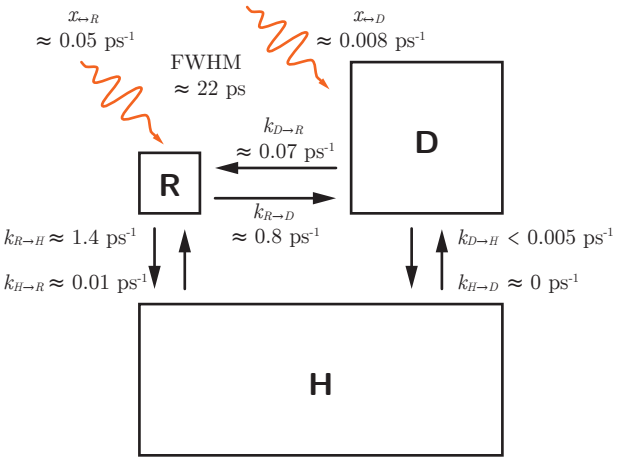

Figure 3.15: Schematic of the reservoir model with population transfer rates between the reservoirs that were obtained by fitting the model to the data.

FWHM The FWHM of the pump pulse was fitted to its upper bound of 22 ps. The cross-correlation measurements in Section 2.1.2 gave a pulse duration of 16 ps. However, the fitted value is still reasonable considering that the temporal profile of the pump pulse strongly depends on the quality of alignment of the optical components of the *PG711* and varies on a day-to-day basis (see Figure 2.9).

Pump Strengths The RAIR spectrum in Figure 3.1 shows an intensity ratio between the d^- and r^- absorption bands of roughly $I_{d^-} \approx 2I_{r^-}$. This gives a ratio of absorbed photons of between the d^- and r^- modes of $r_{\text{abs}} \approx 2$. The pump strength parameters $x_{\to r}$ and $x_{\to d}$ should reflect this. For our model we can calculate this ratio via

$$r_{\text{abs}} = \frac{N_D \cdot x_{\to d}}{N_R \cdot x_{\to r}} \,. \tag{3.36}$$

In this equation, we have to consider the number of normal modes in each reservoir. In the model, all input energy is distributed equally across all normal modes of a reservoir. Therefore, the number of photons absorbed by the system is proportional to the number of normal modes in the respective reservoir N_i and the pump strength parameter $x_{\to i}$. If we calculate this ratio for every bootstrap sample, we get an estimate of $r_{\text{abs}} = 2.4 \pm 0.3$ which is close to the expected value.

Population Transfer Rate from D to H The population transfer rate from the D to the H reservoir has an upper value $k_{D\to H} < 0.005\,\text{ps}^{-1}$. This rate is unexpectedly low compared to the population transfer rate from the R to the H reservoir ($k_{R\to H} \approx 0.80\,\text{ps}^{-1}$). If $k_{D\to H}$ is forcibly increased, the model does not fit the data anymore. The reason for this becomes apparent if we consider the following case. Suppose the population transfer rate from D to H is in the same order of magnitude as from D to R. If we then pump the D reservoir, less than half the energy is redistributed between the D and R reservoirs, and more than half the energy redistributes to the deformation modes. In this case, the population in the R reservoir would be significantly lower than fitted (see Figure 3.14), and the r^+ mode would exhibit a less pronounced signal decrease. We could mitigate this loss in signal decrease by increasing the amount of energy induced into the D reservoir. However, this would also raise the $x_{\leftrightarrow D}/x_{\leftrightarrow R}$ ratio to unreasonable levels. One could argue that the pump laser may have been misaligned in the d^--pumped case so that the pump strengths are not comparable between the two measurements. However, increasing the total amount of energy induced into the system would also increase the level of the trailing "plateau". This would, again, be inconsistent with the data. Thus, in the context of the proposed model, a value of $k_{D\to H} < 0.005\,\text{ps}^{-1}$ seems reasonable.

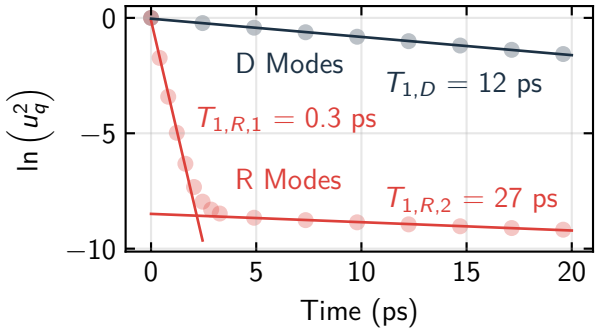

Figure 3.16: Calculated population relaxation times T_1 for the CH_3 stretching modes (red) and the CH_2 stretching modes (black). The data points are simulated with the reservoir model and the solid lines are fits to the simulated data.

Population Relaxation Times There is no direct way to calculate the population relaxation times T_1 from the population transfer rates k. However, we can calculate them indirectly using the reservoir model. How would we proceed if we wanted to get the population relaxation time of the CH_2 stretches? At time $t = 0$, we arbitrarily populate the D reservoir, for example, $u_{D,0} = 0.1$ and let the system equilibrate. From the time-dependence of the population of the reservoir, we can then calculate the intensity of an arbitrary CH_2 mode by $I_D(t) \propto u_D(t)^2$. We can plot the data points logarithmically like in Figure 3.16 and derive the population relaxation time from the slope of the signal decay. By this procedure, we get a relaxation time $T_{1,D} = 12\,\text{ps}$. For the R modes we get two relaxation times $T_{1,R,1} = 0.3\,\text{ps}$ and $T_{1,R,2} = 27\,\text{ps}$. The fast population relaxation time represents the energy relaxation through the r_{fr}^+. The slow component stems from the backfilling of the R reservoir from the D reservoir as, initially, energy redistributes not only into the skeletal modes but also into the CH_2 stretches. The population relaxation of the CH_2 modes happens almost exclusively through the CH_3 modes since the population transfer parameters $k_{d\to h}$ and $k_{h\to d}$ are both ≈ 0.

Attenuation through Structural Disorder With Equation 3.34 we can calculate the amount of attenuation that structural disorder in the monolayers causes. The highest value of the normalized population in the H reservoir is approximately 1×10^{-2} (d^- pumped) and 5×10^{-3} (r^- pumped). With parameter f_{H,r^+} fixed at a value of 1×10^{-2}, the attenuation caused by structural disorder is then $a_{H,r^+} = 1 - u_H \cdot f_{H,r^+} \approx 1 \times 10^{-4}$ and 5×10^{-5} for the d^- and r^- pumped cases respectively. Considering that the total attenuations are two to three orders of magnitude higher than that, this means that structural disorder may not play a significant role in the attenuation of the SF signal.

Originally, the idea was to describe the slow recovery of the signal, which we can see in Figure 3.10 with structural disorder. It turns out that we do not need structural disorder to

describe this "plateau" and the slow recovery. The model suggests that after around 80 ps the R, D, and H reservoirs are nearing thermal equilibrium. At this time, the population of the CH_3 vibrational states is still significant and the main cause for the attenuation of associated resonances. We could model the subsequent slow recovery of the signal with a population transfer $k_{H\rightarrow}$ to the ground state of the molecule. Or, in other words, an energy transfer from the H reservoir to the heat bath.

We can conclude that all parameters are physically reasonable. Thus, the proposed model is suitable for describing the vibrational relaxation process in a calcium arachidate monolayer. Chapter 4 will give a more in-depth discussion of the results.

Summarizing the Fit Results

With the proposed model, we were able to describe the transients of the r^+ modes for both the d^- and r^--pumped cases. For the fitting of the model to the data, we only used data from the *ssp* spectra because of the superior signal-to-noise ratio compared to data from the *ppp* spectra. Since the data look very similar, we can expect the same results for the *ppp* spectra. Thus, including the *ppp* spectra in the fit would not result in significant new insights.

We did not discuss how the attenuation of the various CH_2 modes fits into the model. In practice, including the CH_2 proved to be problematic because of the poor signal-to-noise ratio for the attenuation data of these modes and the high uncertainty involved in fitting these resonances into the spectra. However, in the next section, we will propose a possible explanation for the origin of the μ mode, which we could not assign to a vibrational mode earlier.

Demystifying the μ-Mode

With the proposed reservoir model, we can accurately describe the transients of the attenuation parameters of the r^+ mode. We can now build upon that to explain the transients of other resonances observed in the spectra. Let us take a look at the attenuation parameters of the μ mode, which we were unable to assign to a vibrational mode earlier.

The attenuation parameters are plotted in Figure 3.17. In the d^--pumped case, the attenuation coefficients very much resemble the transient that we already saw for the r^+ mode. In the r^--pumped case, on the other hand, the attenuation parameters distinctly greater than 1 at the time the pump pulse hits the sample. This is followed by values slightly below 1 and a slow recovery of the signal back to an attenuation value of 1.

In the following, we will consider two possibilities regarding the origin of the μ-resonance.

1. The μ-resonance is a hot band of the asymmetric CH_3 stretch superimposed on the resonance of a CH_2 stretch.

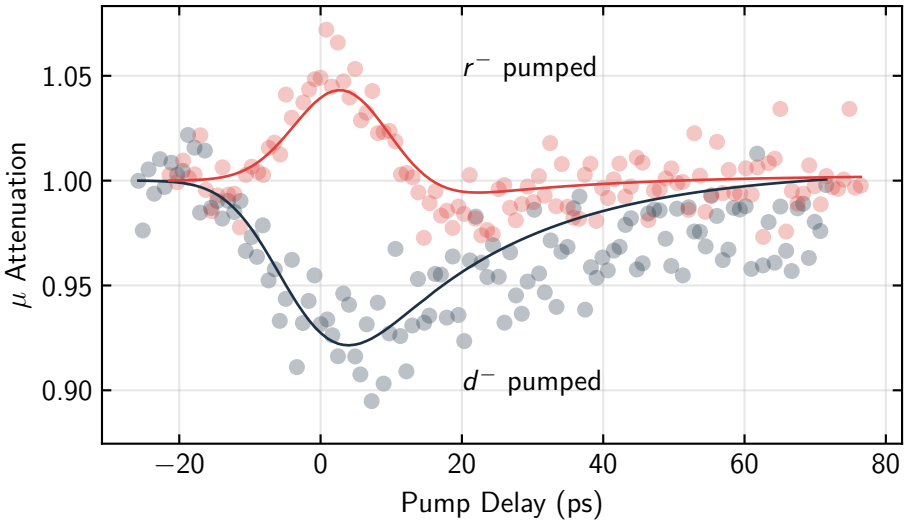

Figure 3.17: Attenuation of the μ mode when pumping the r^- (red) and d^- (black) modes. The solid lines are calculated values from the data in Figure 3.14.

2. The μ-resonance is a fundamental transition shifted in energy due to another mode being excited at the same time. Considering the intensity of the μ-resonance increases upon pumping the r^- mode, the excited mode that could cause this shift may be a CH_3 stretch.

If we assume that the μ-resonance is a hot band of the asymmetric CH_3 stretch superimposed on a CH_2 stretch, we can approximate the expected attenuation with

$$a_\mu \approx (1 - 2u_D) + |A_{r^-,\mathrm{hot}}| \cdot u_R \; . \tag{3.37}$$

The first term is the attenuation of the CH_2 mode and the second term is the oscillator strength of the r^- hot band multiplied by the number of available oscillators in $v = 1$. We can interpret $A_{r^-,\mathrm{hot}}$ as the "real" (time and population independent) oscillator strength of the hot band. It is the only value in the above equation that we can not obtain from the reservoir model.

We can calculate the solid lines in Figure 3.17 with Equation 3.37 setting $|A_{r^-,\mathrm{hot}}| = 2.5$. We are not able to deduce the relative phase of the hot band from this. However, since A_μ is negative this is also the case for $A_{r^-,\mathrm{hot}}$. For comparison, in the *ssp* spectra, $A_{r_b^-}$ and $A_{r_a^-}$ are -0.9 and -1.0, respectively. Interestingly, the hot band does not show up in the *ppp* spectra. Although here, $A_{r_b^-}$ and $A_{r_a^-}$ are -3.7 and -3.4, respectively. These values suggest that the susceptibility of the r^- hot band does not follow Equations 2.6 as would be expected for the asymmetric stretch of a functional group with C_{3v} symmetry. If it would, it would simply scale with the oscillator strengths of the r^- modes, and the hot band would appear stronger in the *ppp* spectra than in the *ssp* spectra.

We fitted the μ mode in the spectrum at a resonance position of 2949 cm^{-1}. Due to the superimposed CH_2, the real position of the resonance of the r^- hot band may differ slightly from that value. With the fundamental transitions of the r_b^- and r_a^- modes being located at 2960 cm^{-1} and 2966 cm^{-1}, respectively, the resonance of the hot band is shifted $\sim$15 cm^{-1} to lower frequencies. We can compare this shift to experimentally obtained line positions of propane. The fundamentals of the asymmetric CH_3 stretches in propane are located at 2967 cm^{-1} and 2968 cm^{-1} [66] (in-plane and out-of-plane). Because of the in-plane and out-of-plane modes, there are three different overtones of the asymmetric CH_3 stretch.

- Both the in-plane and out of plane modes are in the first vibrationally excited state ($v = 1$).
- The in-plane mode is in the second vibrationally excited state ($v = 2$).
- The out-of-plane mode is in the second vibrationally excited state.

We can abbreviate these states with $\langle 1|1\rangle$, $\langle 2|0\rangle$, and $\langle 0|2\rangle$, respectively. The respective line positions of the overtones are 5915 cm^{-1}, 5785 cm^{-1}, and 5739 cm^{-1} [67]. Based on this, we expect the hot bands of the in-plane and out-of-plane vibrations at 2817 cm^{-1} and 2771 cm^{-1}. These are energetically far lower than the μ-resonance at 2949 cm^{-1}. With this, we can rule out that the μ-resonance is a hot band. However, the transition from $\langle 1|0\rangle$ and $\langle 0|1\rangle$ to $\langle 1|1\rangle$ is at a $\sim$2947 cm^{-1} which coincides almost perfectly with the position of the μ-resonance. In this case, Equation 3.37 would still be valid for modeling the attenuation.

In summary, the transients of the attenuation parameter a_μ suggest that μ is not a single resonance in the spectrum but rather an r^- band superimposed on a CH_2 stretching mode. The r^- mode is shifted in energy due to an already excited in-plane or out-of-plane asymmetric stretch. If we compare the oscillator strengths in *ssp* and *ppp* polarization, the results are surprising since the hot band does not appear in *ppp* polarization despite the r^- resonance being much stronger here. This absence suggests that the susceptibilities for the hot band are inherently different from the susceptibilities of the fundamental. This would imply Equations 2.6 are not valid for the hot band transition.

3.4.5 Summary

The model describes the transients of the r^+ mode very well while all parameters are physically reasonable. Contrary to the initial assumption that the "plateaus" in the transients arise from attenuation through structural disorder, this is not necessarily the case. The data suggest that these arise from a long vibrational relaxation time from the deformation modes to the heat bath. In the particular dataset, after $\sim$80 ps all vibrational modes are

in thermal equilibrium. The bottleneck for the signal recovery in the r^--pumped case is the vibrational relaxation from the CH_3 stretching modes to skeletal modes. The time constant associated with this relaxation is 0.7 ps. In the d^--pumped case, the bottleneck for signal recovery is the vibrational energy redistribution between the CH_2 and CH_3 stretching modes. The associated time constant is $N_R \cdot k_{D\to R} \approx 45$ ps.

We could not have obtained these results by naïvely fitting the transients because the underlying dynamics - especially the vibrational relaxation from the CH_3 stretching modes to the deformation modes - are much faster than the excitation pulse. Also, the data suggest that the CH_2 vibrational relaxation happens practically exclusively through the CH_3 stretching modes (and its Fermi resonance).

In theory, we could also use the reservoir model to describe the transients of the r^- and CH_2 stretching modes. However, as pointed out earlier, the data are inconsistent, and we need a more robust description of the features in the SF spectra. The first step towards this goal is already done since we were able to reveal the presence of an r^- hot band in our spectra. Overall, the results suggest that the reservoir model presented here is a suitable tool to analyze additional data sets methodologically.

4 Conclusion and Outlook

4.1 Conclusion

The goal of this thesis was to develop methods to track the vibrational non-equilibrium dynamics in an adsorbate system. The system we chose for this study was calcium arachidate adsorbed on glass. For this purpose, we built a new spectroscopic system, including a narrowband pump-IR pulse and a broadband IR probe pulse in combination with sum-frequency generation.

4.1.1 Experimental

The spectrometer that we built in the context of this thesis proved to be highly capable of performing the desired measurements. The pump range of the spectrometer, however, is limited and does not fully cover the entire C–H stretching region from 2700 to 3100 cm^{-1}. In this work, we were only able to cover the high-energy part of this region with a lower limit of 2910 cm^{-1}. However, the pump pulse also covers the N–H stretch (3000 cm^{-1} to 3450 cm^{-1}) and O-H stretch modes (3000 cm^{-1} to 3900 cm^{-1}) [68]. The spectrometer can probe the entire C–H stretch region. In addition to that, we showed that the spectrometer is capable of probing the N–O stretch region from 1500 to 2100 cm^{-1} [69].

4.1.2 Results

Resonant Pump-Probe Effects

We can deposit energy into the system primarily by pumping the d^- and r^- modes. Note that the pump pulse in our experiment does not cover the entire C–H stretching region and has a lower energy limit just below d^- resonance. Unsurprisingly, the reduction in signal strength of the most prominent vibrational modes in the sum-frequency spectra (r^+ and r^-) is proportional to the IR absorption strength of the respective modes (see Section 3.1). However, pumping the CH_3 bend overtone (r^+_{fr}) does not result in a signal decrease of these prominent modes, although the overtone is prominent in the IR spectrum. This suggests that the vibrational energy relaxation from the bend overtone to the skeletal modes happens much faster than the energy transfer to the CH_3 stretching modes.

According to this reasoning, all energy put into the CH_3 bend overtone rapidly transfers to the skeletal modes of the alkyl chain.

Fitting the Arachidate Spectra

To analyze the vibrational dynamics of a molecular system, we need a thorough understanding of the spectral features. In this regard, there are still shortcomings, and we need more research to fully understand the arachidate spectrum. However, we were able to show how including the pumped spectra in the fitting process greatly improves the validity of the underlying line shape model. In particular, we could identify a hot band of the asymmetric CH_3 stretch, which was in no way apparent from the spectral features.

We were able to extract the transients of eight distinct vibrational modes from the data. However, because of the uncertainties in the underlying line shape model alluded to above, the only transients analyzed were those of the symmetric CH_3 stretch.

Reservoir Model

The reservoir model presented in this thesis fits the data very well. It is, moreover, not limited to this particular system, and theoretically, we can apply it to a variety of molecules and systems. Furthermore, it is easily extendable to incorporate other vibrational modes like, for example, N–H stretching vibrations. Through the model, we gained insights into the vibrational dynamics in the C–H stretch region of our system in unprecedented detail. Figure 4.1 shows an overview of the dynamics we could reveal.

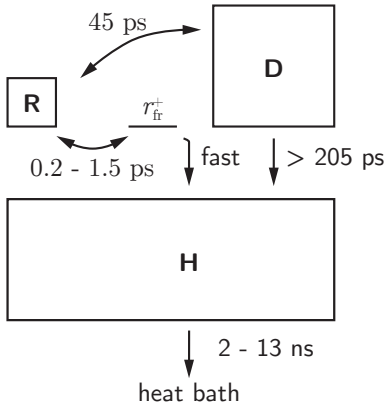

Figure 4.1: Schematic of the reservoir model with time constants for the vibrational energy redistribution.

Population Relaxation Times We can indirectly calculate population relaxation times for the CH_3 and CH_2 stretching vibrations from the reservoir model (see Chapter 3.4).

The population relaxation time of the CH_3, and CH_2 stretches are $T_{1,R} = 0.3\,\text{ps}$ and $T_{1,D} = 12\,\text{ps}$, respectively.

Vibrational Relaxation Pathways The reservoir model shows that the vibrational energy transfer from the C–H stretching modes to the skeletal modes happens almost exclusively through the overtone of the asymmetric CH_3 bending mode. The energy transfer from the CH_2 stretching modes to the skeletal modes is negligibly small.

Deàk et al. [16] proposed two possible pathways for the vibrational decay from the symmetric CH_3 stretch via the Fermi resonance (see Section 1.3). According to their work, the first possibility is that the IR pulse populates a pure CH_3 stretching vibration. From there, the vibrational energy relaxes through the overtone of the asymmetric CH_3 bending mode to the skeletal modes. A second possibility was that a combination state of the stretch and bend overtone gets excited from where the energy relaxes to the skeletal modes. In this work, we could show that there is no combination state since the r^+ mode shows a transient and the r_{fr}^+ does not. We could evaluate the time constant between the CH_3 symmetric stretch and the overtone of the asymmetric CH_3 bending mode to 0.7 ps. Since the r_{fr}^+ does not show a transient, we can conclude that the energy transfer from the overtone of the CH_3 bend to the skeletal modes is too fast to be resolved by our experiment.

Smits et al. [22] and Bredenbeck et al. [23, 24] revealed a strong coupling between the asymmetric CH_2 and symmetric CH_3 stretching modes. However, the time associated with the vibrational energy transfer was still an open question. In this work, we revealed that the time constant for the vibrational energy exchange between the CH_2 and CH_3 stretching modes is 45 ps. Note that this is the time constant for the energy exchange between the CH_3 and CH_2 stretching modes in general and not between the asymmetric CH_2 and symmetric CH_3 stretching modes specifically. However, we can argue that the time constant represents the fastest pathway for energy redistribution, which may coincide with the strongest coupling.

If, for any experiment, we wanted to have an excited CH_3 stretch, counterintuitively, it would be a better idea to induce the energy into the CH_2 stretching modes rather than into the CH_3 stretches directly. Firstly, the energy would then be located in the CH_3 stretch for a longer time span. Secondly, more energy would then flow through the CH_3 stretch since the total amount of energy induced into the system is larger.

Harris et al. [17] discussed that pumping the r^+ mode results in a slow recovery of this mode. Pumping the r^- mode, however, does not show a slow component. We revealed here that the slow component could arise from pumping the CH_2 stretching modes. Therefore, the difference in the observed transients in Ref. [17] is not due to different dynamics but may be caused by the experiment. In the r^+-pumped case, the laser could have simultaneously pumped a CH_2 stretching mode that happened to be in the spectral width

of the pump pulse, whereas in the r^--pumped case, it did not. The d^+ mode is located $\sim$20 cm^{-1} below the r^+ mode whereas the CH_2 stretching mode closest to r^- is the d^- mode located $\sim$40 cm^{-1} below (see Figure 2.18).

The Role of Gauche Defects We can disregard the role of gauche defects in our model to describe the transients of the CH_3 symmetric stretch. However, we cannot rule out the possibility that they play a role after all. It is possible gauche defects affect the intensity of the CH_3 stretching modes only to a minor degree while more significantly affecting the intensity of particular CH_2 stretches. The transients of the d^+ mode show a steady signal increase in both the d^- and r^--pumped cases (see Figure 3.6). The transients of the attenuation coefficients of the d_ω^- mode at 2887 cm^{-1} in Figure 3.9, however, do not imply an increase in signal strength of this particular mode. Therefore, it is possible gauche defects play a role in transients of particular CH_2 stretching modes, but it remains unclear to which extent.

Shortcomings

One of the biggest challenges was the fitting of the spectra. This is the determining step for the quality of the transients of the vibrational modes that we get from the data. Finding a reasonable line shape model is a non-trivial task. In this work, we revealed unexpected features in the spectrum, like the hot band of the r^- mode, only after fitting the spectra. In principle, we could redo the entire data analysis part with this information in mind and maybe gain even more detailed information. In hindsight, it would have been better to start out with a simpler molecule. For example, one that does not show as many spectral features.

In the experiments conducted in the context of this thesis, the IR pump had a lower energy limit of 2910 cm^{-1}. A continuous scan to lower energies is not possible. It would be advantageous to extend the pump range to lower wavenumbers to gain an even more detailed understanding of the vibrational dynamics in the C−H stretching region. Then, a pumping of the CH_2 and CH_3 symmetric stretches would be possible.

Summary

The kind of time-resolved 2-color IR/SF spectroscopy presented in this thesis allowed us to uncover vibrational dynamics that otherwise would have remained obscured. We were able to address and answer questions left open from previous works in the field of vibrational dynamics.

4.2 Outlook

There are still many questions to answer. This section will give an overview of possible starting points for further research.

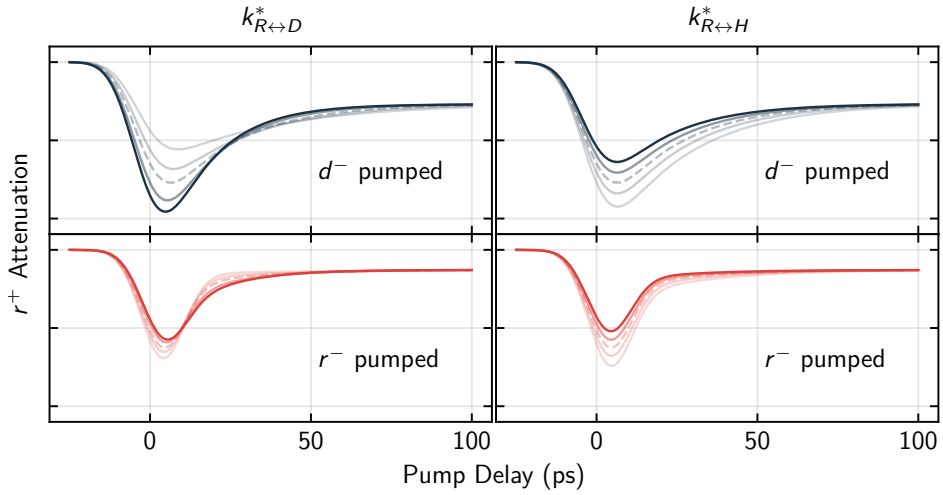

Figure 4.2: Simulated attenuations of the CH_3 symmetric stretch in dependence of the rate constants of vibrational relaxation; left: between the CH_3 and CH_2 stretching vibrations $k^*_{R\leftrightarrow D}$; right: between the CH_3 stretching vibration and the skeletal modes $k^*_{R\leftrightarrow H}$. The latter represents the energy exchange rate between the CH_3 stretching modes and the overtone of the asymmetric CH_3 bending modes (r^+_{fr}). The black and red curves represent the attenuation in the d^- and r^--pumped cases, respectively. As a reference, the dashed line represents the actual data set that was discussed in the previous Chapter. The more opaque the lines, the faster the vibrational energy exchange. The transients on the left were calculated with time constants ranging from 23 ps to 90 ps. The transients on the right were calculated with time constants between 0.56 ps and 1.00 ps.

The first step to take is to alter various parameters of the system and experiment. Firstly, to further validate the model presented in this thesis and secondly, to gain an intuitive feel for how to modify the system to evoke a certain change in its behavior. One idea would be the alter the length of the alkyl chain or increase the strength of the pump laser. However, simulations show that these do not cause a significant change in the transient of the r^+ mode. Another idea is to change the coupling between the CH_3 and CH_2 stretching modes. This could, for example, be done by inserting CD_2 groups between the CH_3 head group and the alkyl chain. Altering the coupling strength may lead to a change in the time constant of the vibrational energy redistribution between the symmetric CH_2 and CH_3 stretching vibrations. Figure 4.2 shows how a systematic alteration of the time constants affects the transients of the r^+ mode. From there, it is apparent that changing the time constant between the CH_2 and CH_3 stretches significantly affects the shape of the r^+ mode's transient. Altering the time constant between the r^+

mode and its Fermi resonance, however, only changes the intensity of the attenuation but not the temporal profile.

Having a molecule with a CD_3 instead of a CH_3 head group should eliminate the fast relaxation pathway from the r^+ mode through its Fermi resonance to the skeletal modes. This should significantly increase the overall vibrational relaxation time of the system. A problem to overcome is that the CH_2 modes are invisible in the SF spectrum. However, one could purposely create gauche defects by heating the sample to make them visible.

By providing a better line shape model for the SF spectrum of calcium arachidate we could drastically improve the transients for the asymmetric CH_3 stretch and or the CH_2 modes. This way, we may gain insights into the vibrational energy redistribution between the individual CH_3 and or CH_2 stretching vibrations.

To investigate the role of intermolecular energy transfer, we can alter the surface density of calcium arachidate molecules. The surface density can be adjusted in the preparation step with the Langmuir-Blodgett technique [52]. Another option to analyze the intermolecular energy transfer would be to dilute the monolayer with other molecules like, for example, fully deuterated arachidate.

To gain insights into the dynamics of the vibrational energy redistribution process of the low-energy deformation modes, we could probe this spectral region. The asymmetric CH_3 bending modes are located at a wavenumber of around $1500\,\mathrm{cm}^{-1}$. With the current setup, this is not possible since the probe IR will - to a large degree - be absorbed by the atmosphere. Therefore, the beam path would have to be flushed with, for example, dry air to avoid absorption by atmospheric water. To answer the question if gauche defects play a role in the transients of the r^+ mode, we could pump the r^+_{fr}. The vibrational energy would then immediately relax into the skeletal modes, potentially causing gauche defects. Without the prominent features that arise from the population of the CH_3 stretching vibrations, gauche defects might become visible.

Figure 2.6 shows that the beam geometry in the experiment is not ideal. Increasing the angle of the upconversion pulse would have three positive effects: Firstly, the intensity of the symmetric CH_3 stretch (and its Fermi resonance) would increase in the *ssp* polarized spectra. Higher intensity is generally desirable. Secondly, the intensity of the asymmetric CH_3 stretch would increase, which is again desirable. Thirdly, the intensity of the symmetric CH_3 stretch and its Fermi Resonance would decrease in the *ppp* polarized spectra. The positive effect of the latter is that this reduces the complexity of the spectrum while not losing information. This is because the symmetric CH_3 stretch can be better resolved in *ssp* polarization anyway.

As we can see, there are still many questions to answer. Hopefully, this thesis marks the beginning of a series of experiments that will continue unraveling the remaining mysteries of vibrational dynamics in condensed matter.

Appendix

1 Event Removal

The following algorithm was used to remove cosmic events from the acquired images. The algorithm is described in Section 2.2.2.

```
# Julia v1.6

using Statistics

function rm_events!(s::Array{T}; width=3, minstd=5) where T <: Real

    # Behaves like `diff` but is twice as fast
    function mydiff(a)
        b = Array{T,1}(undef, length(a)-1)
        for i = 1:length(a)-1
            b[i] = a[i+1] - a[i]
        end
        b
    end

    r = reshape(s, :)
    dr = mydiff(r)
    num_removed_events = 0

    threshold = minstd * std(dr)
    startidx = width + 1
    endidx = length(dr)
    lowidx = 0

    for i = startidx:endidx
        lowidx = i - width

        if any(dr[j] > threshold for j in lowidx:i) && dr[i] < -threshold
            tmp = dr[lowidx:i]
            width_real = width - argmax(tmp) + 1
            r[i-width_real+1:i] .= (r[i-width_real] + r[i+1])/2
            num_removed_events += 1
        end
    end

    s .= reshape(r, size(s))

    num_removed_events
end
```

2 Reservoir Model

The following code contains the function definitions for the reservoir model discussed in Section 3.4.

```
# Julia v1.6

using DifferentialEquations # v6.16.0

abstract type PumpedMode end
struct RPump <: PumpedMode end
struct DPump <: PumpedMode end

"""
Unnormalized Gaussian distribution to model the pump pulse.
"""
function gauss(t, t0, σ)
    exp(-(t - t0)^2 / σ^2)
end

"""
Dispatch to the model function.
"""
function model(du, u, p, t, M::T) where T <: PumpedMode
    k_rd, k_dr, k_rh, k_hr, k_dh, k_hd, x_r, x_d, t0_R, t0_D, σ = p

    if M isa RPump
        t0 = t0_R
        x_d = 0.0
    elseif M isa DPump
        t0 = t0_D
        x_r = 0.0
    end

    p_new = [k_rd, k_dr, k_rh, k_hr, k_dh, k_hd, x_r, x_d, t0, σ]

    model(du, u, p_new, t)
end

"""
Main model
"""
function model(du, u, p, t)
    ur, ud, uh =  u

    k_rd, k_dr, k_rh, k_hr, k_dh, k_hd, x_r, x_d, t0, σ = p

    pump = gauss(t, t0, σ)

    #            D <--> R                R <--> H                   <--> R
    du[1] =      k_rd * (ud - ur) -      k_rh * (ur - uh) + pump * x_r * (1 - 2ur)
    #            R <--> D                D <--> H                   <--> D
    du[2] =      k_dr * (ur - ud) - 10 ^ k_dh * (ud - uh) + pump * x_d * (1 - 2ud)
    #            D <--> H                R <--> H
    du[3] = 10 ^ k_hd * (ud - uh) +      k_hr * (ur - uh)
```

```
    nothing
end

"""
Dispatch to the model with the R reservoir pumped.
"""
model_r(du, u, p, t) = model(du, u, p, t, RPump())

"""
Dispatch to the model with the D reservoir pumped.
"""
model_d(du, u, p, t) = model(du, u, p, t, DPump())

"""
Calculate the attenuation of an r-mode from the solution. This expects the a_r
array to be initialized with 1.0 for each element.
    a_r *= 1 - 2u_r
"""
function rmode_attn_from_population!(a, sol)
    # the 1st column of the solution is the R state
    @. a *= 1 - 2sol[1,:]
    nothing
end

"""
Calculate the attenuation of the R mode based on the population in the H state.
    a_r *= 1 - u_h · f_h
"""
function rmode_attn_from_hstate!(a, sol, f_H)
    # the 3rd column of the solution is the H state
    @. a *= 1 - sol[3,:] * f_H
    nothing
end

"""
Not implemented.
"""
function hotband_attenuation!(a, sol)
error("Not implemented yet")
end

function least_squares!(fit, data)
    fit .-= data
    fit .^= 2
    sum(fit)
end

"""
* `a`:  Tuple; The first element is the attenuation data of the r(+) mode (this has
to be an array; r/d pumped. Has to have the same order as xvals and data). The second
element is the attenuation data of the μ mode (Tuple; same as r(+) mode
attenuation)
* `p`: The parameters that are going to be fitted
* `xvals`: Pump delay data (tuple)
* `data`: data (tuple)
* `ode_problems`: ODEProblems (tuple)
"""
function cost_function!(a::Tuple, p, xvals::Tuple, data::Tuple, ode_problems, f_H=1.0;
    μmode=false, fix_rd_ratio=false, ratio_limit=false, ratio=20.0, fix_f_H=true)
```

```
        # Decompose Parameters
        # This is the factor that scales the signal reduction of the r-modes with
        # the population in the H state.

        # get f_h value from parameters if it's not fixed
        fix_f_H || (f_H = p[end])

        fix_rd_ratio && (p[1] = ratio * p[2])
        ratio_limit && (p[1] / p[2] > ratio) && return Inf

        # Remake the ODE Problems with the new parameters
        tmp_ode_problems = [remake(_prob, p=p) for _prob in ode_problems]

        # Solve the ODE Problems
        sols = [solve(_prob, Tsit5(); saveat=_x) for (_prob, _x) in zip(tmp_ode_problems, xvals)]

        # Make sure the problems actually got solved
        if any([_s.retcode != :Success for _s in sols])
            return Inf
        end

        # initialize the attenaution parameters to 1.0
        for _am in a, _a in _am
            _a .= 1.0
        end

        if issorted(sols[1].t) ⊻ issorted(xvals[1])
            error("one sorted one not")
        end

        rmode_attn_from_population!.(a[1], sols)
        rmode_attn_from_hstate!.(a[1], sols, f_H)
        μmode && hotband_attenuation!.(a[2], sols)

        # least squares and cost
        cost = 0.0

        for (_am, _dm) in zip(a, data)
            for (_a, _d) in zip(_am, _dm)
                least_squares!(_a, _d)
                cost += sum(_a)
            end
        end

        cost
    end
```

3 Confidence Interval Estimation

Figure 1 shows the distribution of estimates for the parameters of the reservoir model in Section 3.4.4.

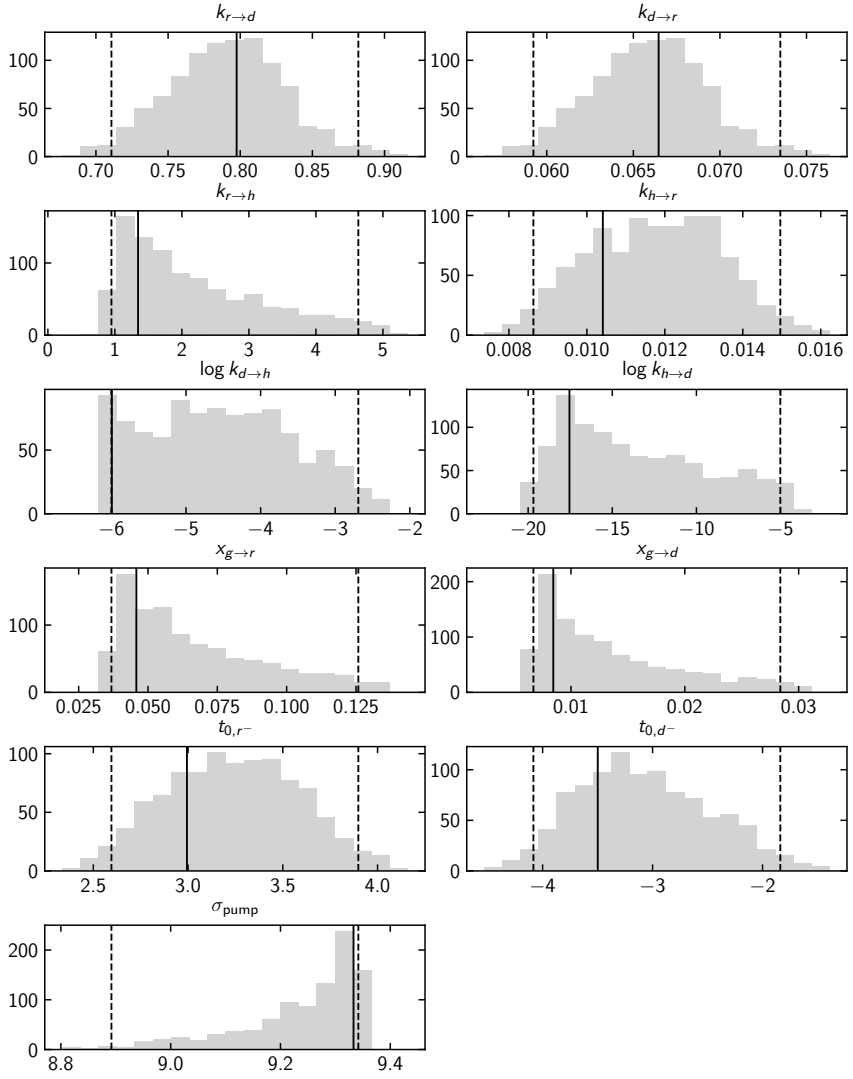

Figure 1: Distribution of estimates for the parameters of the reservoir model obtained with the bootstrap method. The estimate for the original data is indicated with the solid vertical line and the dashed lines indicate the 95 % confidence interval.

Bibliography

(1) Lackner, M.; Hille, M.; Hasselbrink, E. *The Journal of Physical Chemistry Letters* **2019**, 108–112.

(2) Lambert, A. G.; Davies, P. B.; Neivandt, D. J. *Applied Spectroscopy Reviews* **2005**, *40*, 103–145.

(3) Harris, D. C.; Bertolucci, M. D., *Symmetry and Spectroscopy*; Dover Publications: New York, 1989.

(4) Ong, S.; Zhao, X.; Eisenthal, K. B. *Chemical Physics Letters* **1992**, *191*, 327–335.

(5) Giordmaine, J. A. *Physical Review* **1965**, *138*, A1599–A1606.

(6) DiVincenzo, D. P. *Physical Review B* **1988**, *37*, 1245–1261.

(7) Fischer, P.; Wiersma, D. S.; Righini, R.; Champagne, B.; Buckingham, A. D. *Physical Review Letters* **2000**, *85*, 4253–4256.

(8) Belkin, M. A.; Shen, Y. R. *International Reviews in Physical Chemistry* **2005**, *24*, 257–299.

(9) Shen, Y. R., *Fundamentals of Sum-Frequency Spectroscopy*; Cambridge University Press: Cambridge, 2016.

(10) Boyd, R. W., *Nonlinear Optics*, Third Edition; Academic Press: Burlington, 2008.

(11) Hill, J. R.; Dlott, D. D. *Journal of Chemical Physics* **1988**, *89*, 830–841.

(12) Hill, J. R.; Dlott, D. D. *Journal of Chemical Physics* **1988**, *89*, 842–858.

(13) Hill, J. R.; Chronister, E. L.; Chang, T.; Kim, H.; Postlewaite, J. C.; Dlott, D. D. *The Journal of Chemical Physics* **1988**, *88*, 949–967.

(14) Velsko, S.; Hochstrasser, R. M. *The Journal of Physical Chemistry* **1985**, *89*, 2240–2253.

(15) Laubereau, A.; Kaiser, W. *Reviews of Modern Physics* **1978**, *50*, 607–665.

(16) Deàk, J. C.; Iwaki, L. K.; Rhea, S. T.; Dlott, D. D. *Journal of Raman Spectroscopy* **2000**, *31*, 263–274.

(17) Harris, A. L.; Levinos, N. J. *Journal of Chemical Physics* **1989**, *90*, 3878.

(18) Harris, A. L.; Levinos, N. J. *SPIE Proceedings* **1989**, *1056*.

(19) Harris, A. L.; Rothberg, L.; Dhar, L.; Levinos, N. J.; Dubois, L. H. *Journal of Chemical Physics* **1991**, *94*, DOI: 10.1063/1.459867.

(20) Löbau, J.; Wolfrum, K. *Journal of the Optical Society of America B* **1997**, *14*, 2505.

(21) Saß, M.; Löbau, J.; Lettenberger, M.; Laubereau, A. *Chemical Physics Letters* **1999**, *311*, 13–20.

(22) Smits, M.; Ghosh, A.; Bredenbeck, J.; Yamamoto, S.; Müller, M.; Bonn, M. *New Journal of Physics* **2007**, *9*, 390.

(23) Bredenbeck, J.; Ghosh, A.; Nienhuys, H.-K.; Bonn, M. *Accounts of Chemical Research* **2009**, *42*, 1332–1342.

(24) Bredenbeck, J.; Ghosh, A.; Smits, M.; Bonn, M. *Journal of the American Chemical Society* **2008**, *130*, 2152–3.

(25) Laubereau, A.; Kirschner, L.; Kaiser, W. *Optics Communications* **1973**, *9*, 182–185.

(26) Alfano, R. R.; Shapiro, S. L. *Physical Review Letters* **1972**, *29*, 1655–1658.

(27) Laubereau, A.; Kehl, G.; Kaiser, W. *Optics Communications* **1974**, *11*, 74–77.

(28) Laubereau, A.; Linde, D. v. d.; Kaiser, W. *Physical Review Letters* **1972**, *28*, 1162–1165.

(29) Fendt, A.; Fischer, S.; Kaiser, W. *Chemical Physics* **1981**, *57*, 55–64.

(30) Zygan-Maus, R.; Fischer, S. F. *Chemical Physics* **1979**, *41*, 319–327.

(31) Wolfrum, K.; Löbau, J.; Birkhölzer, W.; Laubereau, A. *Quantum and Semiclassical Optics: Journal of the European Optical Society Part B* **1999**, *9*, 257.

(32) Wang, J.; Chen, C.; Buck, S. M.; Chen, Z. *The Journal of Physical Chemistry B* **2001**, *105*, 12118–12125.

(33) Wang, H.-F.; Gan, W.; Lu, R.; Rao, Y.; Wu, B.-H. *International Reviews in Physical Chemistry* **2005**, *24*, 191–256.

(34) Zhuang, X.; Miranda, P. B.; Kim, D.; Shen, Y. R. *Physical Review B* **1999**, *59*, 12632–12640.

(35) Janesick, J. R.; Elliott, T.; Collins, S.; Blouke, M. M.; Freeman, J. *Optical Engineering* **1987**, *26*, 268692–268692-.

(36) Drury, L. O. *Astroparticle Physics* **2012**, *39*, 52–60.

(37) Florentin-Nielsen, R.; Andersen, M. I.; Nielsen, S. P. **1995**, 207–211.

(38) Rabolt, J. F.; Burns, F. C.; Schlotter, N. E.; Swalen, J. D. *The Journal of Chemical Physics* **1983**, *78*, 946–952.

(39) Naselli, C.; Rabolt, J. F.; Swalen, J. D. *The Journal of Chemical Physics* **1985**, *82*, 2136–2140.

(40) Outka, D. A.; Stöhr, J.; Rabe, J.; Swalen, J. D.; Rotermund, H. H. *Physical Review Letters* **1987**, *59*, 1321–1324.

(41) Rabe, J. P.; Swalen, J. D.; Rabolt, J. F. *The Journal of Chemical Physics* **1987**, *86*, 1601–1607.

(42) Cardini, G.; Bareman, J. P.; Klein, M. L. *Chemical Physics Letters* **1988**, *145*, 493–498.

(43) Rabe, J. P.; Novotny, V.; Swalen, J. D.; Rabolt, J. F. *Thin Solid Films* **1988**, *159*, 359–367.

(44) Shih, M. C.; Bohanon, T. M.; Mikrut, J. M.; Zschack, P.; Dutta, P. *The Journal of Chemical Physics* **1992**, *96*, 1556–1559.

(45) Tippmann-Krayer, P.; Kenn, R. M.; Möhwald, H. *Thin Solid Films* **1992**, *210-211*, 577–582.

(46) Akamatsu, N.; Domen, K.; Hirose, C. *The Journal of Physical Chemistry* **1993**, *97*, 10070–10075.

(47) Shih, M.; Peng, J.; Huang, K.; Dutta, P. *Langmuir* **1993**, *9*, 776–778.

(48) Kinzler, M.; Schertel, A.; Hähner, G.; Wöll, C.; Grunze, M.; Albrecht, H.; Holzhüter, G.; Gerber, T. *The Journal of Chemical Physics* **1994**, *100*, 7722–7735.

(49) Schertel, A.; Hähner, G.; Grunze, M.; Wöll, C. *Journal of Vacuum Science & Technology A: Vacuum , Surfaces , and Films* **1996**, *14*, 1801–1806.

(50) Takamoto, D. Y.; Aydil, E.; Zasadzinski, J. A.; Ivanova, A. T.; Schwartz, D. K.; Yang, T.; Cremer, P. S. *Science* **2001**, *293*, 1292–1295.

(51) Ye, S.; Noda, H.; Nishida, T.; Morita, S.; Osawa, M. *Langmuir* **2004**, *20*, 357–365.

(52) Weber, J.; Beier, A.; Hasselbrink, E.; Balgar, T. *The Journal of Chemical Physics* **2014**, *141*, 044912.

(53) Beier-Hannweg, A.; Firla, D.; Hasselbrink, E. *Thin Solid Films* **2017**, *642*, 1–7.

(54) Roberts, G., *Langmuir-Blodgett Films*; Springer: Boston , MA, 1990.

(55) Weber, J. Temperature induced change in aliphatic monolayers observed by vibrational sum-frequency generation spectroscopy., Ph.D. Thesis, Universität Duisburg-Essen, 2014.

(56) Weber, J.; Balgar, T.; Hasselbrink, E. *The Journal of Chemical Physics* **2013**, *139*, 244902.

(57) Beier-Hannweg, A. Geordnete Molekülschichten und der Einfluss thermischer Anregung auf ihre Schwingungsspektren., Ph.D. Thesis, Universität Duisburg-Essen, 2018.

(58) Bibo, A. M.; Peterson, I. R. *Advanced Materials* **1990**, *2*, 309–311.

(59) Chow, B.; Ehler, T.; Furtak, T. *Applied Physics B* **2002**, *74*, 395–399.

(60) Ji, N.; Ostroverkhov, V.; Chen, C.-Y.; Shen, Y.-R. *Journal of the American Chemical Society* **2007**, *129*, 10056–10057.

(61) Himmelhaus, M.; Eisert, F.; Buck, M.; Grunze, M. *The Journal of Physical Chemistry B* **2000**, *104*, 576–584.

(62) Hill, I. R.; Levin, I. W. *The Journal of Chemical Physics* **1979**, *70*, 842.

(63) McKean, D. *Spectrochimica Acta Part A: Molecular Spectroscopy* **1973**, *29*, 1559–1574.

(64) Chernick, M. R., *Bootstrap Methods: A Guide for Practitioners and Researchers*; Wiley: 2007.

(65) Carpenter, J.; Bithell, J. *Statistics in Medicine* **2000**, *19*, 1141–1164.

(66) Wilson, E.; Decius, J.; Cross, P., *Molecular Vibrations: The Theory of Infrared and Raman Vibrational Spectra*; Dover Books on Chemistry Series; Dover Publications: 1980.

(67) Kjaergaard, H. G.; Yu, H.; Schattka, B. J.; Henry, B. R.; Tarr, A. W. *The Journal of Chemical Physics* **1990**, *93*, 6239–6248.

(68) Buck, M.; Himmelhaus, M. *Journal of Vacuum Science & Technology A: Vacuum , Surfaces , and Films* **2001**, *19*, 2717.

(69) Linke, M.; Hille, M.; Lackner, M.; Schumacher, L.; Schlücker, S.; Hasselbrink, E. *The Journal of Physical Chemistry C* **2019**, *123*, 24234–24242.